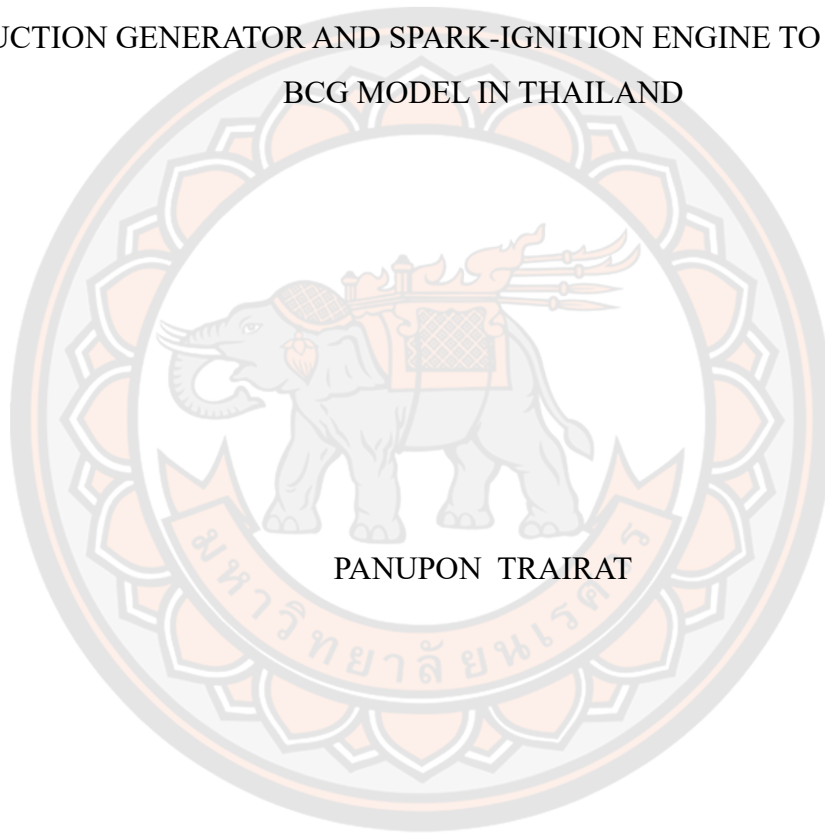GRID INTEGRATION OF LIVESTOCK BIOGAS USING SELF-EXCITED
INDUCTION GENERATOR AND SPARK-IGNITION ENGINE TO SUPPORT THE
BCG MODEL IN THAILAND

PANUPON TRAIRAT

A Thesis Submitted to the Graduate School of Naresuan University
in Partial Fulfillment of the Requirements
for the Doctor of Philosophy in Smart Grid Technology
2023

GRID INTEGRATION OF LIVESTOCK BIOGAS USING SELF-EXCITED
INDUCTION GENERATOR AND SPARK-IGNITION ENGINE TO SUPPORT THE
BCG MODEL IN THAILAND

PANUPON TRAIRAT

A Thesis Submitted to the Graduate School of Naresuan University
in Partial Fulfillment of the Requirements
for the Doctor of Philosophy in Smart Grid Technology
2023

Thesis entitled "Grid Integration of Livestock Biogas Using Self-Excited Induction Generator and Spark-Ignition Engine to support the BCG model in Thailand"

By Panupon Trairat

has been approved by the Graduate School as partial fulfillment of the requirements

for the Doctor of Philosophy in Smart Grid Technology of Naresuan University

Oral Defense Committee

.... Chair
(Associate Professor Pisit Liutanakul, Ph.D.)

.... Advisor
(Associate Professor Sakda Somkun, Ph.D.)

.... Internal Examiner
(Assistant Professor Sahataya Thongsan, Ph.D.)

.... Internal Examiner
(Associate Professor Pisit Maneechot, Ph.D.)

.... Internal Examiner
(Phatcharin Yaowarat, Ph.D.)

Approved

....
(Associate Professor Krongkarn Chootip, Ph.D.)
Dean of the Graduate School

Title	GRID INTEGRATION OF LIVESTOCK BIOGAS USING SELF-EXCITED INDUCTION GENERATOR AND SPARK-IGNITION ENGINE TO SUPPORT THE BCG MODEL IN THAILAND
Author	Panupon Trairat
Advisor	Associate Professor Sakda Somkun, Ph.D.
Academic Paper	Ph.D. Dissertation in Smart Grid Technology, Naresuan University, 2023
Keywords	SEIG, Back-to-back converter, biogas, spark-ignition engine, BCG model, Circular economy

ABSTRACT

This study aims to develop small grid-connected power generation units for farming systems to support Thailand's Bio-Circular-Green Economic Model (BCG). The focus is on utilizing agricultural waste resources within the circular economy framework of the BCG model. Biogas is used as the primary fuel for the internal combustion engine (IC engine), with gasoline and LPG as backup fuels for emergencies. The system includes an engine that drives a self-excited induction generator (SEIG). A grid-connected inverter control strategy based on PQ control has been designed for power conversion, using digital signal processing (DSP). Additionally, interface-based Internet of Things (IoT) devices enable wireless connectivity for monitoring and controlling the system via a dashboard application. The proposed system is validated with biogas produced from pig manure at a farm in central Thailand, achieving a maximum output of 1.2 kW with a thermal system efficiency of 10.7%. Scheduled operation at 1.2 kW for 8 hours daily yields a levelized cost of 0.07 US$/kWh, representing a 42% cost reduction compared to retail electricity prices, with a payback period of 2.76 years. The system is deemed suitable for farms with a minimum of 34 pigs, offering a sustainable and economically viable energy solution for rural communities.

ACKNOWLEDGEMENTS

Panupon Trairat

TABLE OF CONTENTS

LIST OF TABLES

LIST OF FIGURES

Page

CHAPTER I

INTRODUCTION

1.1 Background and Significance of the Study

In Thailand, which is regarded as a genuine agricultural society, the majority of people work in agriculture, raising small livestock like pigs, poultry, fish, and cows as well as annual crops like rice, sugar cane, corn, and cassava. However, the farming production process remains unchanged and operates at a low level. The Thai government encourages innovation to raise the standard and volume of agricultural output because there are not many innovations drives specifically focused on agriculture. As a plan to establish equality and sustainability for the economy, society, and environment, the Thai government has introduced the BCG model [1, 2]. The concept focuses on using innovation, science, and technology to turn cultural and biodiversity comparative advantages into competitive ones. Four key industries are where its benefits are primarily concentrated: 1) Food and Agriculture; 2) Medical and Health; 3) Materials, Energy, and Biochemistry; and 4) Travel and Creative Economy. Three leading economies make up the BCG model: System of Bio-Economy (B) Emphasize the economical utilization of biological resources, integrating it with the Circular Economy (C), which takes into account reusing different materials as much as possible. Both of these economies fall under the Green Economy (G) framework, which seeks to address pollution issues in order to lessen the planet's impact in a sustainable manner [3-6], as illustrated in figure 2. In contrast, In the near future, Thailand's agriculture will become more sustainable thanks to the BCG model's smart practices for agriculture 4.0 [3-6].

The 2021–2027 BCG Action Plan [1] outlines two primary concerns for development in the agriculture and energy sectors: the promotion of renewable energy. Based on the BCG model, biogas is an alternative energy that is used in the circular economy to recycle waste from industry and agriculture [1, 7]. According to our analysis of Thailand's livestock and agricultural industries, biogas fuel generation

from animal dung or agricultural waste has the potential to be used for cooking fuel combustion [8–10]. Although it is not widely used, biogas is an appealing fuel for electricity production. If it is able to produce electricity for farming, it will boost independence by controlling the amount of electricity used for both domestic and agricultural purposes. There are three main ways that biogas-fueled power generation might address the BCG model. To be clear, this can be categorized as follows: 1) Bioeconomy: use biodiversity and biotechnology as catalysts. 2) The circular economy, which produces alternative energy by using waste materials. 3) Green economy: sustainable and ecologically friendly growth.

Producing biogas is an environmentally friendly way to manage waste for the residential, commercial, and agricultural sectors. It directly affects and helps to achieve 12 of the 17 Sustainable Development Goals (SDGs) [11]. Anaerobic microbial fermentation produces biogas from organic waste from agriculture, industry, and municipalities as well as sewage sludge [12, 13]. The production of biogas from livestock farms in underdeveloped nations has the potential to reduce greenhouse gas emissions and promote environmentally responsible waste management [14]. Transportation, electricity generation, and heat production are the typical uses for biogas fuel [11].

Solid oxide fuel cells (SOFCs) can be used to electrochemically convert biogas directly into energy while emitting almost little greenhouse gas. However, in order to make SOFCs appropriate for industrial sizes, complex biogas cleaning and compression systems are needed [15]. Moreover, underdeveloped nations find it difficult to adapt due to the high cost of investments [16]. However, the use of biogas-fed micro gas turbines to generate electricity from sewage treatment systems shows promise [17, 18]. Biogas-fueled micro gas turbines rotate at speeds between 43,000 and 240,000 revolutions per minute (rpm) and have efficiencies ranging from 20 to 30% [18]. A generator that produces electricity at 50/60 Hz is paired with a mechanical transmission system to form a well-equipped micro gas turbine. Comparing the GHG emissions to traditional internal combustion engines, the emissions are far lower. From 30 kW to more than 200 kW, commercial micro gas turbines are available [18]. Technologies for internal combustion engines are

completely developed. With an electrical efficiency of up to 40%, commercial biogas engines for power generation range in size from 25 kW [19] to 2 MW [20]. There has been much research done on the modification of conventional internal combustion engines running on biogas. Diesel and biogas can be used as simultaneous fuels for compression-ignition engines with some modifications [21]. It is also possible to convert a compression-ignition engine to a spark-ignition engine that runs exclusively on biogas or producer gas [22, 23]. To use biogas as the only fuel, standard spark-ignition engines need to be slightly modified [24–26].

The mechanical effort of the biogas-fed engines is typically converted to AC energy using electrically excited synchronous generators [21–23, 26]. For a stand-alone application, the output voltage is regulated by the generator excitation current, and the output frequency is regulated by the engine speed governor. Prior to synchronization, the generator voltage and frequency must be precisely matched to the grid for a grid connection. Compared to electrically excited synchronous generators (ESSGs), which were used in biogas-fed power generating systems [19, 24], permanent magnet synchronous generators (PMSGs) provide greater compactness [27]. Grid integration and output voltage and frequency regulation require the use of a power electronic converter [19, 20, 24]

Another option for producing electricity from biogas is the use of self-excited induction generators (SEIGs) [28–30]. Commercial 3-phase induction machines can be used as generators using SEIGs, which have a durable design and require very little maintenance [31]. Additionally, a SEIG is far less expensive than a PSMG [32]. For wind [33, 34] and small hydro [35–38] energy systems, SEIGs are frequently used. Reactive power is necessary for SEIG excitation and terminal voltage regulation, albeit [39]. The variable-speed prime movers, such as wind and hydro turbines, which are supplied from capacitor banks [30, 38, 40, 41], and hybrid excitation systems made up of static variable generators (SVGs) and capacitor banks [29, 33–37], are what drive the SEIGs in the variable-frequency stand-alone system. By adding a current balancing circuit and a dummy load, a 3-phase SEIG can be used as a standalone single-phase AC power source [42]. The SEIG can be run with variable-speed prime movers and a set speed for grid-connected operation. A

regulated speed prime mover with a restricted mechanical speed range of 1%–5% above the synchronous speed can be used with the SEIG's direct grid connection for fixed speed operation [28]. The SEIG connects to the grid in order to operate as a variable-speed grid-connected device.

A 45-kW SEIG-fed three-phase stand-alone system via a diode bridge rectifier and voltage source converter (VSC) is taken into consideration when discussing the biogas-powered SEIG-based generator systems [30]. A three-phase grid was immediately connected to a 100-kW commercial gas engine-SEIG system [28]. A three-phase standalone system with a VSC-based SVG for generator voltage regulation was directly supplied by a 7-kW gas engine-SEIG system [29]. A speed regulating mechanism was fitted to the gas engines of the three SEIG-based biogas power production systems.

Single-phase grid-connected biogas power generating systems for a small community with a maximum power of less than 5 kW are not reported for, as was previously noted. Thus, the creation of a grid-connected biogas power generation system for a small pig farm in central Thailand is reported in this work. The prime mover was a 196-cc single-cylinder spark-ignition engine powered by biogas produced by the anaerobic digestion of pig dung and wastewater. As a SEIG, a 3-phase, 2.2-kW squirrel-cage induction motor was used. Furthermore, we created a power electronic converter to integrate a 220-V, 50-Hz single-phase grid and control generator excitation. Technical and financial viability was confirmed through field and laboratory testing.

1.2 Purposes of the Study

      1. To develop a prototype of a 1.5 kW single-phase grid-connected inverter for self-excited induction generator from biogas, intended for use on small to medium-sized ranch farms.

      2. To test the grid-connected inverter according to the PEA/MEA grid-code standards.

      3. To develop interface-based Internet of Things (IoT) devices can be wirelessly connected for controlled and logged data via a dashboard application.

1.3 Scope of the Study

      1. To modify a three-phase squirrel-cage induction motor to operate as a generator.

      2. To develop a prototype of a 1.5 kW grid-connected inverter for a self-excited induction generator.

      3. To modify a gasoline internal combustion engine to utilize biogas fuel.

1.4 Benefits of the Study

      1. Prototype development of a 1.5 kW grid-connected inverter for power generation using a biogas engine, compliant with grid code transmission.

      2. Patenting opportunities for the 1.5 kW grid-connected inverter for power generation with a biogas engine.

      3. Our experience with grid-connected inverters and biogas improvement has been invaluable. Looking ahead, we expect biogas power generation to be widely used in smart grids, enhancing sustainability and efficiency.

1.5 Research Methodologies

8.1 Testing parameters of a squirrel-cage induction motor.

8.2 Creating and simulating a model of the inverter and controller in MATLAB/Simulink.

8.3 Designing and constructing the power electronics components of the inverter.

8.4 Designing the controller for the inverter.

8.5 Designing Interface-based Internet of Things (IoT) devices can be wirelessly connected, allowing for controlled and logged data via a dashboard application.

8.6 Testing the grid-connected inverter based on the PEA/MEA grid code standards.

8.7 Conducting laboratory tests on the power generation system using an induction generator as the prime mover.

8.8 Conducting laboratory tests on the power generation system using an internal combustion engine as the prime mover.

8.9 Testing the overall power generation system with a biogas combustion engine.

CHAPTER II

THEORY AND LITERATURE REVIEW

2.1 Biogas production

2.1.1 The basics of biogas production

Biogas production is an environmentally friendly and sustainable energy generation technology that uses anaerobic digestion to turn organic waste into biogas. Methane (CH_4) and carbon dioxide (CO_2) make up the majority of biogas, with trace amounts of other gases such as hydrogen sulfide (H_2S) and water vapor. It can be utilized as an energy source for a number of purposes, such as heating, producing electricity, and even as fuel for automobiles [8–10].

Here are the key steps involved in biogas production:

1) Feedstock Selection: Biogas is produced using organic resources, sometimes referred to as feedstock. Animal manure, agricultural residues, food waste, sewage sludge, and energy crops (such maize or grass) are common sources of feedstock.

2) Preparation: Gathered and ready for the anaerobic digestion process is the feedstock. To do this and expand the surface area available for microbial activity, mechanical techniques such as chopping, shredding, or other methods may be used.

3) Anaerobic Digestion: The primary method by which bacteria decompose organic materials when oxygen is not present is called anaerobic digestion. This procedure takes place in an oxygen-free, enclosed digester tank. Anaerobic digestion occurs in four stages:

- Hydrolysis: Hydrolysis is the process by which complex organic molecules are reduced to simpler forms.

- Acidogenesis: Volatile fatty acids are produced from the simpler molecules by bacteria that produce acid.

- **Acetogenesis:** From the volatile fatty acids, acetic acid is produced.

- **Methanogenesis:** Methane and carbon dioxide are produced by methanogenic bacteria from acetic acid and other intermediates.

4) Gas Collection: At the top of the digester tank is where the biogas generated during the anaerobic digestion process is gathered.

5) Gas Storage and Upgrading: Additional processing of biogas might be necessary to eliminate contaminants like moisture and hydrogen sulfide (H_2S). It can also be utilized immediately for different applications or kept in tanks. Biomethane, a refined form of biogas with a greater methane concentration that may be injected into natural gas pipelines or used as a fuel for transportation, can also occasionally be improved from biogas.

6) Biogas Utilization: Biogas has several uses, some of which are as follows:

- **Electricity Generation:** Gas engines and turbines can produce electricity by using biogas.

- **Heat Production:** It can be used for district heating, as well as for heating houses and businesses.

- **Vehicle Fuel:** It can be converted to biomethane and utilized as a clean-burning automotive fuel.

- **Cooking and Lighting:** In certain areas, homes use biogas for lighting and cooking.

The production of biogas has various advantages for the environment and the economy. It offers a sustainable energy source, aids in the management of organic waste, and lowers greenhouse gas emissions. It can also be included into waste management and sustainable agriculture methods, supporting the circular economy. However, elements including feedstock quality, digester design, and operational management are crucial to the success of biogas production.

2.1.2 The composition of biogas

The composition of biogas can vary depending on the feedstock used, the anaerobic digestion process conditions, and the specific microbial activity in the digester. However, the typical composition of biogas consists primarily of methane (CH_4) and carbon dioxide (CO_2), with trace amounts of other gases. Here is a general overview of the typical composition of biogas:

1. Methane (CH_4): Methane is the primary component of biogas and is responsible for its combustible nature. The methane content in biogas usually ranges from 50% to 75% or higher, depending on the efficiency of the anaerobic digestion process.

2. Carbon Dioxide (CO_2): Carbon dioxide is the second most abundant gas in biogas. It typically makes up 25% to 50% of the total biogas volume. While carbon dioxide is not combustible, its presence in biogas is essential for safety reasons, as it dilutes the combustible methane and reduces the risk of explosion.

3. Nitrogen (N_2): Nitrogen may be present in biogas in small amounts, typically less than 1%. It enters the system with the incoming air or feedstock and can remain in the gas mixture after the anaerobic digestion process.

4. Hydrogen Sulfide (H_2S): Hydrogen sulfide is a common impurity in biogas and is produced during the decomposition of sulfur-containing compounds in the feedstock. It is usually present in trace amounts but can be problematic due to its corrosive nature and foul odor. Efforts are often made to remove or reduce hydrogen sulfide through gas purification processes.

5. Trace Gases: Biogas may contain trace amounts of other gases, such as ammonia (NH_3), water vapor, oxygen (O_2), and various volatile organic compounds (VOCs). The presence of these gases depends on the composition of the feedstock and the efficiency of the anaerobic digestion process.

The composition of biogas is depicted in Table 1.

Table 1 *Typical composition of biogas [8]*

Compound	Formula	Percentage by volume
Methane	CH_4	50 – 80
Carbon dioxide	CO_2	15 – 50
Nitrogen	N_2	0 – 10
Hydrogen	H_2	0 – 1
Hydrogen sulfide	H_2S	0 – 1.5
Oxygen	O_2	0 – 2.5

It is important to note that the specific composition of biogas can be influenced by factors such as temperature, pH, retention time, and the microbial community in the digester. Biogas composition can also be tailored for specific applications by adjusting the digestion process and incorporating gas purification technologies to meet quality standards for different end uses, such as electricity generation or vehicle fuel.

2.1.3 The potential for biogas production in Thailand.

Saran K. et al.'s study [8] examined Thailand's potential for producing biogas. In 2019, data from surveys of three sectors—industrial plants, agricultural plants, and livestock—showed that Thailand has the capacity to produce 22,826.79 million cubic meters annually, of which 7,521.48 million m^3 come from industrial plants, 14,479.01 million m^3 come from agricultural plants, and 826.30 million m^3 come from livestock. Table 2 also provides further information.

Table 2 *The potential of biogas production in Thailand 2019 [8]*

Biogas Source	Production potential (million m^3/years)	Productivity (million m^3/years)	Remaining (million m^3/years)
Industrial plants	7,521.48	747.45	6774.03
Livestock	826.30	68.61	757.66
Agricultural	1,4479.01	-	14,479.01
Total	22,826.79	816.06	22010.70

This study focused exclusively on the livestock and agriculture industries. For these two sectors, we thus display the rates of waste-to-biogas generation. as indicated by Tables 3 and 4 [8], [10], which list the many kinds of animal farms and agricultural plants that may be found in Thailand.

Table 3 Livestock biogas production rate [8]

Types	Manure rate per day (kg/animal)	Manure collected (%)	Evaporation Rate of Solids (%)	Biogas Production Rate (m3/kg(solids))
1. Beef cattle	5.00	50	13.37	0.307
2. Dairy Cattle	15.00	80	13.37	0.307
3. Breeder Pigs	2.00	80	24.84	0.217
4. Piglets	0.50	80	24.84	0.217
5. Fattening Pigs	1.20	80	24.84	0.217
6. Chickens	0.03	80	23.34	0.242

Table 4 Agricultural waste biogas production rate [8]

Types	Waste	Ratio of Waste to product mass (%)	Waste Unused Percentage (%)	Biogas production rate (L/kg(dry))	Dry Material to Raw Material (%)
1. Rice	Straw	29.37	39.40	162 (Fresh)	-
	Trunk	43.52	73.71	250	70
2. Corn	Leaves	30.97	100	225	90
	Stubble	21.26	73.64	344	90
3. Sugarcane	Leaves and Shoots	39.51	93.24	262	70
4. Cassava	Stems and Leaves	28.93	14.87	274	65
	Rhizome	17.12	90.25	141	65

2.1.4 Systems of closed-loop circular economies in the agriculture sector

A closed-loop system that minimizes waste, maximizes resource efficiency, and supports sustainable practices is the goal of the circular economy for agriculture. Creating and executing systems that reduce waste, encourage resource efficiency, and uphold the sustainability of agricultural operations are all part of the circular economy approach to agriculture. [4–7]

A closed-loop system that optimizes resource use and minimizes environmental effect is created when waste from one operation becomes a valuable input for another, a concept inspired by natural ecosystems. In agriculture, it can be used as follows:

1) Waste Reduction and Valorization:

- Using anaerobic digestion and composting will create nutrient-rich compost and biogas from organic waste (food scraps, crop residues).

- Utilize agricultural leftovers and byproducts as a feedstock to produce bioenergy or other goods with added value.

2) Closed-loop Systems:

- Combine crop production with livestock farming so that crop wastes may be used as animal feed and animal waste can be used as a source of nutrients for crops.

- Creating integrated agricultural systems that employ animal manure as a resource as opposed to a pollution source. Using manure as fertilizer or turning it into biogas to produce electricity are two examples.

Figure 1 illustrates the agricultural sector's closed-loop circular economy systems. This study aims to illustrate with the closed-loop red arrow. The following is a succinct explanation: Anaerobic digestion occurs in tanks for the fermentation of animal and agricultural waste. Methane (CH_4) gas and other necessary gas components were the result. Plant food will be made from the organic fertilizer that remains after this procedure is finished. Heat and electrical energy are produced from the decomposed methane gas.

Thailand has always produced biogas from livestock and agricultural waste and occasionally used it as fuel as part of a closed-loop waste reduction scheme. However, the utilization of biogas for energy generation is still relatively new. In addition to completing this system, producing power from biogas can help Thailand achieve more resilient, efficient, and sustainable energy systems that strike a balance between social and environmental well-being and economic growth.
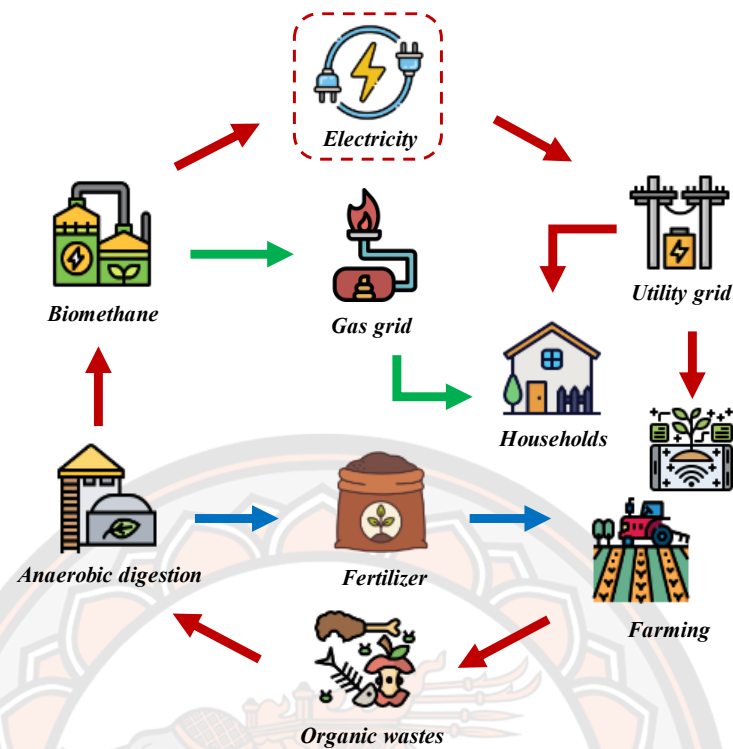
Figure 1 The closed-loop circular economy systems for the agricultural sector [4–7]

2.2. Introduction to Self-Excited Induction Generators:

Electric power can be converted into mechanical work in many applications using induction machines. The induction machine's main benefits are its durable brushless design and the absence of a separate DC field power requirement. These devices, which range in capacity from fractional horsepower (FHP) to multi-megawatt, are incredibly dependable and cost-effective. Furthermore, induction machines have variable speed operation, which sets them apart from synchronous machines. Many micropower generation systems use induction machines as an electrical generator because of their affordability and dependability. For example, A wind turbine powers these machines via a gearbox. Because lower rotational speeds on the wind turbine side must be transferred to high rotor speeds on the other, gearboxes are necessary.

Based on the rotor architecture, there are two types of induction machines: the wound rotor type and the squirrel cage type. Due to its affordability, ease of use, and durability, squirrel cage rotor architecture is a common choice for standalone

power generation projects. In grid-connected power generation systems, a wound rotor machine is the favored option due to its high beginning torque. The capacity to extract rotor power at the additional expense of power electronics in the rotor circuit is another benefit of a wound rotor.

The stator, which receives three-phase current and is composed of several coils with three groups (phases), is a component of the induction machine's electromagnetic structure. The three coils carry currents that are out of time-phase and are physically dispersed across the stator perimeter (space-phase). An essential component of the induction machine's operation is the rotating magnetic field that is produced by this combination. When motoring, induction machines operate at a speed below synchronous speed, and when generating, they operate at a speed above synchronous speed. When there is negative resistance, or when slip is negative, the induction machine.

Structure of self-excited induction generator like a squirrel cage induction motor, they are normally called an induction machine. When the induction machine work is a motoring mode, the mechanical speed (n_m) less than the synchronous speed (n_s), is giving by

$$n_s = \frac{120 f_s}{p} \tag{1}$$

where n_s is the synchronous speed, f_s is the frequency in the stator winding, and P is a number of magnetic poles.

On the other hand, if the mechanical speed (n_m) less than the synchronous speed (n_s), the induction machine will be worked as a generating mode. The difference in speed is defined by the slip (S), is given by

$$S = \frac{(n_s - n_m)}{n_s} \tag{2}$$

The relation between torque and rotational speed as shown in Figure 2 when the actual speed of the induction motor (4.5 kW 4 poles) is controlled to be equal to 1,500 rpm, the torque is a negative value at 47.60 Hz causes the mechanical power is feed in a shaft of the machine.
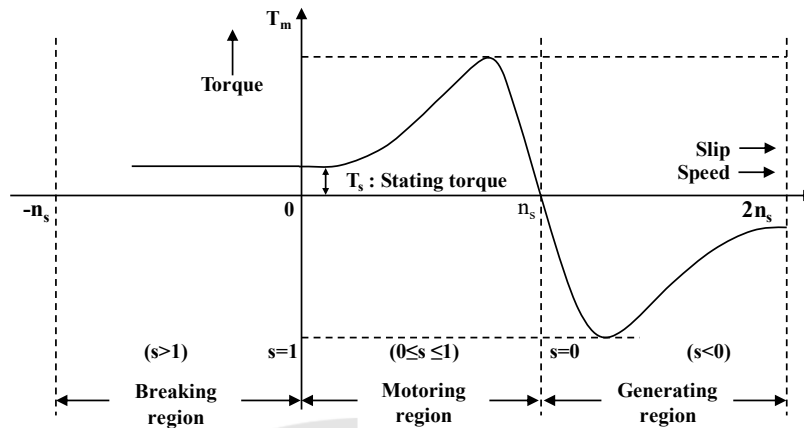
Figure 2 The relation between torque and rotational speed.

The induction machine requires a reactive power supply (Q) to excite the rotor, the voltage at the stator winding to gradually increase. The reactive power can be generated by a capacitor bank and stator winding in parallel as shown in Figure 3(a). When the mechanical load or shaft speed is altered, the capacitor bank is adjusted to compensate for the voltage in the operating regional's rotor and stator are the sources of power during the generating mode.

(a) Three-phase system.   (b) Single-phase system.
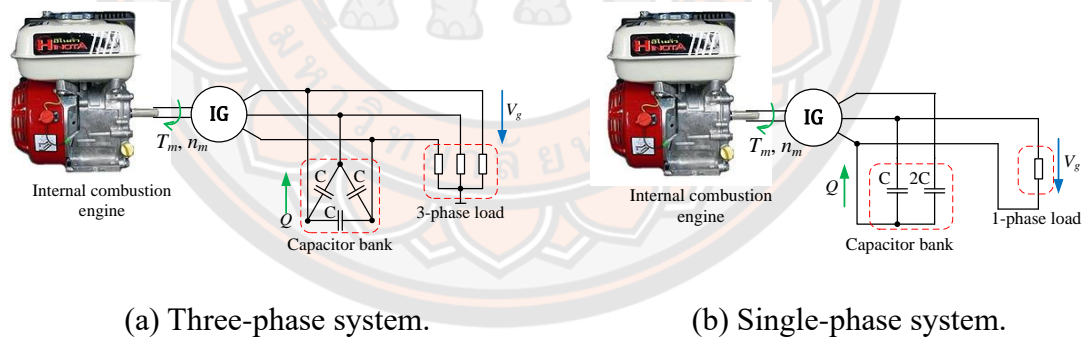
Figure 3 The connected induction generator with the capacitor bank for excitation

Figure 3(b). shows the suitable three-phase induction generator is connected to supply power to the single-phase loads by using a capacitor bank C-2C type, which is commonly used in the small hydropower plant in a rural area without electricity utility. However, the C-2C is necessary to connect with a dummy load for a balanced three-phase current when the generator is operated in low- load, cause the maximum output power is 80 percent of the rated power of the generator.

2.1.1 Equivalent electrical circuit of induction machine

The per-phase equivalent circuit seen in Figure 4 represents the theory of operation of an induction machine [33, 34].
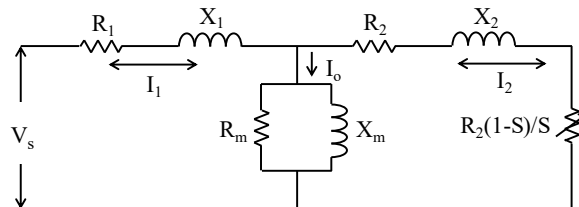
Figure 4 shows the induction machine's equivalent circuit for each phase with respect to the stator.

The resistance and inductive reactance are denoted by R and X, respectively, in the above diagram. The stator is denoted by subscripts 1, 2, and m, whereas the stator side and magnetizing components are denoted by rotor values, respectively.

To operate, induction machines require an AC excitation current. Either external or self-excitation is present in the machine. Shunt capacitors allow a stand-alone system to self-excite as the excitation current is primarily reactive. When operating in a grid-connected manner, it obtains its excitation power from the network, and the grid sets the output voltage and frequency. Local capacitors can be utilized to partially supply the required reactive power in situations where the grid's ability to deliver it is constrained [33, 34].

2.1.2 Self-Excited Induction Generator (SEIG)

An excitation capacitor is linked across the stator terminals of a self-excited induction generator (SEIG), which operates in the saturation region similarly to an induction machine. These devices are the best option for producing electricity in standalone variable-speed wind energy systems in situations where grid-reactive power is unavailable. If there is sufficient residual magnetic field in the rotor, the induction generator will use the external capacitor for self-excitation. The speed, the load, and the capacitance value in farads all have an impact on the generator's output

frequency and voltage in the self-excited mode. Figure 5 depicts the steady-state per-phase equivalent circuit of a self-excited induction generator [33 – 35].
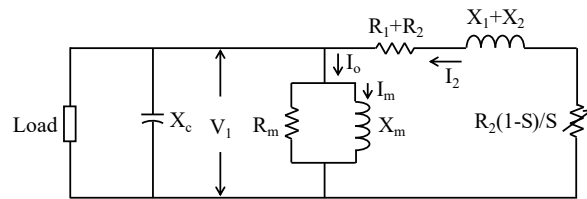
Figure 5 shows an externally capacitor-powered self-excited induction generator.

For many years, the self-excitation mechanism of induction machines has been understood [33 – 35]. An induction machine powered by an external prime mover will induce voltage at its terminals when capacitors are connected across the stator terminals. The machine's magnetic saturation will cause the induced electromotive force (*EMF*) and current in the stator windings to increase until the steady-state condition is reached. The voltage and current will stabilize at this operating point at a specific peak value and frequency. For a given capacitance value, there is a matching minimum speed required for the self-excitation to occur [33 – 35]. Consequently, the induction generator must run in the saturation area when operating in stand-alone mode. This ensures output voltage stability under load and, as shown in Figure 6, one and only one intersection between the magnetization curve and the capacitor reactance line.
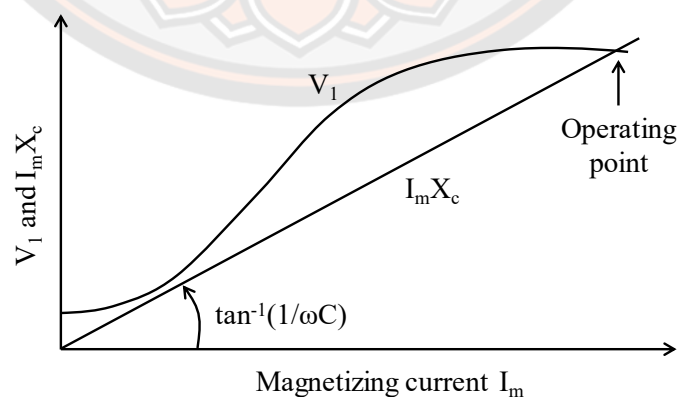
Figure 6 Determining the self-excited induction generator's steady operation.

The magnetizing current $I_m = \frac{V_1}{X_m}$ and the capacitor current $I_c = \frac{V_1}{X_c}$ must be equal when there is no load. The voltage V_1 increases linearly as a function of I_m until the magnetic core's saturation point is achieved. The self-excited generator has an output frequency of $f = \frac{1}{2\pi C X_m}$ and $\omega = 2\pi f$, where C is the self-exciting capacitance.

2.1.3 Steady-state analysis of induction generators

Induction generator steady-state analysis is interesting from both an operational and design perspective. It is feasible to ascertain the machine's performance at a specific speed, capacitance, and load conditions by understanding its parameters. The per-phase steady-state equivalent circuit of the induction machine (Figure 7), adjusted for the self-excitation scenario, serves as the foundation for both the loop impedance and nodal admittance techniques employed in SEIG analysis. By creating nodal equations or loop equations for the equivalent circuit, they apply the concept of conservation of active and reactive powers. These techniques work incredibly well for figuring out the lowest capacitance value required to ensure the induction generator will self-excite. Excitation capacitance needs to be marginally larger than the minimal value in order to operate steadily. Additionally, there exists a speed barrier known as the machine's cutoff speed below which no excitation is possible. For ease of comprehension, the loop impedance approach is provided in the paragraph that follows [33 – 35].

As illustrated in Figure 7, the per-unit per-phase steady-state circuit of a self-excited induction generator under RL load [33 – 35].
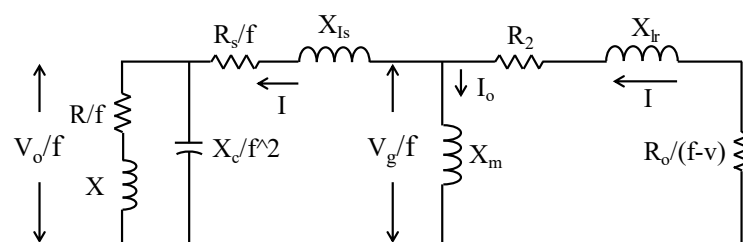
Figure 7 Self-excited induction generator equivalent circuit with R-L load.

Where:

R_s, R_r, and R stand for power-user per-phase stator, rotor (sometimes called stator), and load resistance, in that order. X_{ls}, X_{lr}, X, X_m: these represent the per-phase stator leakage, load, magnetizing reactances (at base frequency), and rotor leakage (referred to as stator), respectively.

The maximum saturated magnetizing reactance, or X_{smax}, is the p.u.

C is the terminal-excitation capacitance per phase.

X_c: the terminal excitation capacitor's p.u. per-phase capacitive reactance (at base frequency).

f, v stand for pulse-width and velocity, respectively.

N: initial velocity in rev/min

Z_b: base impedance per phase

V_g, V0 are the per-phase air gap and output voltages, respectively, while fb is the base frequency.

The following presumptions were made in the SEIG study:

1. It is considered that magnetic saturation only affects the magnetizing reactance X_m. and it is expected that every other parameter of the analogous circuit remains constant. The main flux becomes saturated as a result of self-excitation, and its magnitude is indicated by the value of X_m. Since leakage flux primarily moves through the air, the saturation of the primary flux has little impact on these fluxes.

2. It is assumed that the leakage reactance in units per unit of the stator and rotor are equivalent. In induction machine analysis, this assumption is typically true.

3. The machine's core loss is disregarded. Regarding the circuit depicted in Figure 7.

$$I\,Z = 0 \qquad\qquad (3)$$

Where Z is the net loop impedance given by

$$Z = \left(\left(\frac{Rr}{f-v} \right) + jX_{lr} \| jX_m \right) + \frac{Rs}{f} + jX_{ls} + \left(\frac{-jX_c}{f^2} \| \left(\frac{R}{f} + jX \right) \right) \tag{4}$$

Equation 1 indicates that $Z = 0$ for steady-state excitation $I \neq 0$, implying that Z's real and imaginary components are both zeros. It is possible to solve these two equations concurrently for any two unknowns, most often voltage and frequency. The load-capacitance combination and rotor speed must provide a value such that $X_m = X_{smax}$, which gives the lowest excitation capacitance value below which the SEIG fails to self-excite, in order for voltage accumulation to be successful.

2.4 Induction Motor Model

The dynamic model of an induction motor can be divided into electrical and mechanical components, considering the interaction between the stator and rotor.

2.4.1. Electrical Equations:

The electrical equations describe the behavior of the stator and rotor windings in the induction motor. These equations are often expressed in a dq −axis reference frame after applying Clarke and Park transformations.

a) Stator Voltage Equations:

$$v_{ds} = R_s i_{ds} + \frac{d\lambda_s}{dt} - s\omega_s\lambda_s \tag{5}$$
$$v_{qs} = R_s i_{qs} + s\omega_s\lambda_s \tag{6}$$

Where:

v_{ds} and v_{qs} are the stator voltage components in the dq reference frame.

i_{ds} and i_{qs} are the stator current components in the dq reference frame.

R_s is the stator resistance.

λ_s is the stator flux.

b) Rotor Voltage Equations

$$v_{dr} = R_r i_{dr} + \frac{d\lambda_r}{dt} - s\omega_r \lambda_r \qquad (7)$$
$$v_{qr} = R_r i_{qr} + s\omega_r \lambda_r \qquad (8)$$

Where:

v_{dr} and v_{qr} are the rotor voltage components in the dq reference frame.

i_{dr} and i_{qr} are the rotor current components in the dq reference frame.

R_r is the rotor resistance.

λ_r is the rotor flux.

2.4.2 Magnetic Field Equations

The magnetic field equations describe the interaction between the stator and rotor magnetic fields.

a) Stator Flux Equations:

$$\frac{d\lambda_s}{dt} = \frac{1}{L_s}(v_{ds} - R_s i_{ds} - s\omega_s \lambda_s) \qquad (9)$$

Where L_s is the stator inductance.

b) Rotor Flux Equations

$$\frac{d\lambda_r}{dt} = \frac{1}{L_r}(v_{dr} - R_r i_{dr} - s\omega_r \lambda_r) \qquad (10)$$

Where L_r is the rotor inductance.

4.2.3 Mechanical Equations:

The mechanical equations describe the rotor's motion and the interaction between the mechanical and electrical parts of the motor.

a) Rotor Motion Equation:

$$J\frac{d\omega_r}{dt} = T_{em} - T_{load} - T_{friction} \qquad (11)$$

Where:

J is the moment of inertia of the rotor.

ω_r is the rotor angular velocity.

T_{em} is the electromagnetic torque.

T_{load} is the external load torque.

$T_{friction}$ is the friction torque.

b) Electromagnetic Torque

$$T_{em} = \frac{2}{3}p\left(\lambda_s i_{qr} - \lambda_r i_{qs}\right) \tag{12}$$

Where p is the number of pole pairs.

2.5 Reference Frame Transformation:

In dynamic modeling of induction motors, reference frame transformation plays a vital role in simplifying the analysis by decoupling the equations and aligning them with the rotating fields in the machine. The transformation typically involves converting the three-phase quantities from the stationary reference frame (abc) to a rotating reference frame ($dq0$), commonly known as the Park transformation.

2.3.1 Park Transformation

The Park transformation is utilized to convert the three-phase quantities from the stationary abc reference frame to the rotating $dq0$ reference frame. This transformation is particularly useful for analyzing the steady-state and dynamic behavior of the induction motor under varying operating conditions. The Park transformation equations are defined as follows:

$$\left.\begin{array}{c} d = a\cos(\theta) + b\sin(\theta) \\ q = -a\sin(\theta) + b\cos(\theta) \\ 0 = c \end{array}\right\} \tag{13}$$

And

$$\left.\begin{array}{l} d=\alpha \cos(\theta)+\beta \sin(\theta) \\ q=-\alpha \sin(\theta)+\beta \cos(\theta) \end{array}\right\} \qquad (14)$$

Where:

$a, b,$ and c represent the three-phase quantities in the stationary abc reference frame.

d and q represent the transformed quantities in the rotating $dq0$ reference frame.

α and β represent the two-phase quantities in the stationary $\alpha\beta$ reference frame.

θ represents the electrical angle, which is typically the angle of the rotor flux with respect to the stator.
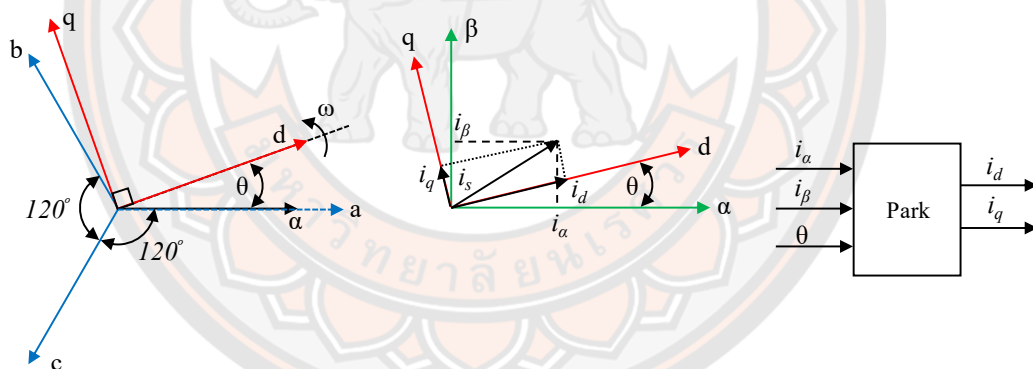
Figure 8 Visualization of Park Transformation. The three-phase stator variables (a, b, c) are transformed into the two-phase rotating reference frame (d and q).

In Figure 8, the blue vector represents the original three-phase stator quantities in the stationary abc reference frame. After the Park transformation, the red vector represents the transformed quantities in the rotating dq reference frame. The angle θ is the electrical angle, illustrating the rotation of the reference frame.

2.3.2 Inverse Park Transformation

The inverse Park transformation converts the quantities back from the rotating dq reference frame to the stationary abc reference frame.

$$\left.\begin{array}{c} c = d\cos(\theta) - q\sin(\theta) \\ b = d\sin(\theta) + q\cos(\theta) \\ 0 = -(a + b) \end{array}\right\} \tag{16}$$

And

$$\left.\begin{array}{c} \alpha = d\cos(\theta) - q\sin(\theta) \\ \beta = d\sin(\theta) + q\cos(\theta) \end{array}\right\} \tag{17}$$

Where:

$a, b,$ and c are the three-phase stator variables in the stationary abc reference frame.

d and q are the two-phase rotating quantities.

α and β represent the two-phase quantities in the stationary $\alpha\beta$ reference frame.
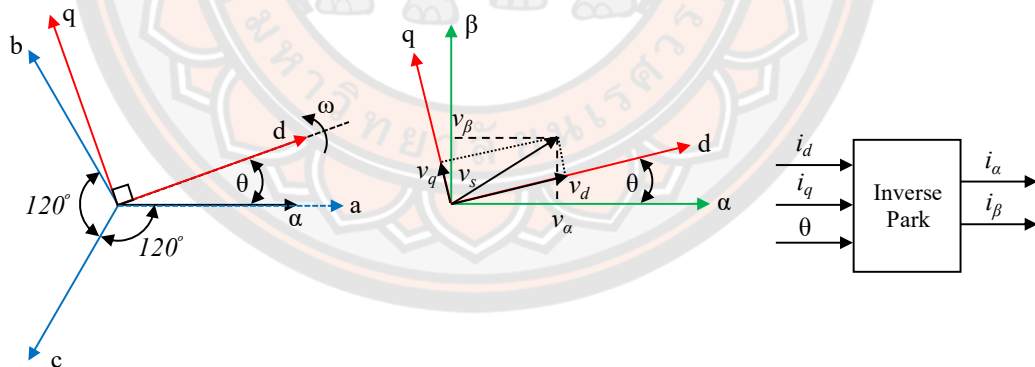
Figure 9 *Visualization of Inverse Park Transformation. The red vector represents the transformed quantities in the rotating dq reference frame. After the inverse Park transformation, the blue vector represents the quantities in the stationary abc reference frame.*

In Figure 9, the red vector represents the transformed quantities in the rotating dq reference frame. After the inverse Park transformation, the blue vector represents the quantities in the stationary abc reference frame. The angle θ is the electrical angle, and the rotation is reversed.

Reference frame transformations, as illustrated in Figures 8 and 9, are crucial in simplifying the analysis of induction motor dynamics, providing a clearer understanding of the motor's behavior in different reference frames.

2.3.3 Clarke Transformation

The Clarke Transformation is used to convert three-phase variables ($a, b,$ and c) in the stationary abc reference frame into two-phase variables (α and β) in a stationary $\alpha\beta$ reference frame. This transformation is particularly useful when analyzing unbalanced conditions or when only two-phase quantities are available. The Clarke Transformation equations are as follows:

$$\left.\begin{array}{l} \alpha = a \\ \beta = 1/\sqrt{3}\,(a+2b+c) \end{array}\right\} \tag{18}$$

Where:

α and β represent the two-phase quantities in the stationary $\alpha\beta$ reference frame.

$a, b,$ and c represent the three-phase quantities in the stationary abc reference frame.
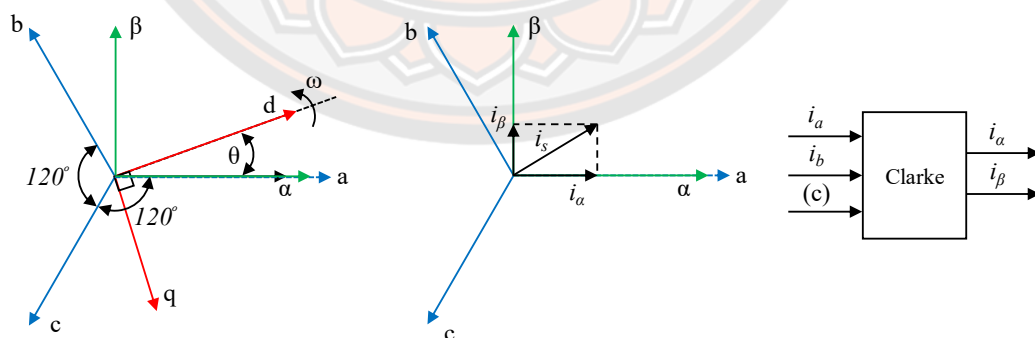
Figure 10 Visualization of Clarke Transformation. The three-phase variables (a, b, c) are transformed into the two-phase stationary αβ reference frame (α and β).

In Figure 10, the blue vector represents the original three-phase variables in the stationary abc reference frame. After the Clarke transformation, the green vector represents the transformed variables in the stationary $\alpha\beta$ reference frame.

2.3.4 Inverse Clarke Transformation

The inverse Clarke transformation converts the quantities back from the two-phase stationary $\alpha\beta$ reference frame to the three-phase stationary abc reference frame. The inverse Clarke transformation equations are given by:

$$\left.\begin{array}{l} a = \alpha \\ b = -\frac{1}{2}\left(\alpha - \sqrt{3}\beta\right) \\ c = -\frac{1}{2}\left(\alpha + \sqrt{3}\beta\right) \end{array}\right\} \tag{19}$$

Where:

$a, b,$ and c represent the three-phase quantities in the stationary abc reference frame.

α and β represent the two-phase quantities in the stationary $\alpha\beta$ reference frame.
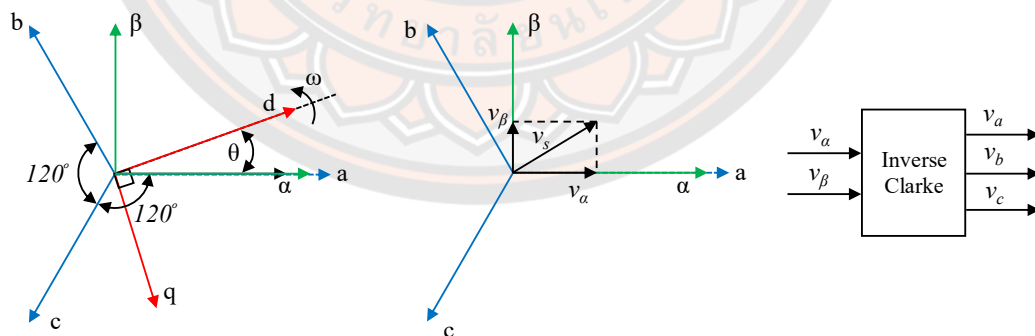
Figure 11 Visualization of Inverse Clarke Transformation. The red vector represents the transformed variables in the stationary αβ reference frame. After the Inverse Clarke transformation, the blue vector represents the variables in the stationary abc reference frame.

In Figure 11, the red vector represents the transformed variables in the stationary $\alpha\beta$ reference frame. After the Inverse Clarke transformation, the blue vector represents the variables in the stationary abc reference frame.

Clarke Transformation, when combined with Park Transformation, provides a comprehensive framework for analyzing induction motor dynamics in different reference frames, facilitating the implementation of advanced control strategies.

The reference frame transformation simplifies the analysis of induction motor dynamics, allowing for a clearer understanding of the motor's behavior in different reference frames. It facilitates the implementation of control strategies such as field-oriented control and simplifies the computation of motor equations in dynamic simulations.

2.6 Related Works and Studies

Ahmed et al., [39] present the thyristor to combine the capacitor (Thyristor switched capacitor, TSC) to control the reactive power for self-excited induction motor and control the voltage of the generator as shown in Figure 12. The three-phase rectifier can be converted to an AC generated output voltage to a DC constant voltage by using the PI controller, which controls the amount of reactive power to motivate the rotor of the induction generator. The advantage of this method is the generator can operate in an extensive range of speed, but there was the harmonics distortion in the TSC and the rectifier cause the power losses in the system.
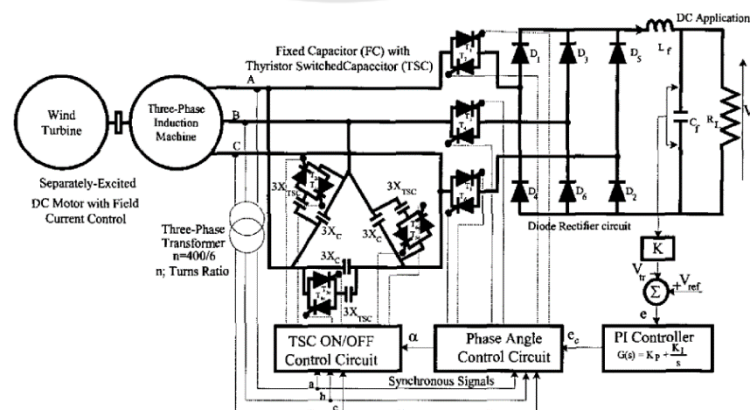
Figure 12 The schematic system configuration of a three-phase induction generator voltage control by the TSC control circuit [39].

Nanba et al., [40] present a basic control system for the induction generator by using a constant capacitor bank and adjustable rectifier as shown in Figure 13., which is suitable for low power systems because of the DC link voltage must be lower than the generator output voltage. The range of speed is appropriate with only one capacitor value and also have a harmonics distortion as well as [39].
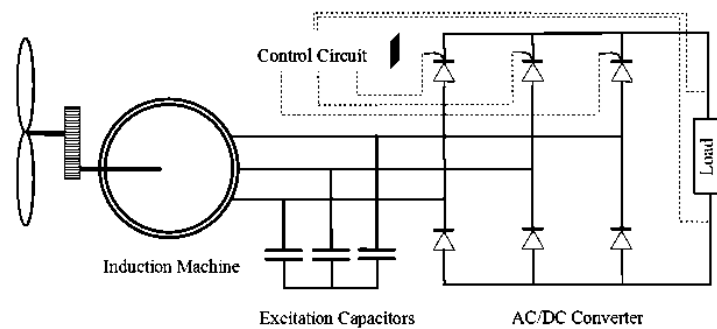
Figure 13 Schematic diagram of the proposed DC power generator [40].

Kimura et al.,[41] present the reduction of a harmonics distortion in the power rectifier by using the power factor correction (PFC) as the main three-phase converter circuit, and use the voltage source inverter (VSI) combine with a constant capacitor bank for self-excited induction generator, that can adjust the voltage to be suitable to load and speed as shown in Figure 14.
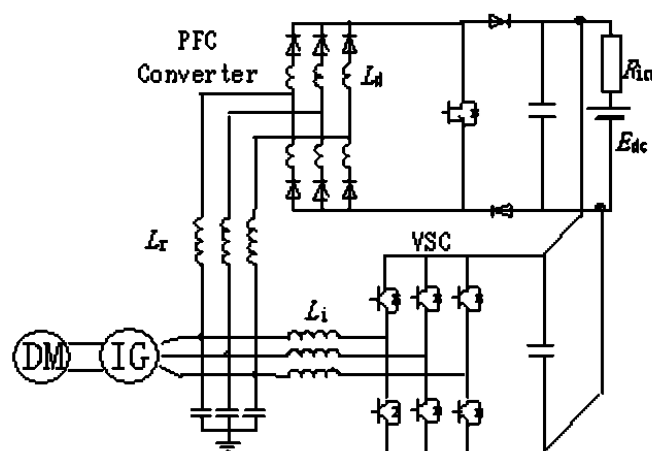
Figure 14 The system of inverter excited induction generator and the PFC converter to transfer the real power [41].

The operation of a self-excited induction generator under the broad range of load and speed as a wind generator is necessary to a more efficient control system. The control system such as field-oriented control as shown in Figure 15. [39], [42] - [48], which a current generator control is controlled in torque and magnetic field by using the stationary frame (abc) to rotating (dq) axis transformation of the measured voltages currents and shaft speed of the generator. However, the speed can be estimated from the voltages and currents by using the observer [49] but that reduced performance. In addition to the field-oriented control system, direct torque control (DTC) is another way to be similar.
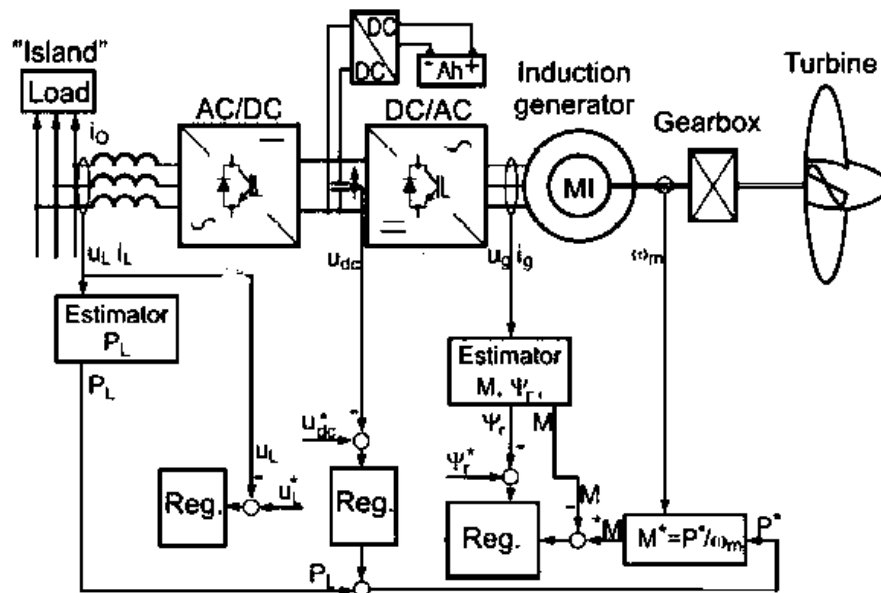
Figure 15 the field-oriented control system [46].

Yuttana Khamsuwan, presents the developed self-excited induction generator control system with direct torque control. This controls the ratio of voltage to frequency of the stator winding to be constant which is suitable for application as a stand-alone three-phase power generation system [47].

Li Yingjian et al., presents the analysis of the energy balance of power generation systems from biogas using internal combustion engines as shown in Figure 16. The results this the power generation system has efficiency equal to 28.45% and the total efficiency is 87.05% at 70 kW maximum power [48].
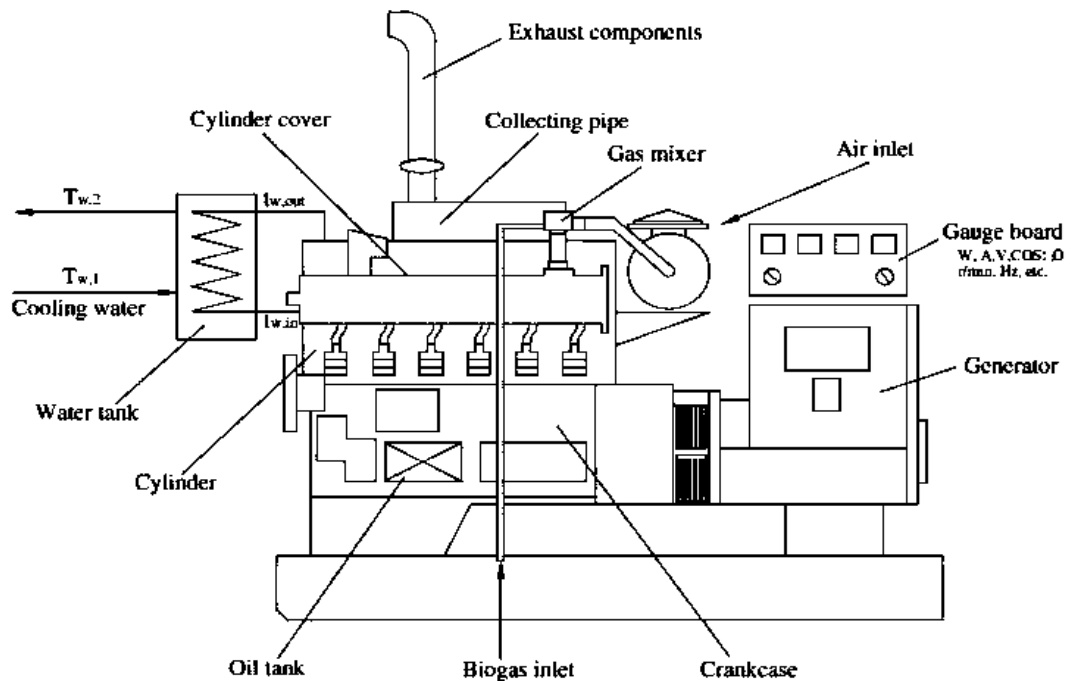
Figure 16 The power generation in internal combustion engine sets using biogas [48].

Kultida Sawangpol et al., [49] present the electric power generation using biogas from cellulosic materials produced from lignocellulosic agricultural residues, consists of rice straw and sugarcane tops and leaves. they using an Up-flow anaerobic sludge-fixed film fermentation process, and a continuous stirred-tank reactor. was selected for feedstock pretreatment. Levelized unit costs from the calculation for the cases of 187 kW to 1,966 kW biogas engines were 9.29 Baht/kWh to 4.77 Baht/kWh for rice straw and 11.29 Baht/kWh to 6.21 Baht/kWh for sugarcane top and leaves, respectively.

CHAPTER III

RESEARCH PROCEDURES OF THE STUDY

3.1 Proposed Biogas Power Generation System

3.1.1 Selection and Modification of a Spark-ignition Engine

A 4-stroke, air-cooled, spark-ignition Honda GX200T2 QHT engine with a horizontal shaft was selected as the prime mover [50]. The engine specs are listed in Table I. The engine's power-speed and torque-speed parameters were mimicked from the specification sheet, as depicted in Figure 17. According to the SAE J1349 standard, the maximum output power is 4.1 kW at 3,600 revolutions per minute (rpm) and the maximum torque is 12.4 N/m at 2,500 rpm. Moreover, the GX200T2 QHT engine can run on gasohol, a blended fuel with a maximum ethanol percentage of 10% that combines gasoline and ethanol. As a result, this engine can be directly coupled to a two-pole machine that runs at a nominal speed of about 3,000 rpm. The gasoline/liquefied petroleum gas (LPG) carburetor conversion kit shown in Figure 18 was used in place of the original carburetor. Biogas can also be fed into the engine thanks to its dual-fuel carburetor [25].
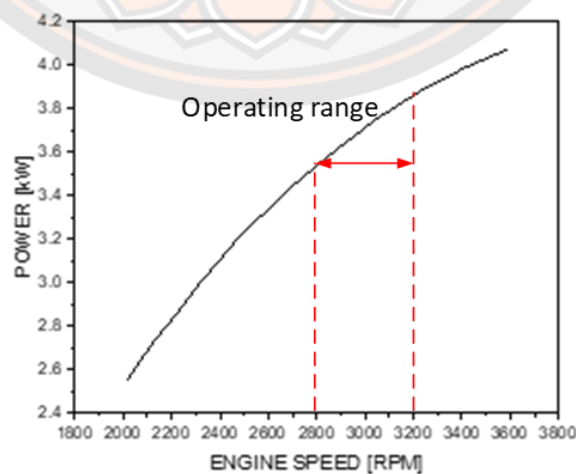
Figure 17 *Mechanical characteristics of the Honda GX200T2 QHT engine.*
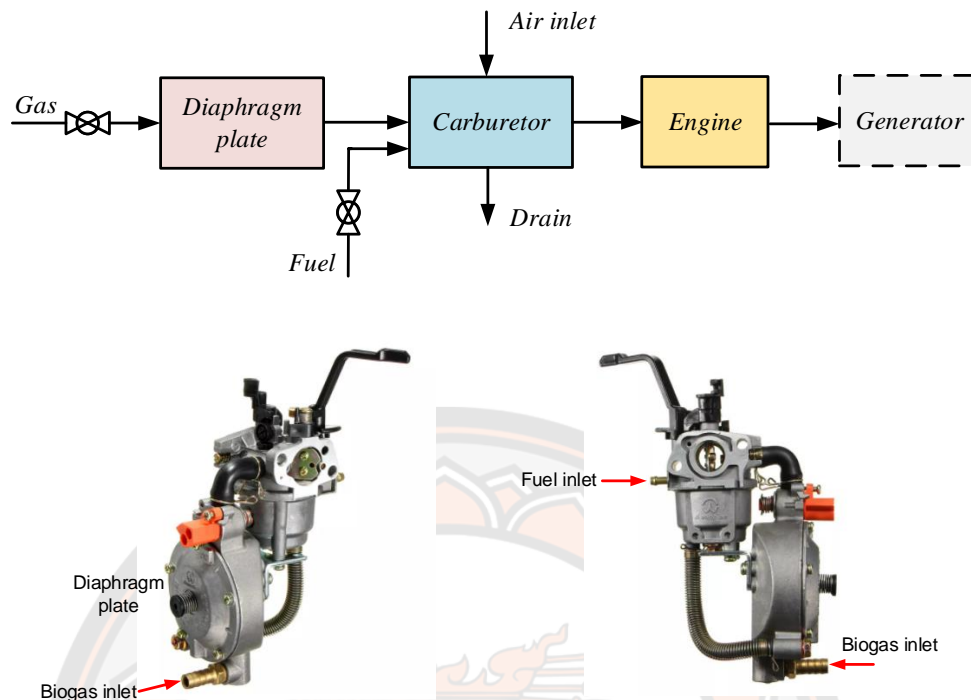
Figure 18 Biogas supply system for the spark-ignition engine.

3.1.2. Power Conversion Topologies

The Hitachi TFO-K series 220/380 V 2.2-kW 2-pole squirrel-cage induction motor, the SEIG, is the model used for this study. This system's output is connected to a single-phase AC grid that operates at 220-volts and 50 Hz, requiring a minimum DC input voltage of V. Because of the unregulated engine speed, there is variation in the generator's output voltage and frequency. To increase the generator terminal voltages from a residual flux density in the rotor core, the SEIG needs a bank of capacitors. In order to maintain the SEIG's excitement while delivering the load, an additional reactive power source is also required [39].

Proposed circuit topologies for this investigation are shown in Figure 19. The passively excited SEIG with the star connection in Figure 19(a). When there is no load, the capacitor bank CB1 provides a reactive power source for the initial excitation, resulting in a nominal line-to-line voltage of about 380 V [30, 50]. An LCL-filtered single-phase insulated-gate bipolar transistor (IGBT) inverter receives the DC bus voltage of roughly 550 V, which is converted from the three-phase AC

voltage by a passive rectifier. When delivering active power to the grid, the capacitor bank CB2 provides additional reactive power for voltage management. The DC bus voltage in this circuit is significantly higher than the peak grid voltage value, despite its straightforward functioning. Due to the high bus voltage, the LCL filter has a large inverter-side inductor to limit current ripple, a high inverter switching loss, and high ratings for semiconductor components.

Furthermore, the rectifier's distorted current demand contributes to the generator's low efficiency. Smooth voltage regulation is achieved by hybrid excitation techniques in Figure 19(b) that use a static voltage generator (SVG) to supply reactive power [35, 36, 52]. As the boosting inductors, a voltage source converter (VSC) is used as the SVG [35]. In order for the VSC to inject reactive power into the generator for voltage regulation, the bus voltage of the VSC is adjusted to be higher than the peak value of the SEIG line-to-line voltage. Furthermore, in order to make the SEIG currents sinusoidal, the SVG can correct for the rectifier's current harmonics. The control system and circuit topology are too complex for low-power applications. The VSC-based SVG may be replaced with a thyristor-based SVG [33, 53]. Low system efficiency is still caused by the SEIG current harmonics and high DC bus voltage, though.

The suggested back-to-back converter topology is displayed in Fig. 3(c). With a suitable capacitor bank CB1, the SEIG winding is linked in a delta configuration so that the line-to-line voltage at no load is roughly 220 V. The SEIG 3-phase AC voltage is converted to a DC voltage greater than the peak value of the line-to-line input voltage using a VSC-based PWM rectifier, a boost-type power converter. It is sufficient for the single-phase inverter with a lower IGBT rating and switching loss because the DC bus voltage reference value is 400 V. In addition to pulling active power, the VSC-based PWM rectifier provides the SEIG with reactive power. Because of the SEIG sinusoidal currents and reduced switching losses, the suggested topology is anticipated to outperform the passive rectifier configurations depicted in Figures 19(a) and 19(b) because of the sinusoidal currents generated by the SEIG and reduced losses from switching.
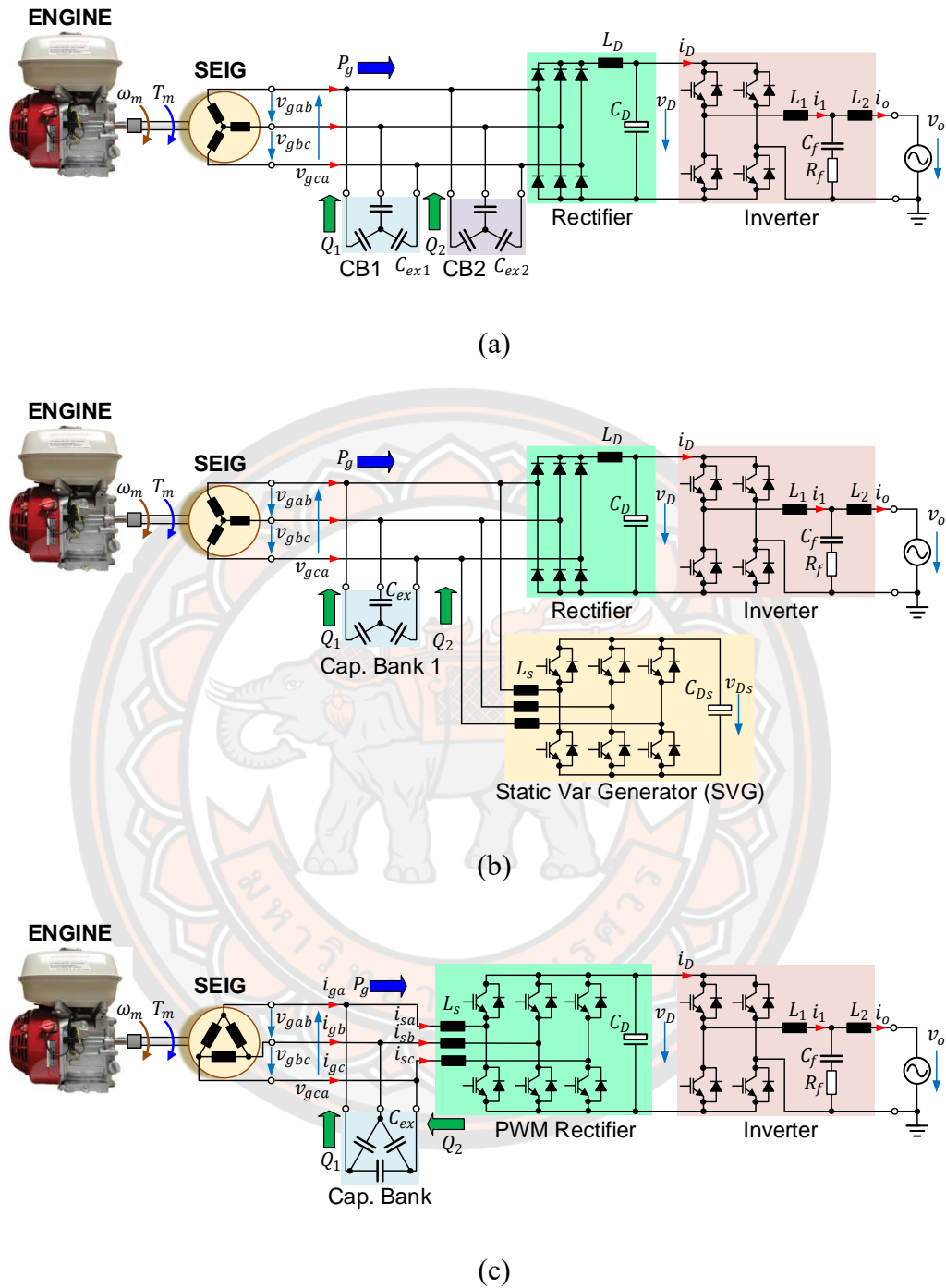
Figure 19 Possible power conversion topologies for the biogas power generation system: (a) Passive rectifier with multi capacitor banks, (b) Passive rectifier with a capacitor bank and an SVG, (c) Proposed back-to-back converter with a capacitor bank.

3.2 Proposed Power Conversion System

Figure 20 illustrates the power converter control system. The control schemes for the SEIG-side and grid-side are executed using a TMS320F28069 32-bit microcontroller manufactured by Texas Instruments. Voltage and current signals from both the SEIG and grid are sampled using the embedded analog-to-digital converters (ADCs). These signals are then used by the control schemes to generate switching signals for the IGBTs through the gate driver circuits. The SEIG and capacitor bank are treated as a 3-phase AC voltage source with a star connection. Consequently, the virtual phase voltages of the SEIG are defined as follows:

$$\left.\begin{array}{c} v'_{ga}(t) = \hat{V}'_g \cos \omega_g t \\ v'_{gb}(t) = \hat{V}'_g \cos \left(\omega_g t - \frac{2\pi}{3}\right) \\ v'_{gc}(t) = \hat{V}'_g \cos \left(\omega_g t - \frac{4\pi}{3}\right) \end{array}\right\}$$

(20)

The amplitude of the virtual grid voltage $\hat{V}'_g$ is given by $\sqrt{2}\left(\frac{V_{LL}}{\sqrt{3}}\right)$, where V_{LL} represents the voltage amplitude and ω_g denotes the electrical frequency of the generator. The actual shaft rotational speed is not directly necessary; instead, the shaft speed can be approximated using the generator frequency ω_g. This estimation will be utilized for supervisory control in conjunction with other mechanical parameters such as temperatures, biogas pressure, and gas flow rate.
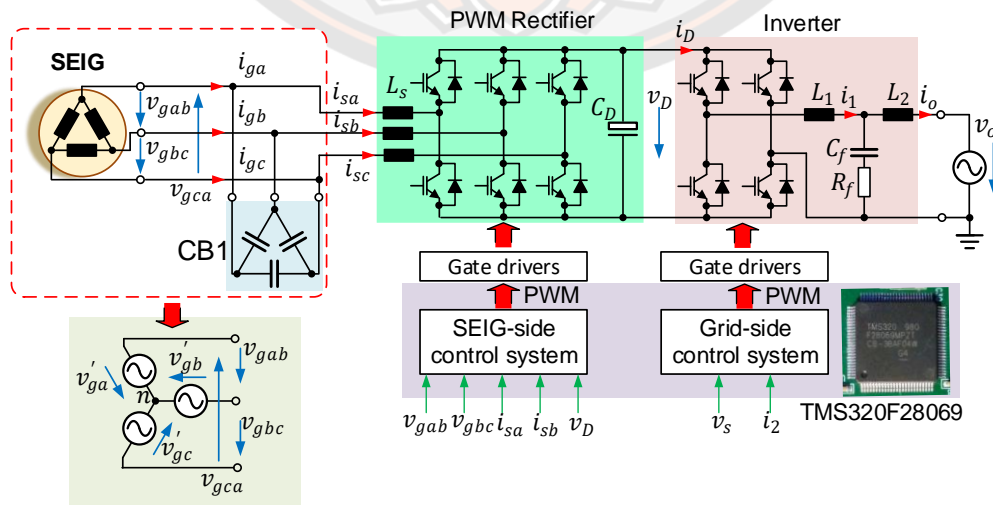
Figure 20 Control structure of the biogas power generation system.

3.2.1 SEIG-Side Power Conversion Topologies

The control system of the PWM rectifier in the synchronous reference frame, depicted in Figure 21, utilizes reference signals denoted by $'*'$. The measured line-to-line voltages $v_{gab}(t)$ and $v_{gbc}(t)$ are transformed into a space vector, which undergoes a shift by $\frac{e^{-\frac{j\pi}{6}}}{\sqrt{3}}$ to derive the space vector $v'_{g\alpha}(t) + jv'_{g\beta}(t)$ representing the virtual phase voltages $v'_{ga}(t)$, $v'_{gb}(t)$, and $v'_{gc}(t)$. A synchronous reference frame phase-locked loop (PLL) estimates the angle $\hat{\theta}_g$, frequency $\hat{\omega}_g$, and amplitude $\hat{V}'_g$ of the space vector $v'_{g\alpha}(t) + jv'_{g\beta}(t)$. The PWM rectifier currents $i_{sa}(t)$ and $i_{sb}(t)$ are solely measured owing to the symmetry of the 3-phase 3-wire system, enabling the transformation of the synchronous reference frame currents $i_{sd}(t)$ and $i_{sq}(t)$. Consequently, the instantaneous active and reactive powers $p_s(t)$ and $q_s(t)$ of the PWM rectifier are determined as:

$$p_s(t) = \frac{3}{2}\hat{V}'_g i_{sd}(t) \tag{21}$$

$$q_s(t) = \frac{3}{2}\hat{V}'_g i_{sq}(t) \tag{22}$$

Under the assumption of no loss in the capacitor bank, the active power $p_g(t)$ and reactive power $q_2(t)$ of the Synchronous Electric Induction Generator (SEIG) are altered as follows.

$$p_g(t) = p_s(t) = \frac{3}{2}\hat{V}'_g i_{sd}(t) \tag{23}$$

$$q_2(t) = q_s(t) = \frac{3}{2}\hat{V}'_g i_{sq}(t) \tag{24}$$

To address the ripple in the DC bus voltage $v_D(t)$ caused by the oscillating power of the grid-side inverter at a frequency of $2\omega_o$ (where $\omega_o = 2\pi f_o$ represents the grid frequency), a second-order notch filter $G_{NF}(s)$ is utilized at $2\omega_o$ to diminish the bus ripple before entering the bus voltage control loop. This control loop integrates a proportional-integral (PI) controller $G_{PI1}(s)$. Subsequently, the bus voltage controller generates the d-axis reference current $i^*_{sd}(t)$ to regulate the active

power $p_s(t)$ drawn from the Synchronous Electric Induction Generator (SEIG) in response to the bus power consumed by the single-phase inverter.

To address the voltage regulation challenges of a variable-speed Synchronous Electric Induction Generator (SEIG), which exhibits nonlinear characteristics, we propose a straightforward open-loop excitation scheme, leveraging the proximity of the mechanical speed typically ranging between 2,800-3,200 rpm to the nominal synchronous speed of 3,000 rpm. In this scheme, the q-axis reference current $i_{sq}^*(t)$ is directly related to $i_{sd}^*(t)$ by a constant gain K_q, aiming to generate the reactive power $q_2(t)$ for SEIG voltage regulation. The direction of $q_2(t)$ is determined by the sign of the estimated SEIG frequency $\widehat{\omega}_g$, especially in scenarios where the phase sequence deviates from the conventional one. PI controllers $G_{PI2}(s)$ are employed to regulate the dq-axes currents, while a space vector modulation (SVM) technique is utilized to generate switching signals for the Insulated Gate Bipolar Transistors (IGBTs).
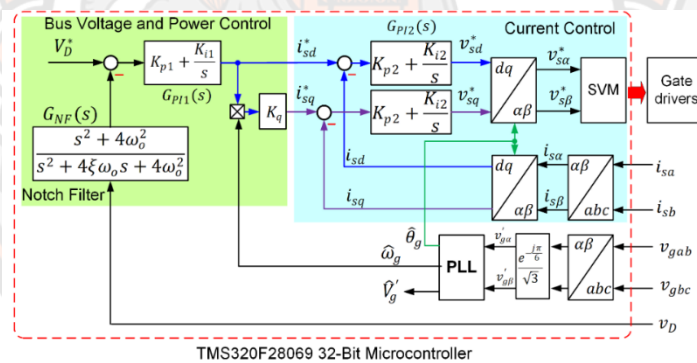
Figure 21 SEIG-side power converter control system.

The $2\omega_o$ ripple component in the bus voltage influences the waveforms of the PWM rectifier and Synchronous Electric Induction Generator (SEIG) currents. Figure 21 illustrates the natural reference frame equivalence of the control system on the SEIG side. The Proportional-Integral (PI) controllers within the current control loops depicted in Figure 6 can be likened to proportional-resonant controllers operating at the resonant frequency of ω_g. The bus voltage filter $G_{fv}(s)$ is designed to attenuate the $2\omega_o$ component $\tilde{v}_{D2\omega_o}$. Let the reference current $i_{sd}^*(t)$ be denoted as:

$$i_d^*(t) = \hat{I}_g^* + \hat{I}_{2\omega_o} \cos(2\omega_o t + \psi) \tag{24}$$

where $\hat{I}_g^*$ represents the active power-producing component, and $\hat{I}_{2\omega_o} \cos(2\omega_o t + \psi)$ represents the resultant of the $2\omega_o$ component. The reference currents i_{sa}^*, i_{sb}^*, and i_{sc}^* in the natural reference frame are derived from

$$\begin{bmatrix} i_{sa}^* \\ i_{sb}^* \\ i_{sc}^* \end{bmatrix} = \begin{bmatrix} \cos \omega_g t & -\sin \omega_g t \\ \cos\left(\omega_g t - \frac{2\pi}{3}\right) & -\sin\left(\omega_g t - \frac{2\pi}{3}\right) \\ \cos\left(\omega_g t - \frac{4\pi}{3}\right) & -\sin\left(\omega_g t - \frac{4\pi}{3}\right) \end{bmatrix} \cdot \begin{bmatrix} i_{sd}^* \\ i_{sq}^* \end{bmatrix} \qquad (25)$$

Let $i_{sq}^*(t) = k_q i_{sd}^*(t)$ and consider only the $2\omega_o$ component of $i_{sd}^*(t)$, which causes inter harmonic components $i_{sa,2\omega_o}^*$, $i_{sb,2\omega_o}^*$, and $i_{sc,2\omega_o}^*$ in the natural frame reference currents i_{sa}^*, i_{sb}^*, and i_{sc}^* as

Let $i_{sq}^*(t) = k_q i_{sd}^*(t)$ and focus solely on the $2\omega_o$ component of $i_{sd}^*(t)$, which gives rise to interharmonic components $i_{sa,2\omega_o}^*$, $i_{sb,2\omega_o}^*$, and $i_{sc,2\omega_o}^*$ in the natural frame reference currents i_{sa}^*, i_{sb}^* and i_{sc}^* as follows:

$$\begin{bmatrix} i_{sa,2\omega_o}^* \\ i_{sb,2\omega_o}^* \\ i_{sc,2\omega_o}^* \end{bmatrix} = \pm \frac{\hat{I}_{2\omega_o}}{2} \begin{bmatrix} \cos\left((2\omega_o \mp \omega_g)t + \psi\right) + k_q \sin\left((2\omega_o \mp \omega_g)t + \psi\right) \\ \cos\left((2\omega_o \mp \omega_g)t - \frac{2\pi}{3} + \psi\right) + k_q \sin\left((2\omega_o \mp \omega_g)t - \frac{2\pi}{3} + \psi\right) \\ \cos\left((2\omega_o \mp \omega_g)t - \frac{4\pi}{3} + \psi\right) + k_q \sin\left((2\omega_o \mp \omega_g)t - \frac{4\pi}{3} + \psi\right) \end{bmatrix} \quad (26)$$

Hence, the bus voltage filter $G_{fv}(s)$ assumes a critical function in attenuating the $(2\omega_o \mp \omega_g)$ components in the PWM rectifier currents. Employing a low-pass filter with a cutoff frequency significantly below $2\omega_o$ would result in sluggish performance. In this investigation, we utilize a standard second-order notch filter $G_{NF}(s)$ to eliminate the $2\omega_o$ component while maintaining rapid dynamic performance.
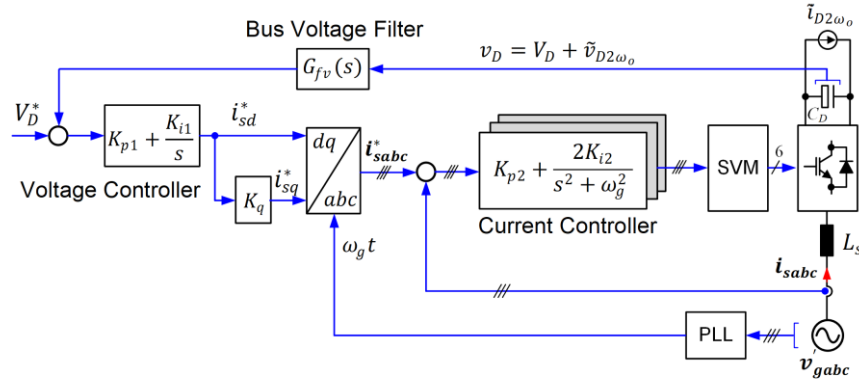
Figure 22 Equivalent SEIG-side power converter control system in the natural reference frame.

3.2.2 Grid-Side Power Conversion Topologies

The proposed topology's output stage, as depicted in Figure 23, consists of the single-phase *LCL*-filtered grid-connected inverter. The inclusion of the damping resistor R_f within the *LCL* filter ensures control stability, especially in the presence of significant grid impedance. This study employs feedback control of the grid current $i_o(t)$. The grid voltage $v_o(t)$ can be expressed as:

$$v_o(t) = \hat{V}_o \cos\omega_o t \tag{27}$$

where $\hat{V}_o$ is the voltage amplitude, $\omega_o = 2\pi f_o$ is the grid frequency. The desired grid current $i_o(t)$ is

$$i_o(t) = \hat{I}_o \cos(\omega_o t + \varphi_o) \tag{28}$$

The single-phase inverter is controlled in the virtual synchronous reference frame control by setting $i_{o\alpha}(t) = i_o(t)$ and the orthogonal current $i_{o\beta}(t) = i_o(t)e^{-\frac{j\pi}{2}} = \hat{I}_1 \sin(\omega_o t + \varphi_o)$. The grid current is decoupled into the dq axes using the Park transformation given by

$$\begin{bmatrix} i_{od}(t) \\ i_{oq}(t) \end{bmatrix} = \begin{bmatrix} \cos\omega_o t & \sin\omega_o t \\ \sin\omega_o t & \cos\omega_o t \end{bmatrix} \cdot \begin{bmatrix} i_o(t) \\ i_{o\beta}(t) \end{bmatrix} = \begin{bmatrix} \hat{I}_o \cos\varphi_o \\ \hat{I}_o \sin\varphi_o \end{bmatrix} \tag{29}$$

The synchronous reference frame control leads to the decomposition of the instantaneous power and reactive power as follows [54]:

$$p_o(t) = \frac{\hat{V}_o(t)}{2} \hat{I}_o \cos\varphi_o = \frac{\hat{V}_o}{2} i_{od}(t) \tag{30}$$

$$q_o(t) = -\frac{\hat{V}_o(t)}{2} \hat{I}_o \sin\varphi_o = -\frac{\hat{V}_o}{2} i_{oq}(t) \tag{31}$$

The grid-side control system is implemented in the unbalanced synchronous reference frame, a subclass of the synchronous reference frame control. Figure 23 illustrates the stationary reference frame representation of the synchronous reference frame control. The error signals $e_\alpha(t)$ and $e_\beta(t)$ in the $\alpha\beta$ −axes are transformed into the error signals $e_d(t)$ and $e_q(t)$ in the dq −axes with the angle $h\omega_o t$. The controllers $H_{DC}(s)$ in the dq −axes generate the control signals $y_d(t)$ and $y_q(t)$, which are then transformed back to the $\alpha\beta$ −axes control signals $y_\alpha(t)$ and $y_\beta(t)$. Utilizing the convolution and modulation properties of the Laplace transformation [38], the stationary reference frame outputs can be expressed as:

$$\begin{bmatrix} y_\alpha(s) \\ y_\beta(s) \end{bmatrix} = \frac{1}{2} \begin{bmatrix} \begin{pmatrix} H_{DC}(s+jh\omega_o) \\ +H_{DC}(s-jh\omega_o) \end{pmatrix} & \begin{pmatrix} -jH_{DC}(s+jh\omega_o) \\ +jH_{DC}(s-jh\omega_o) \end{pmatrix} \\ \begin{pmatrix} jH_{DC}(s+jh\omega_o) \\ -jH_{DC}(s-jh\omega_o) \end{pmatrix} & \begin{pmatrix} H_{DC}(s+jh\omega_o) \\ +H_{DC}(s-jh\omega_o) \end{pmatrix} \end{bmatrix} \begin{bmatrix} e_\alpha(s) \\ e_\beta(s) \end{bmatrix} \tag{32}$$

If the β-axis input $x_\beta(t) = 0$ and only the output in the α-axis is considered for the single-phase system, the stationary reference frame equivalence of $H_{DC}(s)$ becomes

$$H_{AC}(s) = \frac{y_\alpha(s)}{e(s)} = \frac{1}{2}\left(H_{DC}(s+jh\omega_o) + H_{DC}(s-jh\omega_o)\right) \tag{33}$$

If $H_{DC}(s) = K_P + \frac{K_I}{s}$ is the standard PI controller, $H_{AC}(s)$ is

$$H_{AC}(s) = K_P + \frac{K_I}{s^2+(h\omega_o)^2} \tag{34}$$

The equivalent controller transfer function in the stationary reference frame in Equation (34) is identical to the ideal proportional-resonant controller, which offers an infinite gain at the target frequency $h\omega_o$, ensuring zero steady-state error. This control technique is known as the unbalanced synchronous reference frame control, which has demonstrated successful applications for single-phase converters [39, 40]. The unbalanced synchronous reference frame control can be implemented in various structures with equivalent performance [57].
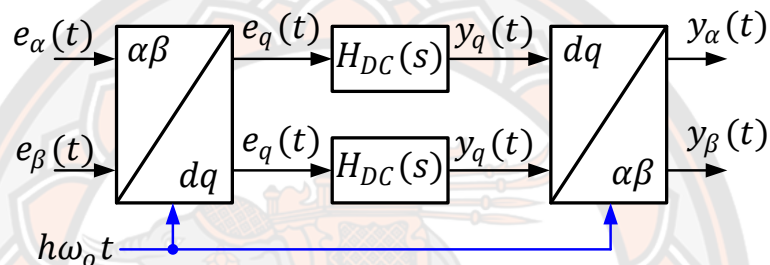
Figure 23 Stationary reference frame representation of the synchronous reference frame control.

Figure 24(a) illustrates the grid-side control system of the single-phase inverter, which is realized in the multiple unbalanced synchronous reference frame on the same microcontroller as the SEIG-side control. The proposed control scheme comprises a fundamental component controller at the grid frequency ω_o, along with multiple harmonic controllers at frequencies $h\omega_o$. These harmonic controllers mitigate low-frequency harmonics in the grid and inverter output voltages arising from switching dead times [54]. An inverse Park transformation Phase-Locked Loop (PLL) estimates the angle $\theta_o = \omega_o t$ and the grid voltage amplitude $\hat{V}_o$ [58].

A low-pass filter with a time constant of T_{fo} is employed to attenuate the rapid changes in the power reference P_o^*, ensuring smooth extraction of power from the SEIG and engine. The $d-$axis reference current $i_{od}^*(t)$ is computed from the filtered reference output power P_{of}^* using Equation (12), while the $q-$axis reference current $i_{oq}^* = 0$ is set for unity power factor operation. The fundamental current controller utilizes the grid current as the $\alpha-$axis component current $i_{o\alpha}(t) = i_o(t)$ and the reference current $i_{o\beta}^*$ as the $\beta-$axis component current $i_{o\beta} = i_{o\beta}^*$ for the reference frame transformation [47].

The fundamental grid current components $i_{od}(t)$ and $i_{oq}(t)$ in the $dq-$axes are regulated by the PI controllers $G_{PIO}(s) = K_{PO} + \frac{K_{Io1}}{s}$, whose outputs m_{d1}^* and m_{q1}^* are transformed back to the stationary reference frame. The $\alpha-$axis output $m_{\alpha1}^*$ is only used. This control structure has inherent power decoupling and frequency adaption capabilities [54].

Figure 24(b) illustrates the details of the harmonic current controllers implemented in the modulation/demodulation structure at frequencies $h\omega_o$. These controllers possess a simpler structure compared to the fundamental component controller while maintaining identical performance. The $\alpha-$axis reference current $i_{o\alpha}^*$ is compared with the grid current $i_o(t)$. The resulting error signals in the $dq-$axes are regulated by the integral controllers $\frac{K_{Ioh}}{s}$, the outputs of which are transformed back to the $\alpha-$axis signals m_h^*. The output signals of the fundamental current controller $m_{\alpha1}^*$ and the harmonic controller m_h^* constitute the input signal m^* for the Pulse Width Modulation (PWM) unit embedded in the microcontroller. The transfer function of the grid current controller is equivalent to a Proportional-Multi-Resonant (PMR) controller as described in [54].

$$G_{io}(s) = \frac{m^*(s)}{i_o^*(s) - i_o(s)} = K_{PO} + \sum_{h=1}^{n} \frac{K_{Ioh}}{s^2 + (h\omega_o)^2} \qquad (35)$$
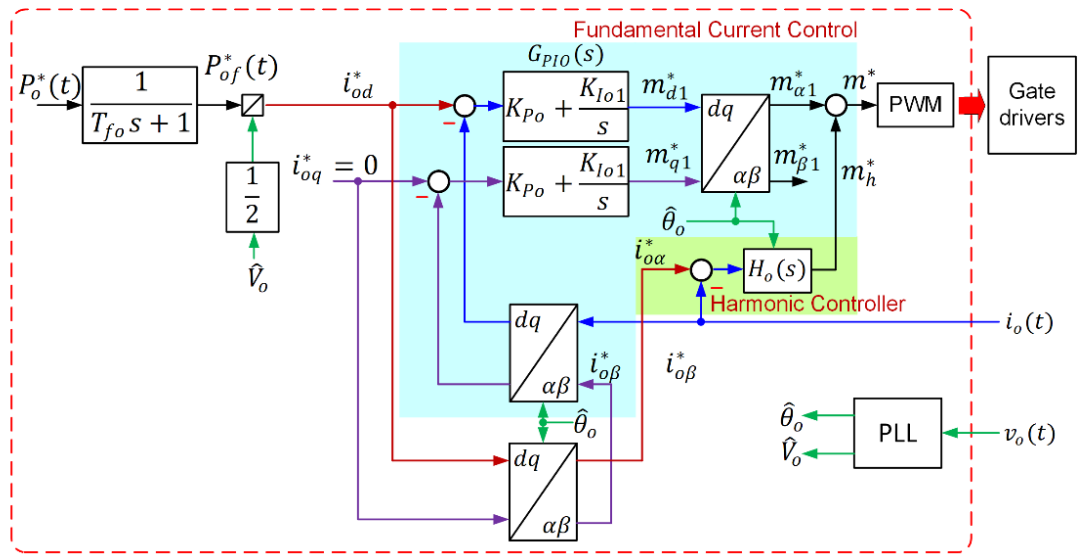
(a)
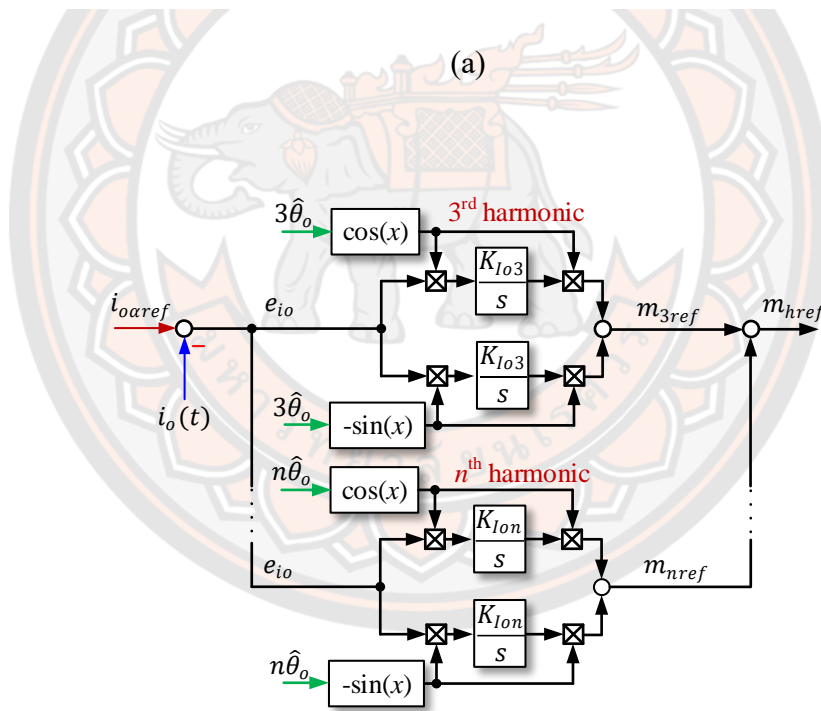
(b)

Figure 24 Grid-side control system: (a) Overall control system, (b) Structure of the harmonic control.

3.3 Prototype Construction

    3.3.1. Back-to-back converter design

        The proposed power converter depicted in Figure 5 was assembled using parameters listed in Table I. The excitation capacitors C_{ex} were utilized to raise the SEIG voltage to the nominal value of V_{LL} =220 V (line to line) at the no-load rotational speed of approximately 3,000 rpm. Assuming an efficiency of 70% for both the converter and SEIG, the nominal output power was set at 1.5 kW, resulting in a mechanical input power of $P_m = 2.14$ kW, which closely aligns with the rated power. Both the SEIG-side and grid-side converters employed the asymmetrical regular sampled Pulse Width Modulation (PWM) technique with a triangular carrier frequency of f_c =10 kHz and a sampling frequency of f_s =20 kHz. The resonant frequency f_{LCL} is determined by:

$$f_{LCL} = \frac{1}{2\pi \sqrt{\left(\frac{L_1 L_2}{L_1 + L_2}\right) C_f}} \tag{36}$$

        According to Table I, $f_{LCL} = 5.06$ kHz satisfies the stability criterion given by [59]

$$\frac{f_s}{6} < f_{LCL} < \frac{f_s}{2} \tag{37}$$

        The grid current control loop with harmonic controller orders 3rd, 5th, 7th, and 9th was designed to operate at a bandwidth of 1,100 Hz [54]. The current control loop of the PWM rectifier was tuned to an approximate bandwidth of 1,000 Hz using the method outlined in [60]. Figure 25 illustrates the simplified control block diagram of the bus voltage control loop, where the notch filter is approximated as a low-pass filter. The controller parameters K_{p1} and K_{i1}, along with the notch filter's damping factor ξ, were determined using the extended symmetrical optimum method [61] at a loop bandwidth of 15 Hz.
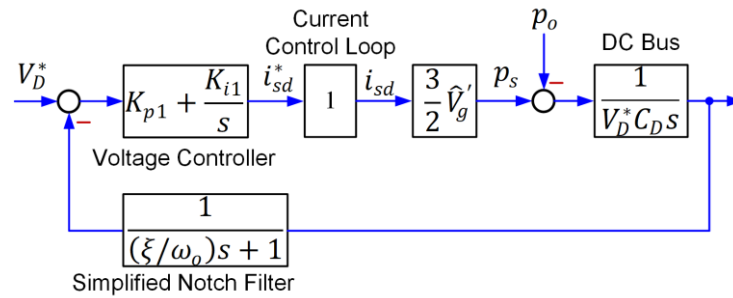
Figure 25 Simplified bus voltage control block diagram.

3.3.2. Experimental setup

Figure 26 displays the prototype of the biogas power generation system installed at Tha Manoa Subdistrict, Chaibadal District, Lopburi, Thailand (15.1998°N, 101.1652°E). Figure 11 illustrates the performance evaluation diagram of the prototype system. Gasohol, consisting of 90% 95-octane gasoline and 10% ethanol by volume, was utilized for laboratory tests. The average thermal input power was determined from the consumption rate monitored in 10-minute intervals using a digital weighing scale. During field tests at Tha Manoa Subdistrict, the engine was fueled by biogas. In this community, there are 8 pig farms, each containing 100-700 pigs. Each farm has installed an anaerobic covered lagoon for biogas production from pig slurry. The produced biogas from each lagoon is purified by passing through $Fe(OH)_3$ absorbent granules, which were made from grey cement mixed with fine sand soaked in $FeCl_3$ and $NaOH$ [62]. Fan blowers pressurize the upgraded biogas for distribution to 230 households for cooking purposes between 5.00 – 9.00 am and 4.00 – 9.00 pm daily. Excess biogas is planned for power generation. The thermal input power was determined from the volumetric flow rate using a thermal mass flowmeter and CH_4 content monitored by a gas analyzer. The shaft torque, speed, and mechanical power were obtained from a torque-speed sensor mounted between the engine and the SEIG. Electrical parameters at the SEIG and converter outputs were measured by a 4–channel power analyzer, while current and voltage waveforms were recorded by a 4–channel digital oscilloscope.

Table 5 This is a table. Tables should be placed in the main text near to the first time they are cited.

Symbol	Quantity	Value
P_o	Nominal output power	1.5 kW
V_{LLB}	Nominal SEIG line-to-line voltage	220 V
f_{gB}	Nominal SEIG frequency	50 Hz
C_{ex}	Excitation capacitors	40 µF (Δ connection)
V_D	Nominal DC voltage	400 V
V_o	Nominal grid voltage	220 V
f_o	Grid frequency	50 Hz
f_c	Triangular carrier frequency	10 kHz
f_s	Sampling frequency	20 kHz
L_s	SEIG-side inductor	2 mH
C_D	DC bus capacitor	1,000 µF
L_1	LCL filter inductor	1 mH
L_2	Grid-side inductor	0.5 mH
C_f	LCL filter capacitor	3 µF
R_f	LCL filter damping resistor	1 Ω

Figure 26 Prototype of the biogas power generation system.

The thermal input power was determined from the volumetric flow rate using an Omega FMA-A2100 thermal mass flowmeter (Stamford, CT, USA), while the CH4 content was monitored by an IRCD4 gas analyzer from Beijing Shi'An Technology (Beijing, China). The shaft torque, speed, and mechanical power were obtained from a CALT DYN-200 torque-speed sensor (Shanghai, China) mounted between the engine and the SEIG. Electrical parameters at the SEIG and converter outputs were measured by a Yokogawa WT300 4-channel power analyzer (Tokyo, Japan). Current and voltage waveforms were recorded by an ISO-TECH IDS-1074B 4-channel digital oscilloscope (Corby, UK).
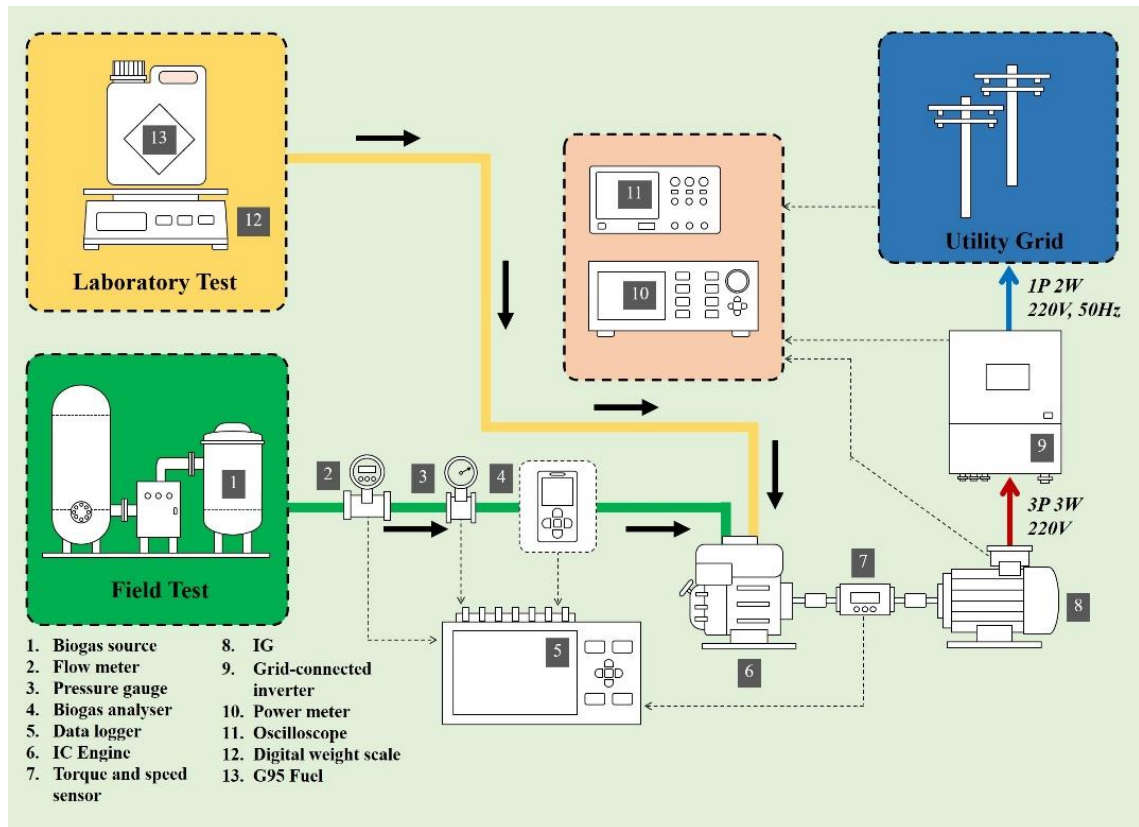
Figure 27 Performance evaluation diagram of the biogas power generation system.

CHAPTER IV

THE POWER MONITORING SYSTEM BASED ON INTERNET

OF THINGS

4.1 Internet of Things

Currently, the Internet of Things (IoT) is being utilized in various activities, particularly in the application of energy management systems using smart grid technology. These smart grids are designed to monitor and measure electricity consumption and collect data to forecast electricity demand at different times. The collected data is invaluable for several aspects of energy management, including controlling the distribution of electricity, planning the construction of power plants, managing energy supply sources, and setting electricity prices in alignment with demand and supply principles [65-66].

The integration of IoT in smart grids facilitates real-time monitoring and data acquisition, which enhances the efficiency and reliability of the electrical grid. By accurately forecasting demand, utility companies can optimize their operations, reduce wastage, and ensure a stable supply of electricity. This predictive capability is crucial for balancing load and preventing blackouts, thereby improving the overall resilience of the energy infrastructure [65-66].

The concept of IoT-based smart management is not limited to electricity. Similar methodologies can be applied to other utility management systems, such as smart water systems and smart irrigation systems. In smart water systems, IoT devices can monitor water usage, detect leaks, and ensure efficient water distribution. Smart irrigation systems can optimize water use in agriculture by monitoring soil moisture levels and weather conditions, thereby promoting sustainable water use and enhancing crop yield [65-66].

These IoT applications in utility management exemplify how technology can drive efficiency and sustainability across various sectors. By leveraging IoT for real-time data collection and analysis, we can achieve more informed decision-making, resource optimization, and ultimately, a more sustainable interaction with our environment [65-66].

4.2 MIT App Inventor Application

The MIT App Inventor is a smartphone application that operates on the Android operating system. It can be accessed through a web browser and tested on a connected smartphone or a phone emulator on a computer. The application development process is divided into two main parts. The first part is the design phase, using the App Inventor Designer, which allows users to select the components needed to create the application. The second part is the coding phase, utilizing the App Inventor Blocks Editor. This phase involves programming the application, after which the application package can be deployed on Android smartphones. This division facilitates a streamlined and user-friendly approach to app development, making it accessible to a broad range of users, from beginners to more experienced developers [65, 66, 67].
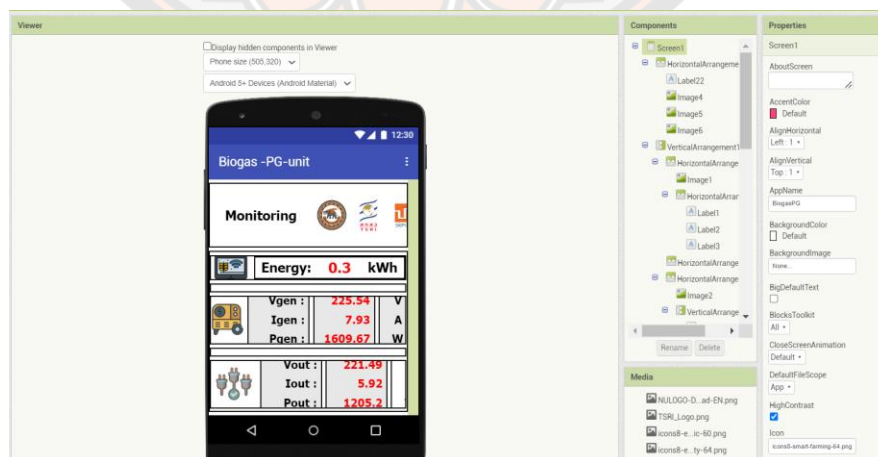
Figure 28 Example of Creating a Dashboard Interface with App Inventor Designer

4.3 Design of an Energy Monitoring System on a Smartphone Application

The design of an electrical power display system based on a smartphone application can be schematically shown in Figure 29(a). This research uses the EasyLogic PM2230 power meter manufactured by Schneider Electric, which is used for industrial applications. Modbus protocol connection is supported by specifying the register location of the required parameters from the manufacturer's instruction manual. The data from the power meter is sent to the NodeMCU ESP32 via RS485 Modbus Protocol and converted to TTL (Transistor-Transistor Logic). It is forwarded via Wi-Fi to Google Firebase [68, 69] as a real-time database for displaying windows on applications by application design with MIT app inventor software was developed on the MIT platform using Component Oriented Software (Component-based Software Development) principles without writing commands (Source code) developed applications [67]. The real-time data collection system that is designed can be seen in Figure 29(b). We choose to use data collection on Google Sheets in real-time every 10 minutes. Create JavaScript code to retrieve values sent from the NodeMCU ESP32 and store them in Google Sheets with the Google Apps Script function.
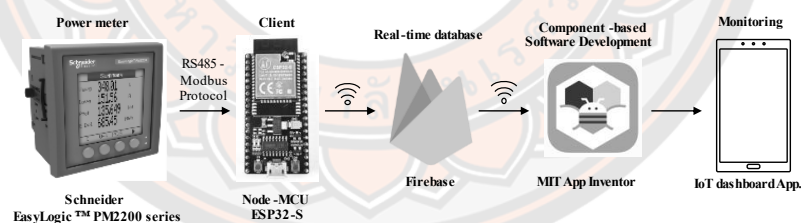
(a)
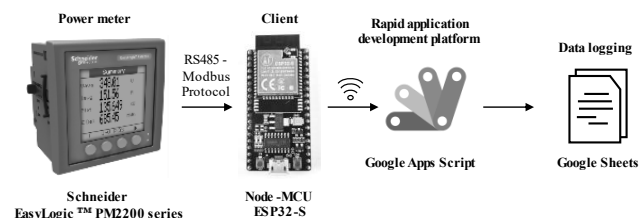
(b)

Figure 29 Power Monitoring System based IoT: a) Power monitoring system on an application, and b) Realtime data logging.

The application is developed using component-based software development principles, eliminating the need to write source code manually [67]. This approach allows for the application to be installed on Android smartphones via a QR code. An example of the developed application is shown in Figure 30.
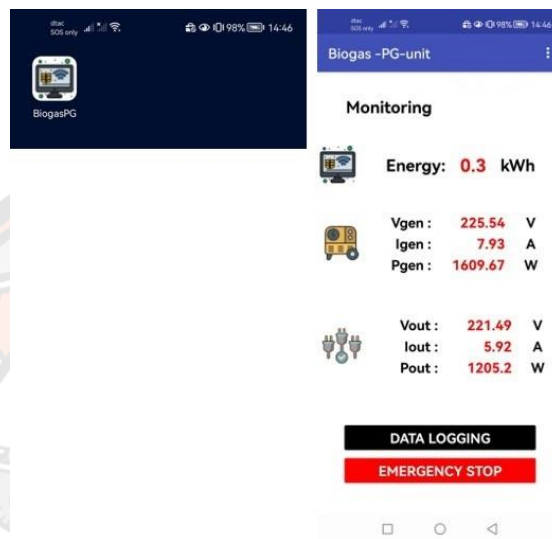
Figure 30 Power monitoring on smartphone applications

CHAPTER V

RESULT AND DISCUSSION

4.1 Control performance of the SEIG and back-to-back converter

This segment aims to confirm the laboratory functionality of the SEIG and back-to-back converter setup. The SEIG was powered by the GX200T2 QHT engine using gasohol. Through experimental analysis, the reactive power gain K_q was established at 0.5 to maintain a consistent ratio between the SEIG voltage and frequency across its operational spectrum.

Figure 31(a) illustrates the SEIG voltage buildup process. Initially, a small SEIG voltage $v_{gab}(t)$ emerges, attributed to the residual flux density within the rotor core. Upon connection with the back-to-back converter, $v_{gab}(t)$ gradually escalates due to the reactive power $q_1(t)$ provided by capacitors C_{ex}. Concurrently, as the terminal voltage is established, the SEIG also delivers active power to the DC bus capacitor C_D, while the Voltage Source Converter (VSC) functions as a passive rectifier. Consequently, the DC bus voltage approximates the peak value of the SEIG line-to-line voltage.

During the build-up period, the VSC current $i_{sa}(t)$ progressively rises and eventually decreases to zero at steady state. Under the steady-state no-load condition, the SEIG current $i_{ga}(t)$ flows between the SEIG and C_{ex}, indicated by $i_{sa}(t) \approx 0$. At this point, the voltage $v_{gab}(t)$ stabilizes at the RMS value of $V_{LL} \approx 220$ V. It is important to note that this voltage V_{LL} is contingent on the value of C_{ex} and the engine speed ω_m.

Figure 31(b) illustrates the PWM rectifier startup when $v_D(t)$ increases to the reference $V_D^* = 400$ V. During this transient condition, $v_{gab}(t)$ drops because the SEIG supplies active power $p_g(t)$ to the bus capacitance. Nonetheless, the SEIG remains excited due to the reactive power $q_2(t)$ fed back from the PWM rectifier to the SEIG.
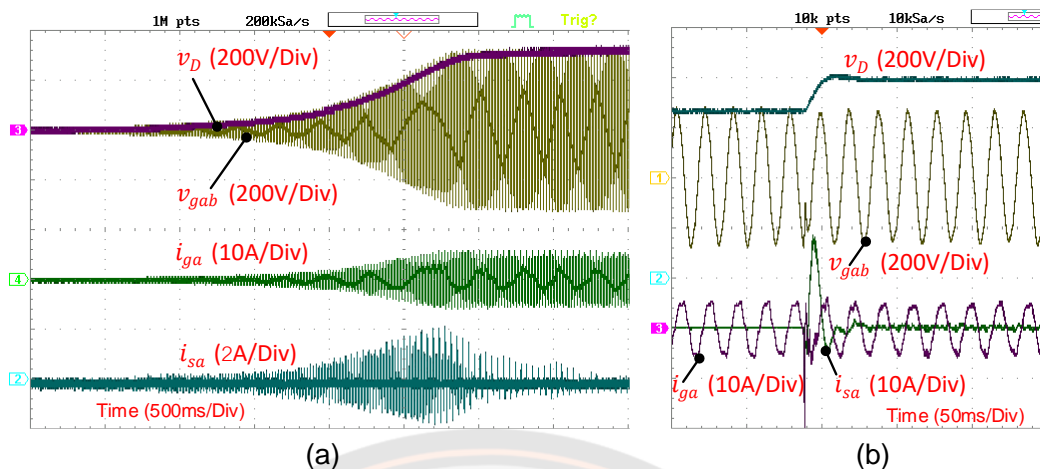
Figure 31 Transient voltage and current waveforms of the SEIG-side converter: (a) Voltage build-up period, (b) DC bus voltage start-up period.

After initializing the PWM rectifier, the grid-side inverter was activated. In Figure 32, the transient response of the grid current $i_o(t)$ is depicted when injecting a power output of 1,200 W. The dq – axes current signals $i_{sd}(t)$ and $i_{sq}(t)$ of the PWM rectifier in the microcontroller-based control system were transmitted to 14-bit digital-to-analog converters (DACs) for observation on an oscilloscope. In the SEIG-side control system, the d –axis current $i_{sd}(t)$ is generated to extract an active power $p_g(t)$ from the SEIG. Correspondingly, the q –axis current $i_{sq}(t)$ increases in tandem with $i_{sd}(t)$.

Figure 33 depicts the steady-state waveforms of the grid voltage $v_o(t)$ and current $i_o(t)$, alongside the SEIG voltage $v_{gab}(t)$ and current $i_{ga}(t)$ at a rated output power of 1.5 kW, with the engine speed approximately at 2,900 rpm. The SEIG frequency is measured at 46 Hz. Notably, the SEIG current waveform closely resembles a sinusoid without interharmonic components, as elucidated in (8), owing to the presence of a notch filter that blocks the $2\omega_o$ component of the bus voltage. Simultaneously, the grid current waveform exhibits sinusoidal characteristics, courtesy of the additional harmonic controller. The impact of bus voltage ripple on the SEIG current is delineated in Figure 34, where the notch filter is substituted with a low-pass filter. The bus voltage loop bandwidth was adjusted to 15 Hz, akin to the notch filter-based control. The alterations in each SEIG current cycle indicate the presence of inter-harmonic components, as expounded in (8).
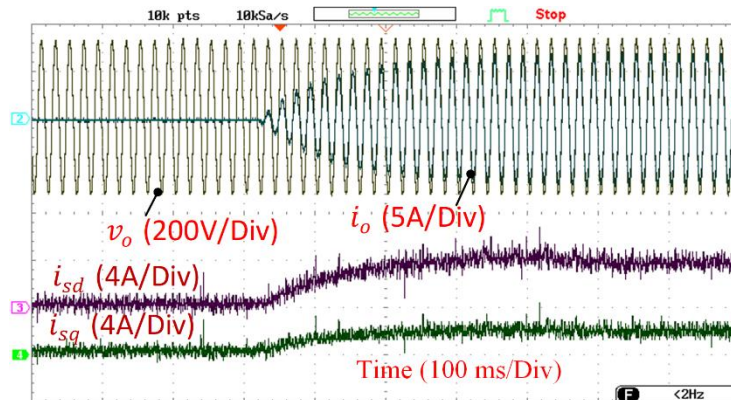
Figure 32 Transient response when injecting a power of 1,200 W to the grid.
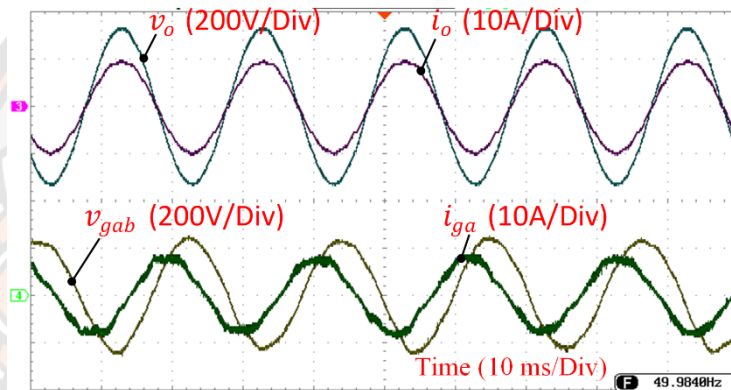
Figure 33 Steady state waveforms of the grid voltage and current and SEIG voltage and current at the rated output power of 1.5 kW with the notch filter-based bus voltage control.
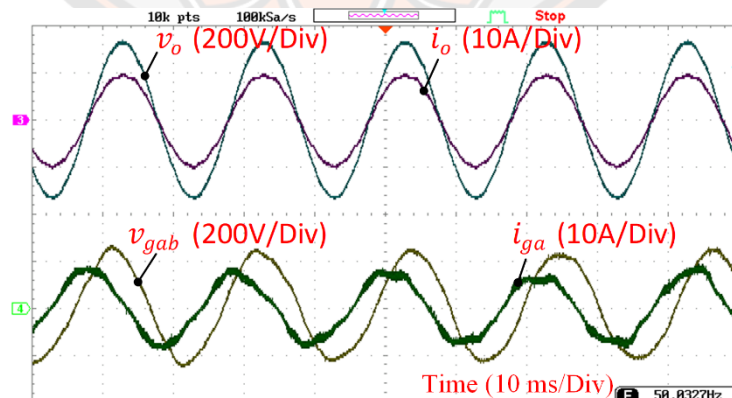
Figure 34 Steady state waveforms of the grid voltage and current and SEIG voltage and current at the rated output power of 1.5 kW with the low pass filter-based bus voltage control.

Moreover, the SEIG current waveform exhibits sinusoidal characteristics with a total harmonic distortion (THD) of 2.67% at the rated power. Figure 35 illustrates the grid current harmonics at output powers of 500 W (33%), 1,000 W (66%), and 1,500 W (100%), normalized by the rated current of 6.75 A. These harmonics adhere to the requirements stipulated in the IEEE 1547 standard [64].
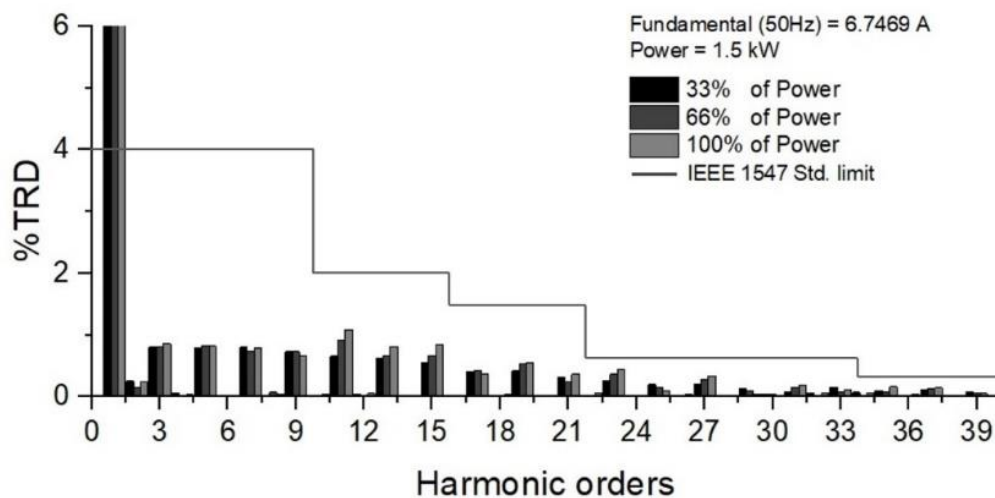
Figure 35 Output current harmonics of the grid-side inverter normalized by the rated current according to the IEEE 1574 standard.

Figure 36 displays the reactive power $q_2(t)$ injected by the PWM rectifier into the SEIG across the output power range from 10% to 100%. The reactive power from the capacitor bank Q_1 is calculated from:

$$Q_1 = 3 \times (V_{LL}^2 \omega_g C_{ex}) \tag{38}$$

The reactive power Q_1 diminishes with the output power owing to the reduction in generator frequency. Meanwhile, the reactive power $q_2(t)$ from the PWM rectifier assumes a crucial role in regulating the SEIG voltage. Figure 37 illustrates the SEIG voltage/frequency ratio normalized by the nominal value of V_{LLB}/f_{gB}, which closely approaches unity across the output power range.
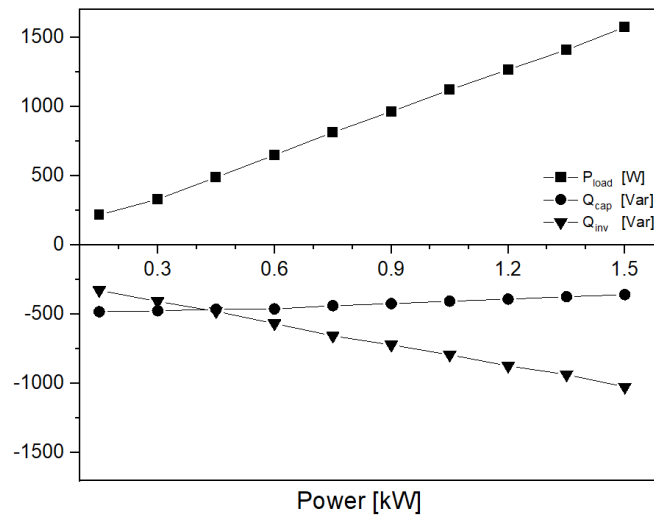
Figure 36 Reactive power and active power of the SEIG with the output power.
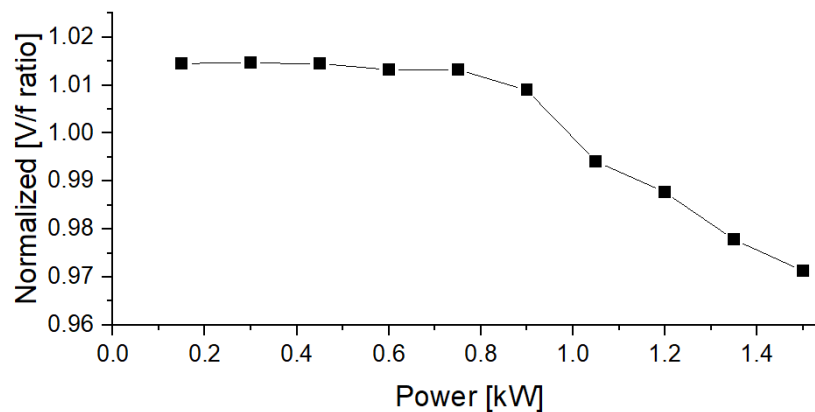
Figure 37 Normalized SEIG voltage/frequency ratio.

The mechanical frequency ω_m of the induction machine is lower than the electrical frequency ω_g when operating in the motor mode, and higher than ω_g for the generator mode. The slip S resulting from the speed difference is expressed as:

$$S = (\omega_g - \omega_m)/\omega_g \tag{39}$$

Figure 38 presents a comparison between ω_m and ω_g, normalized by the nominal frequency $\omega_{gB} = 2\pi f_{gB}$ plotted against the shaft torque T_m. As the torque T_m increases, the mechanical frequency ω_m decreases, consistent with the engine characteristic. The SEIG-side converter draws active power $p_g(t)$ from the SEIG,

causing the SEIG frequency ω_g to lag behind the mechanical frequency ω_m. Consequently, in the generator mode, the slip S diminishes with increasing torque in the negative region.
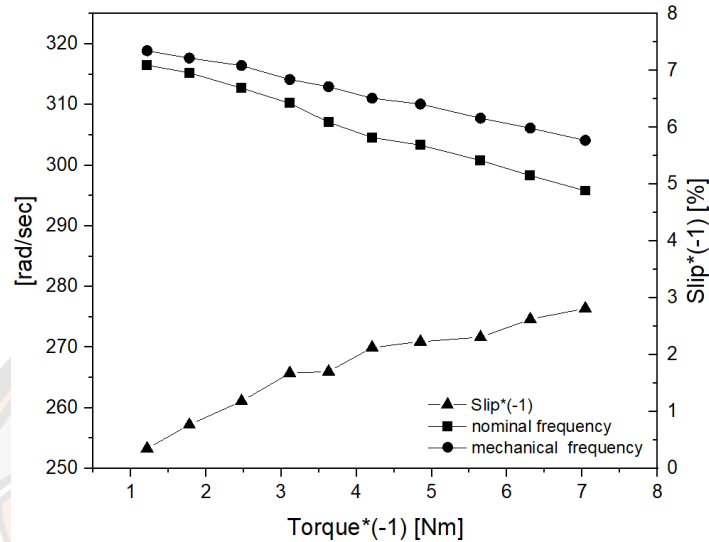
Figure 38 Mechanical, SEIG frequency and slip versus the shaft torque.

4.2 System Efficiency

The prototype's efficiency was validated using biogas at the designated area, Ta Manoa Subdistrict, in December 2021. A Beijing Shi'An Technology IRCD4 gas analyzer monitored the composition of biogas during the experiment, with details listed in Table II. Engine exhaust gas was monitored using an SA500 gas analyzer from the same manufacturer. During the field experiments, the no-load speed was set at approximately 3,250 rpm. This adjustment was necessary because the shaft speed with biogas decreased more significantly with higher output power compared to gasohol in laboratory tests. Consequently, excitation capacitors of $C_{ex} = 35$ µF were utilized in the field experiment to accommodate the higher no-load speed.

In the field tests with biogas, the prototype system delivered a maximum output power of 1,200 W, which was 80% of the rated value. This reduction in output power was attributed to low biogas production. Unfortunately, the pigs were young during the test period, resulting in insufficient manure to produce biogas at full scale.

Table 6 Biogas composition in the field experiments

Composition	Content
CH_4	68.5 - 70.0%
CO_2	30%
H_2S	0.14 - 0.24%

Figure 39 illustrates the comparison of the engine shaft speed fueled by gasohol and biogas. It is evident that the engine speed with biogas drops rapidly when the output power exceeds 70% of the rated power. Moreover, during the field experiments, it was observed that the engine experienced knocking when the output power exceeded 80% of the rated value. In contrast, the engine fueled by gasohol delivers power smoothly.

However, the prototype's output power was derated due to the unstable biogas supply during the experiment and the lower energy density of biogas itself. Figure 40 presents the biogas consumption at 21°C and 101.325 kPa, obtained from the thermal mass flowmeter, against the output power. This biogas flowrate, along with the methane content detailed in Table II, was utilized to calculate the engine input power.
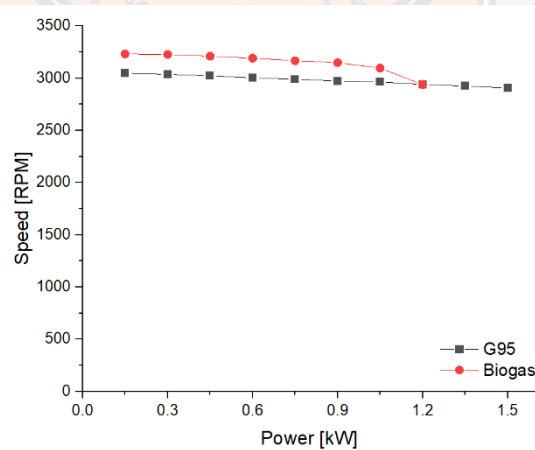
Figure 39 Engine shaft speed with the output power.
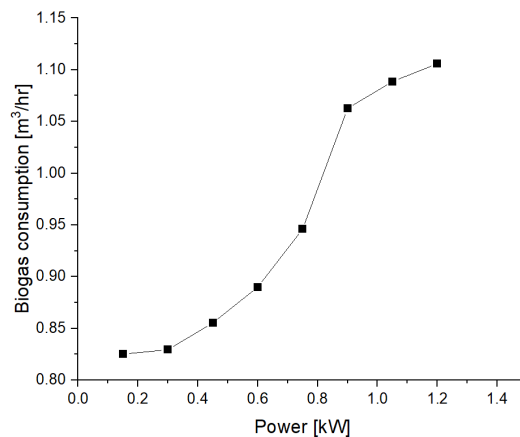
Figure 40 Biogas consumption with the output power.

Figure 41 provides a comparison of the engine's efficiency, SEIG, back-to-back converter, and the overall system performance using biogas and gasohol. The engine's efficiency significantly influences the overall system efficiency. Notably, the engine efficiency with biogas is lower than that with gasohol. For instance, at an output power of 80%, the engine efficiency is approximately 14% with biogas, compared to 18% with gasohol. However, it is important to note that the engine efficiency could potentially be enhanced if the biogas supply could support higher power operations.

On the other hand, the SEIG and back-to-back converter exhibit efficiencies greater than 70% and 90%, respectively, for output powers exceeding 50%. Despite this, the system efficiency with biogas is approximately 10.7% at an output power of 80%. However, it is anticipated that the system efficiency with biogas could reach about 13% at the rated power, based on the system efficiency achieved with gasohol.

Figure 42 presents a comparison of NOx and CO emissions from the exhaust gas. Remarkably, the NOx emission from the biogas-fueled system is significantly lower than that from the gasohol-fueled system. Specifically, the NOx emission from the biogas-fed system remains below 50 ppm at 80% output power, owing to the purification process employing $Fe(OH)_3$ absorbent granules.

Furthermore, the CO emission from the biogas-fed engine decreases with increasing output power, with levels below 400 ppm at 80% output power. This reduction is attributed to a more complete combustion process. In contrast, the CO emission from the gasohol-fueled system remains consistently high, at 2,000 ppm, for all output power levels. Notably, this value represents the maximum measurable limit of the exhaust gas analyzer, indicating that the actual CO emission was higher than 2,000 ppm.

(a)

(b)

(b)

(d)
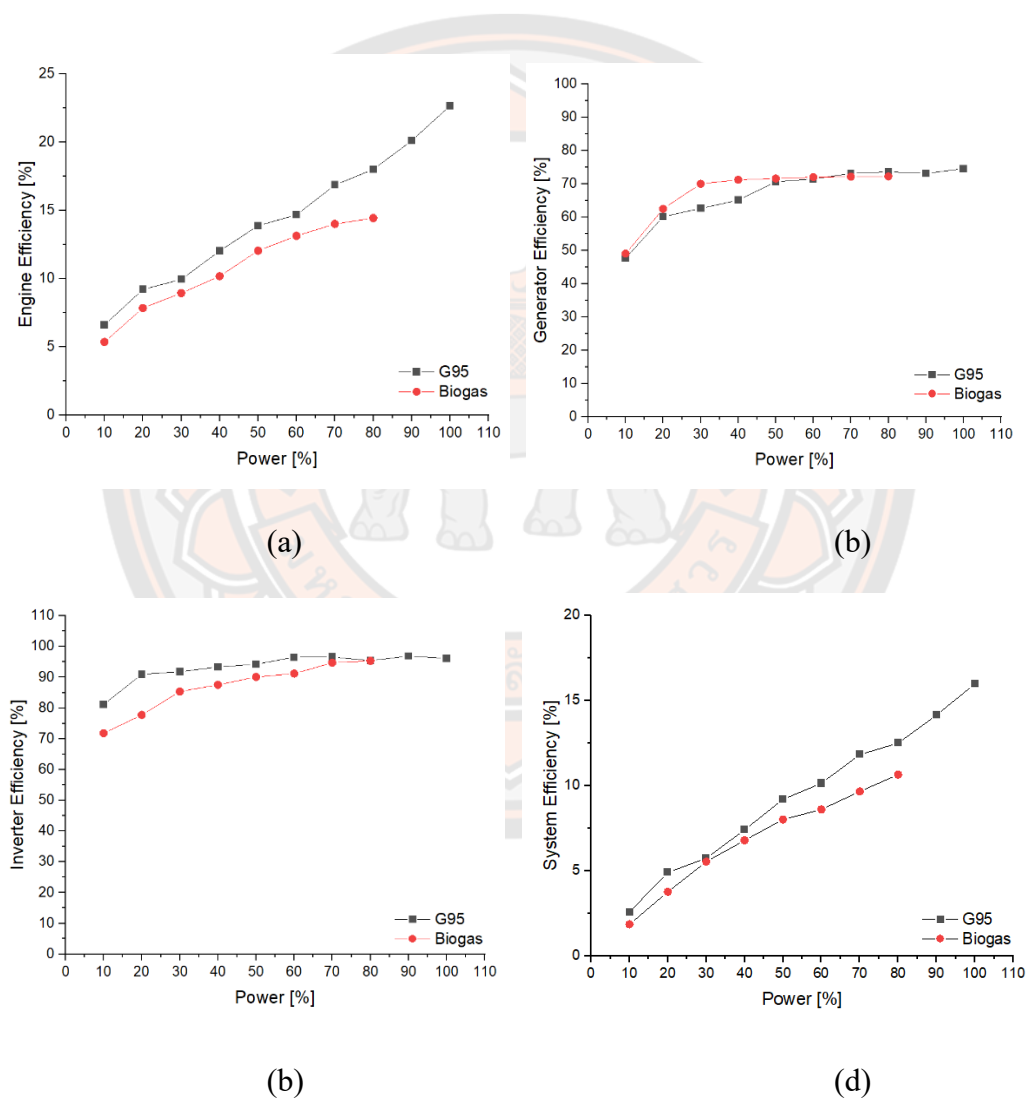
Figure 41 Efficiency of the prototype generation system: (a) engine, (b) SEIG, (c) back-to-back converter, and (d) system.
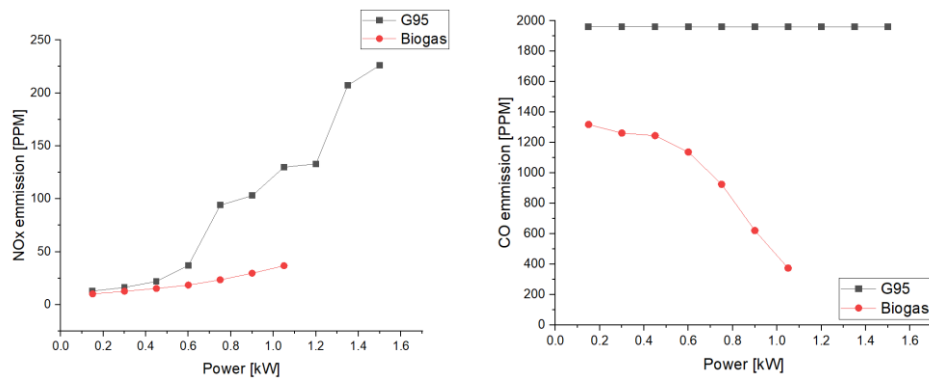
Figure 42 NO$_x$ and CO emissions with the output power.

4.4 Power Monitoring System Testing

In this test uses two power meters, one measuring 3-phase, 3-wire delta ungrounded on the generator side and the second measuring 1-phase, 2-wire delta on the grid side. (Single-phase 2-wire L-N) can be shown in Figure 43 and compare the efficiency of the data recorded from this research data recording system with the data recorded from the standard measuring equipment. Here, a power meter, model Chroma digital power meter 66204, is installed on the grid side to measure and record data every 5 minute for comparison by setting the following parameters: Vs, Is, and Fs. The comparison uses the square root of the mean square error (Root Mean Square. Error: RMSE) to show the evaluation of the error from the proposed data collection system. The comparison results are shown in Figure 44.
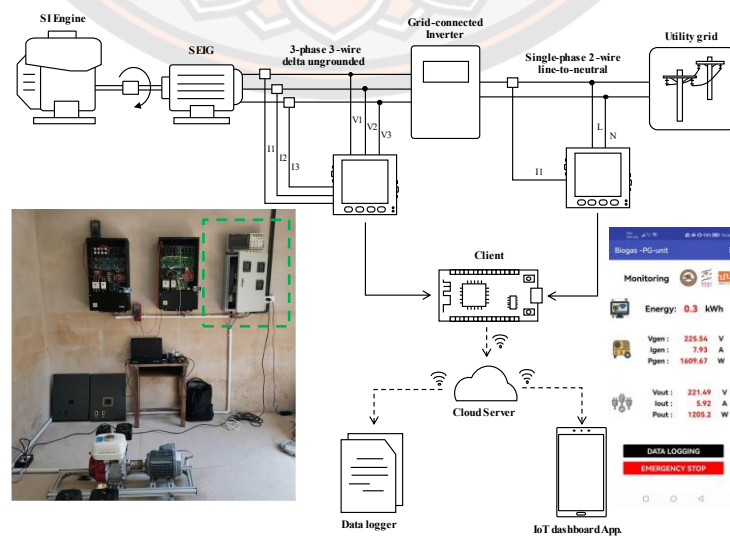
Figure 43 Testing Setup of a Power Monitoring System-Based IoT
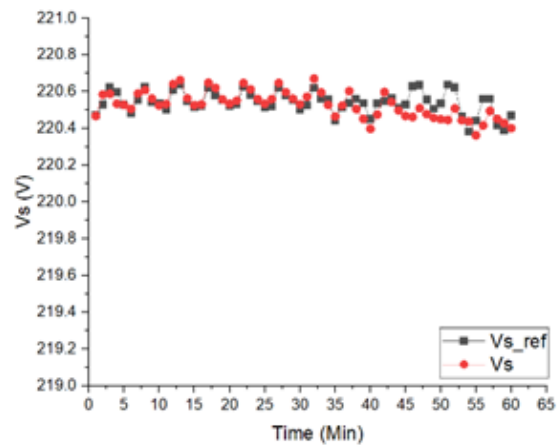
(a) Grid voltage
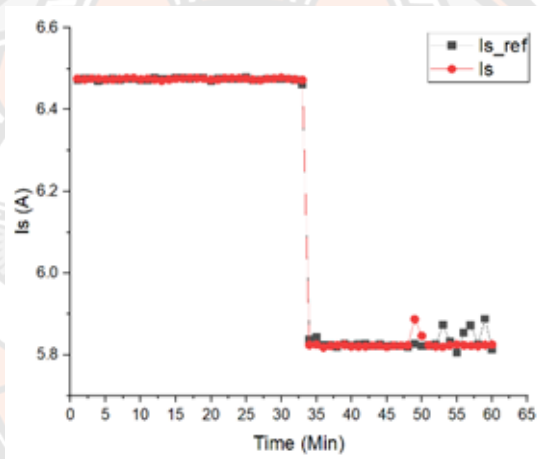
(b) Grid Current
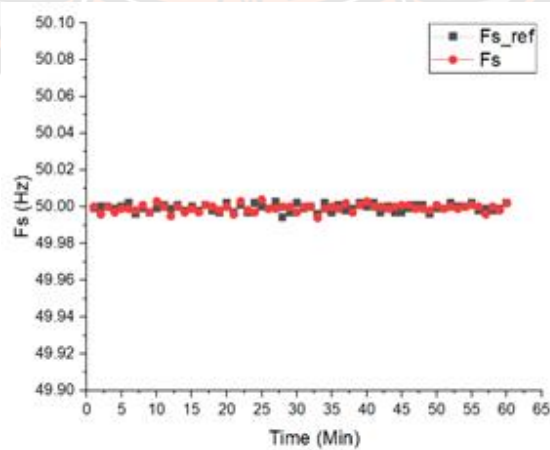
(c) Grid frequency

Figure 44 The error values from the proposed data acquisition system using RMSE

From Figure 44, it was found that the parameter data measured by the measuring instrument compared to the display system and the data collected in real-time were similar. When estimating the error values from the proposed data acquisition system using RMSE, it was found that the recorded grid voltage Vs, grid current Is and grid frequency Fs tested had tolerances of 0.05888, 0.12547, and 0.00244 respectively, which are in the range is acceptable and very close to standard measuring tools.

4.3 Suitability and Economic Analysis

The technically proven biogas generation system presents various potential applications and economic feasibility considerations, which are essential for its successful implementation and commercialization. Below are some key points to consider in the analysis:

4.31. Suitability of the proposed biogas power generation system

Based on the given operational scenario and biogas consumption rate, the prototype system requires approximately 8.85 m³ of biogas daily to sustain a power production level of 1.2 kW for 8 hours each day. Furthermore, considering the biogas production rate from pig manure reported in [8], where a mature pig excretes manure of 2 kg/day, yielding biogas production of 0.26 m³, we can calculate the number of pigs required to meet the biogas demand.

Given that each pig produces 0.26 m³ of biogas per day, and the system requires 8.85 m³ daily, the minimum number of pigs required can be calculated as:

$$Number\ of\ pigs = \frac{Biogas\ demand}{Biogas\ production\ per\ pig\ per\ day}$$

$$= \frac{8.85\ m^3}{0.26\ \dfrac{m^3}{pig}}{day}} \approx 34\ pigs$$

Therefore, a farm should have at least 34 pigs to maintain a stable biogas supply for the operation of the prototype system under the specified conditions. The feasibility of installing the proposed prototype system on pig farms in Ta Manoa subdistrict appears promising, given the substantial number of pigs typically present on these farms (ranging from 100 to 700 pigs). With such a large population of pigs, there is ample potential for sufficient biogas production to support the operation of the system.

Furthermore, considering the scalability of the system, it is estimated that the output power can be increased to 5 kW by utilizing the largest 390-cc engine available in the GX series and a 7.5-kW induction machine. This scalability allows for meeting higher energy demands or supporting additional applications on the farm.

The selection of a spark-ignition engine commonly used in agricultural equipment, such as water pumps and sprayers, offers several advantages. Firstly, the familiarity of the engine among the local community facilitates maintenance, as people are accustomed to its operation and upkeep. Additionally, the availability of spare parts and expertise for engine maintenance locally enhances the system's reliability and reduces maintenance costs.

Overall, installing the proposed prototype system on pig farms in Ta Manoa subdistrict appears feasible, offering a sustainable energy solution while leveraging existing resources and community expertise.

4.3.2 Economic viability

Table 7. presents a summary of the capital costs, operating costs, and salvage values of the components of the biogas power generation system, excluding the anaerobic digester and purification components. The main operating cost considered is the maintenance of the engine. In this analysis, the assumed system lifetime is five years, with the engine operating for 8 hours daily, totaling 14,600 hours. It's worth noting that a biogas-fueled spark-ignition engine can typically operate for up to 60,000 hours [8].

The life-cycle cost (LCC) for the five-year period is calculated to be $1,046 with an interest rate of 7%. Importantly, both the power converter and SEIG can undergo overhauls after the project's lifespan and be reused in new projects, thus providing potential cost savings for future endeavors.

This analysis provides a comprehensive understanding of the financial aspects of the biogas power generation system, facilitating informed decision-making regarding investment and operation.

Table 7. Break-down costs of the proposed SEIG-based biogas power generation system.

Parts	Capital cost	Operating cost	Salvage value
Engine with biogas modification	260 US$	35 US$	-
Generator (SEIG)	150 US$	-	75 US$
Power converter	450 US$	-	200 US$
Housing and piping	140 US$	7 US$	-
Total	1,000 US$	42 US$	270 US$

***As of May 1, 2024, the current currency value is 1 USD equal to 36.14 THB.**

Assume there is a 10% system unavailability due to maintenance and low biogas production. An energy yield per year at 1.2 kW is

1.2 kW × 8 hours × 365 days × 0.9 = 3,153 kWh.

Each year's revenue is estimated to be 378.36 US$ with a retail electricity price of 0.12 US$. Thus, the payback period will be 2.76 years. Therefore, the levelized cost of electricity (LCOE) for the whole project lifetime is 0.07 US$/kWh.

4.4 Analyzing biogas-fueled consumption in the proposed power generation

In the previous test, we used one of the pig farm waste biogas sources mentioned in the section above. It was found to have a maximum power capacity of 1.2 kW. We analyzed the amount of pig manure required per hour for this farm. Based on the data from Table 2, the results are as follows: The system requires 0.217 m^3 of biogas per hour, equivalent to a minimum of 8.47 kilograms of raw materials per hour. Assume we want to produce electricity 8 hours per day at 1.2 kW. That means this pig farm needs to have at least 34 pigs.

In addition, we also analyzed and classified the required raw material quantities for power generation at 1.2 kW per hour for other types of waste. From the agricultural and livestock sectors, as shown in Tables 8 and 9.

Table 8 Raw material for power generation at 1.2 kW per hour (Agricultural sector).

Type	Waste	Biogas Production rate (m³/kg(dry))	Require material (kg)	Dry material (kg)	Raw material (kg)	Product mass (kg)
1. Rice	*Straw*	0.162	6.83	6.83	6.83	58.99
	Trunk	0.250	4.423	6.32	9.03	28.14
2. Corn	*Leaves*	0.225	4.92	5.46	6.07	19.59
	Stubble	0.344	3.21.	3.57	3.97	25.35
3. Sugarcane	*Leaves and Shoots*	0.262	4.22.	6.03	8.617	23.38
	Stems and Leaves	0.274	4.04	6.21	9.557	222.06
4. Cassava	*Rhizome*	0.141	7.84	12.07	18.567	120.15

Table 9 Raw material for power generation at 1.2 kW per hour (Livestock sector).

Type	Biogas Production rate (m³/kg(solids))	Require material (kg)	Solid material (kg)	Raw material (kg)
1. Beef cattle	0.307	3.60	4.16	8.32
2. Dairy Cattle	0.307	3.60	4.16	5.20
3. Breeder Pigs	0.217	5.09	6.78	8.48
4. Piglets	0.217	5.09	6.78	8.48
5. Fattening Pigs	0.217	5.09	6.78	8.48
6. Chickens	0.242	4.57	5.96	7.45

CHAPTER VI

CONCLUSION

It appears you have provided a detailed description of a biogas-powered electrical generation system. Here is a summarized breakdown:

1. Engine: A 196-cc four-stroke single-cylinder ignition engine, modified to run on biogas derived from pig manure using a gas conversion kit.

2. Generator: The engine drives a 2-pole 2.2-kW squirrel-cage inductor motor, configured as a self-excited induction generator.

3. Back-to-Back Converter: Developed for generator control and integration with a 220-V 50-Hz single-phase network. This converter system consists of:

   - Generator-Side Converter: Utilizes a three-phase PWM rectifier to transfer active power to the grid-side converter and supply reactive power back to the generator for voltage regulation.

   - Grid-Side Converter: Employs an LCL-filtered voltage source inverter with multi-frequency unbalanced synchronous reference frame control. This ensures that the injected output current complies with the IEEE 1547 standard, which is crucial for grid integration.

4. Control Systems:

   - Generator-Side Control: Implements notch filter-based bus voltage control to effectively mitigate inter-harmonic components in the generator current induced by oscillating power from the grid-side converter.

   - Grid-Side Control: Utilizes multi-frequency unbalanced synchronous reference frame control to manage the injected output current and ensure compliance with grid standards, particularly IEEE 1547.

Overall, this system enables efficient and compliant biogas-based power generation, leveraging advanced control strategies and converter technologies to facilitate seamless integration with the grid. The advantages of the proposed biogas power generation system, as summarized, are as follows:

1. Low Investment Cost: The system offers a cost-effective solution for power generation, making it accessible to a wide range of users, including small-scale agricultural operations like swine farms.

2. Local Availability of Components: Spark-ignition engines and induction machines, key components of the system, are manufactured in Thailand and are readily available in the local market. This enhances accessibility and reduces procurement lead times.

3. Ease of Operation: The system is designed for simplicity and ease of operation, making it suitable for deployment in rural or remote areas where technical expertise may be limited. Additionally, the familiarity of the community with engine operation facilitates maintenance and troubleshooting tasks.

4. Sustainable Energy Source: By utilizing biogas derived from swine manure, the system contributes to sustainable waste management practices and reduces reliance on fossil fuels. It provides an environmentally friendly alternative for power generation, aligning with sustainability goals.

5. Financial Viability: The levelized cost of electricity is estimated to be 0.07 US$/kWh, indicating favorable economics compared to conventional energy sources. Additionally, the relatively short payback period of 2.76 years enhances the financial attractiveness of the system.

6. The system is a dispatchable renewable source that can be used for grid support.

7. Near-sinusoidal generator and output currents impose a low loss on the generator.

Overall, the proposed biogas power generation system offers a range of benefits, including affordability, local availability of components, ease of operation, environmental sustainability, and favorable financial returns. These advantages position it as a viable and attractive solution for decentralized power generation, particularly in rural agricultural settings like swine farms.

Future work will focus on optimizing biogas production through advanced feedstock management and pre-treatment techniques, enhancing the anaerobic digestion process with specialized microbial consortia, and improving reactor design for scalability. Additionally, efforts will be directed towards upgrading biogas quality by removing contaminants and producing biomethane, ensuring sustainable feedstock sourcing, and mitigating environmental impacts. Technological innovations, such as smart control systems and collaborative R&D, along with supportive economic and policy frameworks, will be essential to maximize the efficiency and sustainability of biogas systems, aligning with Thailand's Bio-Circular-Green (BCG) economy model.
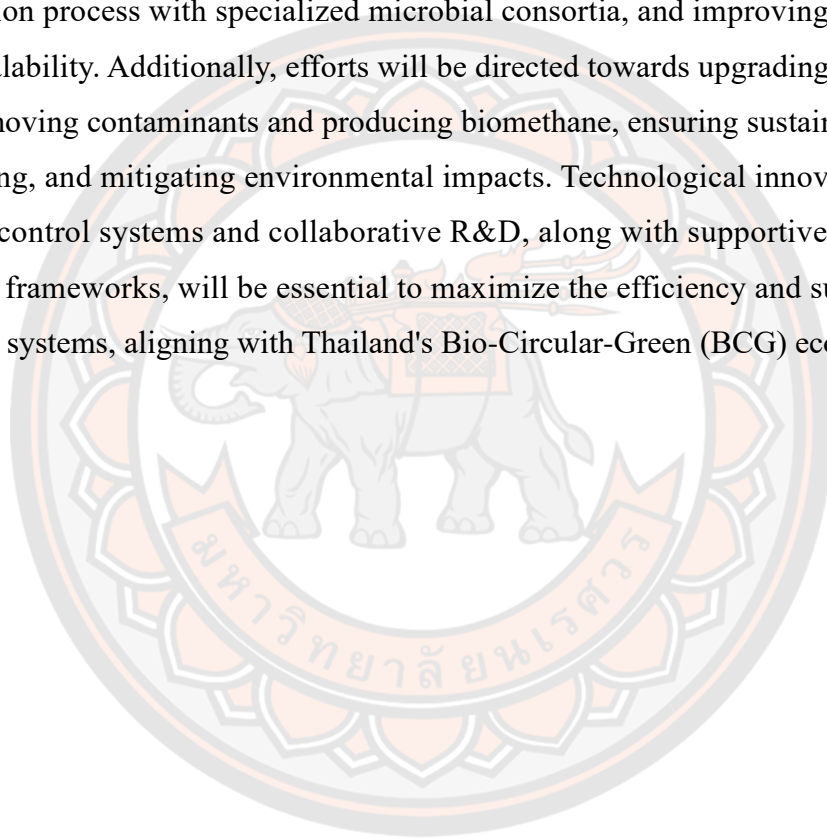
REFERENCES

REFERENCES

[1] Energy Policy and Planning office. Thailand power development plan 2018 Rev. 3 [Internet]. 2018 [cited 2019 Nov 15]. Available from: https://www.eppo.go.th/ images/Infromation_service/NEWS/2018/PDP_ Public_ Hearing2018_3.pdf.

[2] Palapleevalya P, Poboon C, Mungcharoen T. Development of sustainable consumption and production indicators for industrial sector according to circular economy principles in Thailand. Interdiscip Res Rev. 2021;16(6):13-8.

[3] Edyvean RG, Apiwatanapiwat W, Vaithanomsat P, Boondaeng A, Janchai P, Sophonthammaphat S. The bio-circular green economy model in thailand – a comparative review. Agr Nat Resour. 2023;57(1):51-64.

[4] Liu Y, Ma X, Shu L, Hancke GP, Abu-Mahfouz AM. From industry 4.0 to agriculture 4.0: current status, enabling technologies. IEEE Trans Industr Inform. 2021;17(6):4322-34.

[5] Scot MK, Furstenau LB, Kipper LM, Giraldo FD, López-Robles JR, Cobo MJ, et al. Precision techniques and agriculture 4.0 technologies to promote sustainability in the coffee sector: state of the art, challenges and future trends. IEEE Access. 2020;8:149854-67.

[6] Cheng WM, Liu HJ, Chen R, Chang WC, Yuan JJ, Chen J, et al. A real and novel smart agriculture implementation with IoT technology. The 9th International Conference on Orange Technology (ICOT); 2021 Dec 16-17; Tainan, Taiwan. USA: IEEE; 2021. p. 1-4.

[7] Aceleanu MI, Şerban AC, Suciu MC, Biţoiu TI. The management of municipal waste through circular economy in the context of smart cities development. IEEE Access. 2019;7:133602-14.

[8] Khotmanee S, Pinsopon U. A study on biogas production potential in Thailand 2019. The 7th International Conference on Engineering–Applied Sciences and Technology (ICEAST); 2021 Apr 1-3; Pattaya, Thailand. USA: IEEE; 2021. p. 269-72.

[9] Chanathaworn J, Dussadee N. Application of supporting media for improvement of anaerobic digestion performance and biogas production. Int J Renew Energy. 2017;12(2):65-74.

[10] Schlegel M, Kanswohl N, Rossel D, Sakalauskas A. Essential technical parameters for effective biogas production. Agron Res. 2008;6(SI):341-8.

[11] Obaideen, K.; Abdelkareem, M.A.; Wilberforce, T.; Elsaid, K.; Sayed, E.T.; Maghrabie, H.M.; Olabi, A. Biogas role in achievement of the sustainable development goals: Evaluation, Challenges, and Guidelines. J. Taiwan Inst. Chem. Eng. 2022, 131, 104207.

[12] Czubaszek, R.; Wysocka-Czubaszek, A.; Wichtmann, W.; Banaszuk, P. Specific Methane Yield of Wetland Biomass in Dry and Wet Fermentation Technologies. Energies 2021, 14, 8373.

[13] Tauber, J.; Ramsbacher, A.; Svardal, K.; Krampe, J. Energetic Potential for Biological Methanation in Anaerobic Sewage Sludge Digesters in Austria. Energies 2021, 14, 6618.

[14] Seruga, P.; Krzywonos, M.; Boer, E.D.; Nied´zwiecki, A.; Urbanowska, A.; Pawlak-Kruczek, H. Anaerobic Digestion as a Component of Circular Bio economy & mdash; Case Study Approach. Energies 2023, 16, 140.

[15] Ingale, G.U.; Kwon, H.-M.; Jeong, S.; Park, D.; Kim, W.; Bang, B.; Lim, Y.-I.; Kim, S.W.; Kang, Y.-B.; Mun, J.; et al. Assessment of Greenhouse Gas Emissions from Hydrogen Production Processes: Turquoise Hydrogen vs. Steam Methane Reforming. Energies 2022, 15, 8679.

[16] Athanasiou, C.; Drosakis, C.; Booto, G.K.; Elmasides, C. Economic Feasibility of Power/Heat Cogeneration by Biogas–Solid Oxide Fuel Cell (SOFC) Integrated Systems. Energies 2023, 16, 404.

[17] Chang, C.C.; Do, M.V.; Hsu,W.L.; Liu, B.L.; Chang, C.Y.; Chen, Y.H.; Yuan, M.-H.; Lin, C.-F.; Yu, C.-P.; Chen, Y.H.; et al. A case study on the electricity generation using a micro gas turbine fuelled by biogas from a sewage treatment plant. Energies 2019,12, 2424.

[18] Xiao, G.; Yang, T.; Liu, H.; Ni, D.; Ferrari, M.L.; Li, M.; Luo, Z.; Cen, K.; Ni, M. Recuperators for micro gas turbines: A review. Appl. Energy 2017, 197, 83–99.

[19] Yanmar Holdings. Cogeneration Systems—CP Series (Bio Gas). 2023. Available online: https://www.yanmar.com/en_th/energy/cogeneration_systems/biogas/ (accessed on 16 June 2023).

[20] Caterpillar. Gas Generator Sets G3520C. 2023. Available online: https://www.cat.com/en_US/products/new/power-systems/electric-power/gas-generator-sets/18483554.html# (accessed on 16 June 2023).

[21] Verma, S.; Das, L.M.; Kaushik, S.C. Effects of varying composition of biogas on performance and emission characteristics of compression ignition engine using exergy analysis. Energy Convers. Manag. 2017, 138, 346–359.

[22] Homdoung, N.; Tippayawong, N.; Dussadee, N. Performance and emissions of a modified small engine operated on producer gas. Energy Convers. Manag. 2015, 94, 286–292.

[23] Yingjian, L.; Qi, Q.; Xiangzhu, H.; Jiezhi, L. Energy balance and efficiency analysis for power generation in internal combustion engine sets using biogas. Sustain. Energy Technol. Assess. 2014, 6, 25–33.

[24] Capaldi, P.; Daliento, A.; Rizzo, R. An innovative 10 kW microcogenerator suitable for off grid application and fed with syngas or biogas. In Proceedings of the Universities Power Engineering Conference, Cluj-Napoca, Romania, 2–5 September 2014.

[25] Da Costa, R.B.R.; Valle, R.M.; Hernández, J.J.; Malaquias, A.C.T.; Coronado, C.J.; Pujatti, F.J.P. Experimental investigation on the potential of biogas/ethanol dual-fuel spark-ignition engine for power generation: Combustion, performance and pollutant emission analysis. Appl. Energy 2020, 261, 114438.

[26] Karakitie, E.D.; Aralu, C.E.; Fadare, A.D. Performance charateristics of a conventional spark ignition petrol engine powered by biogas. Fuel Commun. 2022, 10, 100032.

[27] Bash, M.; Pekaret, S.; Sudhoff, S.; Whitmore, J.; Fratzen, M. A comparison of permanent magnet and wound rotor synchronous machines for portable power generation. In Proceedings of the 2010 Power and Energy Conference at Illinois (PECI), Urbana, IL, USA, 12–13 February 2010.

[28] Wang, L.; Lin, P. Analysis of a Commercial Biogas Generation System Using a Gas Engine–Induction Generator Set. IEEE Trans. Energy Convers. 2009, 24, 230–239.

[29] Bellini, A.; Franceschini, G.; Lorenzani, E.; Tassoni, C.; Tomaiuolo, M. Field Oriented Control of Self-Excited Induction Generator for Distributed Cogeneration Plants. In Proceedings of the 41st IEEE Industry Applications Conference, Tampa, FL, USA, 8–12 October 2006.

[30] Klíma, J. Stand Alone Bio-Gas Power Plants with Induction Generator and PWM Voltage Source Inverter. IFAC Proc. Vol. 1997, 30, 137–142.

[31] Singh, G.K. Self-excited induction generator research—A survey. Electr. Power Syst. Res. 2004, 69, 107–114.]

[32] Krishna, V.M.; Sandeep, V.; Murthy, S.; Yadlapati, K. Experimental investigation on performance comparison of self-excited induction generator and permanent magnet synchronous generator for small scale renewable energy applications. Renew. Energy 2022, 195, 431–441.

[33] Krause, P. C., Wasynczuk, O., & Sudhoff, S. D. (1994). Analysis of Electric Machinery. IEEE Press Series on Power Engineering. Wiley-IEEE Press.

[34] Chapman, S. J. (2017). Electric Machinery Fundamentals (5th ed.). McGraw-Hill Education.

[35] Filizadeh, S. (2017). Electric Machines and Drives: Principles, Control, Modeling, and Simulation. Wiley-IEEE Press.

[36] Toliyat, H. A., & Nandi, S. (2013). Electric Machines: Modeling, Condition Monitoring, and Fault Diagnosis. CRC Press.

[37] Sen, P. C. (1997). Principles of Electric Machines and Power Electronics (2nd ed.). Wiley.

[38] Hughes, A., & Drury, B. (2013). Electric Motors and Drives: Fundamentals, Types and Applications (4th ed.). Newnes.

[39] T. Ahmed, K. Nishida, M. Nakaoka, and Lee Hyun-Woo, "Self-excited inductiongenerator with simple voltage regulation scheme for wind energy,"in Proc. 30th Annual Conference of IEEE Industrial Electronics Society (IECON2004) 2004, pp. 86-91 Vol. 1.

[40] A. Nesba, R. Ibtiouen, S. Mekhtoub, O. Touhami, S. Bacha, D. Riu, and M. Benhaddadi, "Analysis of self-excited induction generator feeding DC loads for low-cost renewable energy applications," in Proc. IEEE International Electric Machines and Drives Conference (IEMDC '09), 2009, pp. 812-817.

[41] N. Kimura, Hamada Tomoyuki, T. Morizane, and K. Taniguchi, "Control of PFC converter with inverter excited induction generator for advanced wind power generation system," in Proc. IEEE Power Electronics Specialists Conference (PESC2008), 2008, pp. 4439-4445.

[42] A. Sikorski and M. Korzeniewski, "AC/DC/AC converter in a small hydroelectric power plant," Bulletin of the Polish Academy of Sciences: Technical Sciences, vol. 59, pp.507-511, 2011.

[43] H. Wang, et al., "Experiment study of squirrel-cage induction generator for the full-scale wind power converter," in 7th International Power Electronics and Motion Control Conference (IPEMC), 2012, pp. 1457-1463.

[44] A. Bellini, et al., "Field Oriented Control of Self-Excited Induction Generator for Distributed Cogeneration Plants," in the 41st IEEE Industry Applications Conference, 2006, pp. 1738-1744.

[45] G. Cimuca, et al., "Design and Control Strategies of an Induction-MachineBased Flywheel Energy Storage System Associated to a Variable-Speed Wind Generator,"IEEE Transactions on Energy Conversion, vol. 25, pp. 526-534, 2010.

[46] H. R. Mosaddegh and H. A. Zarchi, "Variable structure direct torque control of brushless doubly fed induction generator for wind turbine applications," in Proc.

2014 22nd Iranian Conference on Electrical Engineering (ICEE), 2014, pp. 671-676.

[47] Yuttana Khumsuwan, "Direct Torque Control Strategies for a Stand-alone SelfExcited Induction Generator," The Thailand Research Fund (TRF), 2010.

[48] Li Yingjian, Qiu Qi, He Xiangzhu, and Li Jiezhi, "Energy balance and efficiency analysis for power generation in internal combustion engine sets using biogas," Sustainable Energy Technologies and Assessments, vol. 6, pp. 25-33, 2014.

[49] Kulthida Sawangphon, Warunee Tia and Pawinee Chaiprasert, "A Feasibility Study of Power Generation Using Biogas from Cellulosic Materials, " KMUTT Research and Development Journal. Vol. 36. No. 4. pp. 477-492.

[50] Honda. GX120/160/200. 2023. Available online: https://engines.honda.com/models/model-detail/mid-gx#Features (accessed on 16 June 2023).

[51] Senthil Kumar, S.; Kumaresan, N.; Subbiah, M. Analysis and control of capacitor-excited induction generators connected to a micro-grid through power electronic converters. Generation, Transmission & Distribution. IET 2015, 9, 911–920.

[52] Singh, B.; Niwas, R. Performance of synchronous reluctance generator for DG set based standalone supply system. Electr. Power Syst. Res. 2016, 133, 93–103. [CrossRef]

[53] Braga, A.; Rezek, A.; Silva, V.; Viana, A.; Bortoni, E.; Sanchez, W.; Ribeiro, P. Isolated induction generator in a rural Brazilian area: Field performance tests. Renew. Energy 2015, 83, 1352–1361. [CrossRef]

[54] Somkun, S. High performance current control of single-phase grid-connected converter with harmonic mitigation, power extraction and frequency adaptation capabilities. IET Power Electron. 2021, 14, 352–372. [CrossRef]

[55] Monfared, M.; Golestan, S.; Guerrero, J.M. Analysis, design, and experimental verification of a synchronous reference frame voltage control for single-phase inverters. IEEE Trans. Ind. Electron. 2014, 61, 258–269. [CrossRef]

[56] Somkun, S. Unbalanced synchronous reference frame control of singe-phase stand-alone inverter. Int. J. Electr. Power Energy Syst. 2019, 107, 332–343. [CrossRef]

[57] Somkun, S.; Chunkag, V. Unified unbalanced synchronous reference frame current control for single-phase grid-connected voltage-source converters. IEEE Trans. Ind. Electron. 2016, 63, 5425–5436. [CrossRef]

[58] Golestan, S.; Monfared, M.; Freijedo, F.D.; Guerrero, J.M. Dynamics assessment of advanced single-phase PLL structures. IEEE Trans. Ind. Electron. 2013, 60, 2167–2177. [CrossRef]

[59] Wang, J.; Yan, J.D.; Jiang, L.; Zou, J. Delay-dependent stability of single-loop controlled grid-connected inverters with LCL filters. IEEE Trans. Power Electron. 2016, 31, 743–757. [CrossRef]

[60] Holmes, D.G.; Lipo, T.A.; McGrath, B.P.; Kong,W.Y. Optimized design of stationary frame three phase AC current regulators. IEEE Trans. Power Electron. 2009, 24, 2417–2426. [CrossRef]

[61] Sangwongwanich, A.; Abdelhakim, A.; Yang, Y.; Zhou, K. Chapter 6—Control of Single-Phase and Three-Phase DC/AC Converters. In Control of Power Electronic Converters and Systems; Blaabjerg, F., Ed.; Academic Press: Cambridge, MA, USA, 2018; pp. 153–173.

[62] Sedpho, S. Community Biogas from Swine Farms Phase 3 at Thamanao Sub-District, Chaibadan District, Lopburi Province, Thailand; Thailand Voluntary Emission Reduction Program; Tha Manao Subdistrict Administrative Organization: Lopburi, Thailand, 2020.

[63] Pinate,W.; Dangphonthong, D.; Sirirach, S.; Sukkhon, S. Removal of hydrogen sulfide (H2S) from biogas for the community in the province of Maha Sarakham. J. Phys. Conf. Ser. 2017, 901, 012049. [CrossRef]

[64] 1547-2018; IEEE Standard for Interconnection and Interoperability of Distributed Energy Resources with Associated Electric Power Systems Interfaces. Revision of IEEE Std 1547–2003; IEEE Standards Coordinating Committee: New York, NY, USA, 2018; pp. 1–138.

[65] Adriani F, Agung TK, Syafii, editors. IoT System for Household Electrical Appliance Monitoring and Control. 2022 International Conference on Technology and Policy in Energy and Electric Power (ICT-PEP); 2022 18-20 Oct. 2022.

[66] Afida J, Sera Syarmila S, Azimah Abdul G, Thirukumaran R, Surizal N. A Reliable Architecture for IoT-based Aquatic Monitoring System of Coral Reef and Algae. Journal of Advanced Research in Applied Sciences and Engineering Technology. 2023;29(3):139-46.

[67] Pokress, S.C. and Veiga, J.J.D. 2013. MIT App Inventor enabling personal mobile computing. arXiv preprint arXiv: 1310. 2830v2. 24 Oct 2013.

[68] Younis MF, Alwan ZS, editors. Monitoring the performance of cloud real-time databases: A firebase case study. 2023 Al-Sadiq International Conference on Communication and Information Technology (AICCIT); 2023 4-6 July 2023.

[69] Goswami L, Agrawal P, editors. IOT based Diagnosing of Fault Detection in Power Line Transmission through GOOGLE Firebase database. 2020 4th International Conference on Trends in Electronics and Informatics (ICOEI)(48184); 2020 15-17 June 2020.

BIOGRAPHY

Name-Surname   Panupon Trairat

Date of Birth   21 August 1991

Address   145 M.6, Chantima, Lankrabue, Kamphaengphet 62170

Education Background   2014 - Bachelor of Engineering: Electrical Engineering from Naresuan University - Phitsanulok, Thailand
2018 - Master of Engineering: Electrical Engineering from Naresuan University - Phitsanulok, Thailand

Publication   Trairat, Panupon, Sakda Somkun, Tanakorn Kaewchum, Tawat Suriwong, Pisit Maneechot, and Tanongkiat Kiatsiriroat. 2023. "Biogas-Powered Small Power Generation System Designed for the Agricultural Sector to Support the BCG Model in Thailand". Engineering and Applied Science Research 50 (6):548-60. https://ph01.tci-thaijo.org/index.php/easr/article/view/252387.

Trairat, Panupon, Sakda Somkun, Tanakorn Kaewchum, Tawat Suriwong, Pisit Maneechot, Teerapon Panpho, Wikarn Wansungnern, Sathit Banthuek, Bongkot Prasit, and Tanongkiat Kiatsiriroat. 2023. "Grid Integration of Livestock Biogas Using Self-Excited Induction Generator and Spark-Ignition Engine" Energies 16, no. 13: 4963. https://doi.org/10.3390/en16134963

APPENDIX

MDPI

Article

Grid Integration of Livestock Biogas Using Self-Excited Induction Generator and Spark-Ignition Engine

Panupon Trairat [1], Sakda Somkun [1,*], Tanakorn Kaewchum [1], Tawat Suriwong [1], Pisit Maneechot [1], Teerapon Panpho [1], Wikarn Wansungnern [1], Sathit Banthuek [1], Bongkot Prasit [1] and Tanongkiat Kiatsiriroat [2]

[1] School of Renewable Energy and Smart Grid Technology (SGtech), Naresuan University, Phitsanulok 65000, Thailand; panupont61@nu.ac.th (P.T.); tanakornka65@nu.ac.th (T.K.); tawats@nu.ac.th (T.S.); pisitm@nu.ac.th (P.M.); wikarnw@nu.ac.th (W.W.); sathitb@nu.ac.th (S.B.); bonggotp@nu.ac.th (B.P.)

[2] Department of Mechanical Engineering, Chiang Mai University, Chiang Mai 50300, Thailand; tanong@dome.eng.cmu.ac.th

* Correspondence: sakdaso@nu.ac.th

Abstract: This study developed a grid-connected biogas power generation system for a rural community using a 3-phase 2.2 kW squirrel-cage induction machine as the self-excited induction generator. The generator was driven by a 196 cc single-cylinder spark-ignition engine fueled by biogas. We developed a back-to-back converter that consists of a 3-phase PWM rectifier as the generator-side converter and a single-phase LCL-filtered grid-connected inverter. The generator-side converter transferred the active power to the grid-side converter and supplied the reactive power control back to the generator. The notch filter-based bus voltage control on the generator side mitigated the inter-harmonics in the generator current. The injected grid current complied with the IEEE 1547 standard because of the multi-frequency unbalanced synchronous reference frame control. The proposed system was validated with biogas produced from pig manure at a pig farm in central Thailand, which found a maximum output of 1.2 kW with a thermal system efficiency of 10.7%. The proposed system was scheduled to operate at 1.2 kW for 8 h per day with a levelized cost of 0.07 US\$/kWh, 42% cheaper than the retail electricity price, and a payback period of 2.76 years. The proposed system is suitable for a farm with a minimum of 34 pigs.

Keywords: back-to-back converter; biogas; induction generator; spark-ignition engine; sustainable energy

check for
updates

1. Introduction

Biogas production is a form of sustainable waste management for agricultural, industrial, and residential sectors, which has direct impacts and contributions to 12 out of the 17 sustainable development goals (SDGs) [1]. Agricultural, industrial, and municipal organic waste and sewage sludge are converted to biogas through fermentation of microorganisms under anaerobic conditions [2,3]. Biogas production from livestock farms in developing countries has potential benefits in the reduction of greenhouse gas (GHG) emissions and environment-friendly waste management [4]. Biogas fuel is normally utilized for heat production, transportation, and electricity production [1].

Biogas can be converted directly to electricity through an electrochemical process using solid oxide fuel cells (SOFCs) with near-zero GHG emissions. However, complicated biogas cleaning and compression systems are required to make the SOFCs suitable for industrial scales [5]. Moreover, the high investment cost is a barrier to adaptation in developing countries [6]. Nevertheless, biogas-fed micro gas turbines are promising for power generation from sewage treatment systems [7,8]. Micro gas turbines fueled from biogas have efficiencies between 20–30% [8], with a rotational speed between 1433π to 8000π rad/s. A micro gas turbine is well equipped with a mechanical transmission system coupled with a generator providing the 50/60 Hz electrical output. The GHG emission is far less

than the conventional internal combustion engines. Commercial micro gas turbines range from 30 kW to over 200 kW [8]. Internal combustion engine technologies are fully mature. Commercial biogas engines for power generation range from 25 kW [9] to 2 MW [10] with an electrical efficiency of up to 40%. Modification of standard internal combustion engines fueled by biogas has been widely explored. Compression–ignition engines can be modified to be fueled simultaneously by diesel and biogas [11]. A compression–ignition engine can be alternatively converted into a spark–ignition engine which can be solely fed by producer gas or biogas [12,13]. Standard spark–ignition engines require a slight modification for using biogas as the sole fuel [14–16].

Electrically excited synchronous generators are normally used to convert the mechanical work of the biogas-fed engines to AC electricity [11–13,15]. The output frequency is regulated through the engine speed governor for a stand-alone application, while the output voltage is regulated via the generator excitation current. For a grid connection, it must be ensured that the generator voltage and frequency exactly match those of the grid before synchronization. Permanent magnet synchronous generators (PMSGs) offer more compactness than electrically excited synchronous generators [17], which were adopted for biogas-fed power generation systems [9,14]. A power electronic converter is mandatory for regulating the output voltage and for grid integration [9,10,14].

Self-excited induction generators (SEIGs) can be another candidate for biogas power generation [18–20]. SEIGs have a rugged construction which requires almost no maintenance, which can use commercial 3-phase induction machines as generators [21]. Moreover, an SEIG has a cost much lower than a PSMG [22]. SEIGs are widely adopted for wind [23,24] and small hydro [25–28] energy systems. However, SEIGs require reactive power for excitation and regulation of the terminal voltage [29]. For the variable frequency stand-alone system, SEIGs are driven by variable speed prime movers, e.g., wind and hydro turbines, which are supplied from capacitor banks [20,25,30,31], hybrid excitation systems consisting of static var generators (SVGs) and capacitor banks [19,23,24,26–28]. A 3-phase SEIG can be operated as a stand-alone single-phase AC using a current-balancing circuit and a dummy load [32]. For grid-connected operation, the SEIG can be operated with a fixed speed and variable speed prime movers. For the fixed speed operation, the SEIG connects directly to the grid [18], which is suitable for a governed speed prime mover with a limited mechanical speed range of 1–5% above the synchronous speed. For the variable-speed grid-connected operation, the SEIG connects to the grid through an AC–DC–AC link power converter [27].

In one application of biogas-powered SEIG-based generator systems, a 45 kW SEIG fed a three-phase stand-alone system through a diode bridge rectifier and voltage source converter (VSC) [20]. A 100 kW commercial gas engine–SEIG set was directly connected to a three-phase grid [18]. A 7 kW gas engine–SEIG system directly supplied a 3-phase stand-alone system with a VSC-based SVG for regulation of the generator voltage [19]. The gas engines of these three SEIG-based biogas power generation systems were equipped with a speed regulation system.

As mentioned above, there is no report on single-phase grid-connected biogas power generation systems for a small community with a maximum power less than 5 kW. Therefore, this work reports the development of a grid-connected biogas power generation system for a small pig farm in central Thailand. A 196 cc single-cylinder spark-ignition engine fueled by biogas from anaerobic digestion of pig manure and wastewater was used as the prime mover. A 2.2 kW 3-phase squirrel-cage induction motor was operated as an SEIG. In addition, we developed a power electronic converter for the generator excitation control and integration of a 220 V 50 Hz single-phase grid. Laboratory and field tests validated technical and economic viability were validated.

2. Materials and Methodology

2.1. Selection and Modification of a Spark-Ignition Engine

A Honda GX200T2 QHT air-cooled [33], 4-stroke spark-ignition engine (Tokyo, Japan) with a horizontal shaft was chosen as the prime mover. Table 1 summarizes the engine

specifications. The power–speed and torque–speed characteristics of the engine were reproduced from the specification sheet, as shown in Figure 1. The maximum output power was 4.1 kW at 120π rad/s, with a maximum torque of 12.4 N-m at 83π rad/s according to the SAE J1349 standard. In addition, gasohol, mixed fuel between gasoline and ethanol, with a maximum ethanol content of 10%, can be used with the GX200T2 QHT engine. Thus, this engine is suitable for direct coupling to a two-pole machine with a nominal speed of approximately 100π rad/s. The original carburetor was replaced by a gasoline/liquefied petroleum gas (LPG) carburetor conversion kit, as depicted in Figure 2. This dual fuel carburetor also facilitates the engine to be fed by biogas [16].

Table 1. Parameters of the inverter.

Symbol	Quantity	Value
P_0	Nominal output power	1.5 kW
$V_{LL,B}$	Nominal SEIG line-to-line voltage	220 V
f_{gB}	Nominal SEIG frequency	50 Hz
C_α	Excitation capacitors	40 μF (Δ connection)
V_D	Nominal DC voltage	400 V
V_0	Nominal grid voltage	220 V
f_0	Grid frequency	50 Hz
f_c	Triangular carrier frequency	10 kHz
f_s	Sampling frequency	20 kHz
L_s	SEIG-side inductor	2 mH
C_D	DC bus capacitor	1000 μF
L_1	LCL filter inductor	1 mH
L_2	Grid-side inductor	0.5 mH
C_f	LCL filter capacitor	3 μF
R_f	LCL filter damping resistor	1 Ω

Figure 1. Mechanical characteristics of the Honda GX200T2 QHT engine.
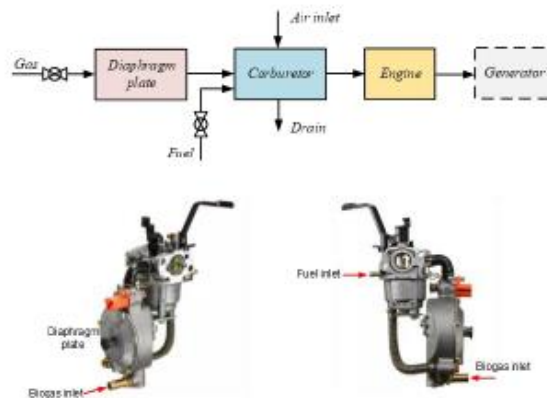
Figure 2. Biogas supply system for the spark–ignition engine.

2.2. Assesment of Possible Power Conversion Topologies

This study selected a Hitachi TFO-K series 220/380 V 2.2 kW 2-pole squirrel-cage induction motor (Tokyo, Japan) for the SEIG. The output of this system was connected to a 220 V 50 Hz single-phase AC grid, which required a minimum DC input voltage of $\sqrt{2} \times 220 = 311$ V. The engine speed was unregulated, so the generator output voltage and frequency were variable. The SEIG required a capacitor bank to build up the generator terminal voltages from a residual flux density in the rotor core. An additional reactive power source was also mandatory, to keep the SEIG excited when supplying the load [21].

Figure 3 depicts possible circuit topologies for this study. In the SEIG with the star connection in Figure 3a with passive excitation, the capacitor bank CB1 supplies a reactive power Q_1 for an initial excitation, which builds a nominal line-to-line voltage of approximately 380 V at no-load [20,34]. A passive rectifier converts the 3-phase AC voltage to the DC bus voltage v_D of approximately 550 V, which feeds an LCL-filtered single-phase insulated-gate bipolar transistor (IGBT) inverter. The capacitor bank CB2 supplies additional reactive power Q_2 for voltage regulation when feeding active power to the grid. Although this circuit has a simple operation, the DC bus voltage is far higher than the grid voltage peak value. This high bus voltage results in a bulky inverter-side inductor L_1 of the LCL filter to limit the current ripple, high switching loss in the inverter, and high semiconductor component ratings.

(a)
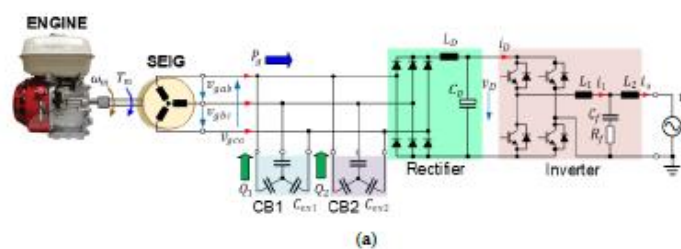
Figure 3. Cont.
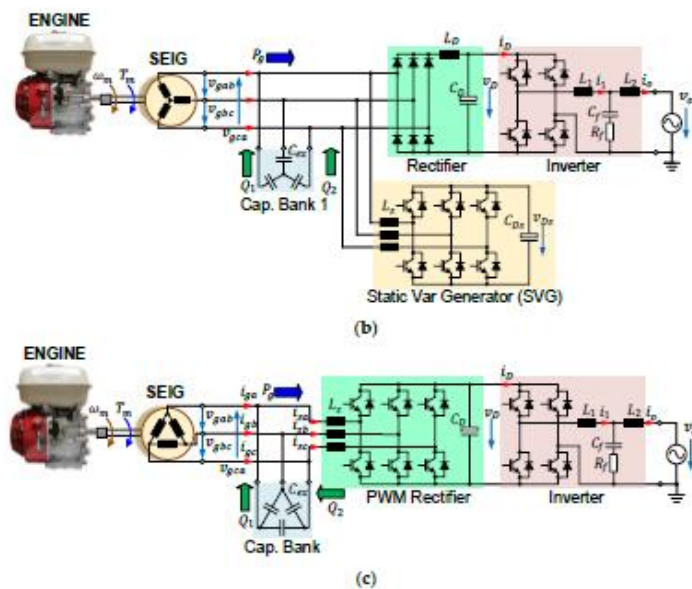
Figure 3. Possible power conversion topologies for the biogas power generation system: (a) Passive rectifier with multi capacitor banks, (b) Passive rectifier with a capacitor bank and an SVG, (c) Proposed back-to-back converter with a capacitor bank.

Moreover, the generator has low efficiency due to the distorted currents drawn by the rectifier. Hybrid excitation schemes in Figure 3b with the reactive power supplied by a static var generator (SVG) provide smooth voltage regulation [26,28,35]. A voltage source converter (VSC) is adopted as the SVG, with L_s as the boosting inductors [28]. The VSC bus voltage v_{Ds} is controlled to be greater than the peak value of the SEIG line-to-line voltage so that the VSC can inject the reactive power Q_2 into the generator for voltage regulation. In addition, the SVG can compensate for the current harmonics of the rectifier so that the SEIG currents become sinusoidal. This circuit topology and its control scheme are complicated and unsuitable for low-power applications. A thyristor-based SVG can be adopted instead of the VSC-based SVG [23,36]. However, the SEIG current harmonics and large DC bus voltage v_D still cause a low system efficiency.

Figure 3c shows the proposed back-to-back converter topology. The SEIG winding is connected as the delta configuration so that the no-load line-to-line voltage is approximately $V_{LL} = 220$ V, with a proper capacitor bank CB1. A VSC-based PWM rectifier is a boost-type power converter that converts the SEIG 3-phase AC voltage to a DC voltage v_D higher than the peak value of the line-to-line input voltage. The DC bus voltage reference value V_D^* is 400 V, which is high enough for the single-phase inverter with lower IGBT rating and switching loss. The VSC-based PWM rectifier also supplies the reactive power Q_2 to the SEIG while drawing the active power P_g. The proposed topology was expected to be more efficient than the passive rectifier topologies in Figure 3a,b, due to the SEIG sinusoidal currents and lower switching losses.

2.3. Proposed SEIG-Based Power Conversion System

Figure 4 depicts the power converter control system. The SEIG-side and grid-side control schemes were implemented on a TMS320F28069 32-bit microcontroller from Texas

Instruments. The voltage and current signals of the SEIG and grid were sampled via the embedded analog-to-digital converters (ADCs), from which the control schemes generated the switching signals from the PWM units for the IGBTs via the gate driver circuits. The SEIG and capacitor bank were considered as a 3-phase AC voltage source with the star connection. Therefore, the virtual phase voltages of the SEIG are defined as follows:

$$
\left.
\begin{aligned}
v'_{ga}(t) &= \hat{V}'_g \cos \omega_g t \\
v'_{gb}(t) &= \hat{V}'_g \cos\left(\omega_g t - \frac{2\pi}{3}\right) \\
v'_{gc}(t) &= \hat{V}'_g \cos\left(\omega_g t - \frac{4\pi}{3}\right)
\end{aligned}
\right\}
\tag{1}
$$

where $\hat{V}'_g = \sqrt{2}\left(V_{LL}/\sqrt{3}\right)$ is the voltage amplitude and ω_g is the generator electrical frequency. The shaft rotational speed is not required. Instead, the shaft speed can be estimated from the generator frequency ω_g, which was used for supervisory control, along with other mechanical parameters such as temperatures, biogas pressure, and gas flow rate.
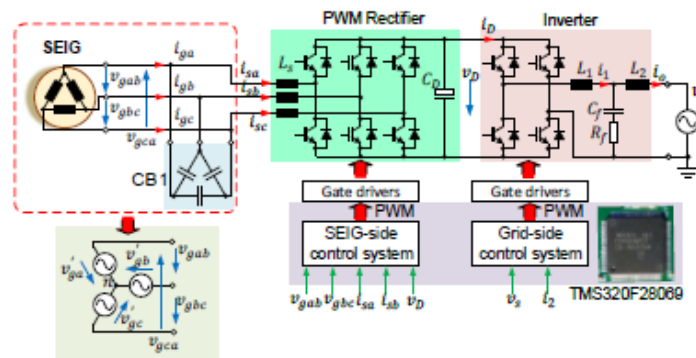
Figure 4. Control structure of the biogas power generation system.

Figure 5 shows the control system of the PWM rectifier in the synchronous reference frame. The superscripts '*' denote the reference signals. The measured physical line to line voltages $v_{gab}(t)$ and $v_{gbc}(t)$ are transformed into a space vector, which is then shifted by $e^{-j\pi/6}/\sqrt{3}$ to calculate the space vector $v'_{g\alpha}(t) + jv'_{g\beta}(t)$ of the virtual phase voltages $v'_{ga}(t)$, $v'_{gb}(t)$ and $v'_{gc}(t)$. The synchronous reference frame phase-locked loop (PLL) estimates the angle θ_g, frequency $\hat{\omega}_g$, and amplitude $\hat{V}'_g$ of the space vector $v'_{g\alpha}(t) + jv'_{g\beta}(t)$ The PWM rectifier currents $i_{sa}(t)$ and $i_{sb}(t)$ are only measured due to the symmetry of the 3-phase 3-wire system for transforming the synchronous reference frame currents $i_{sd}(t)$ and $i_{sq}(t)$. Thus, the instantaneous active and reactive powers $p_s(t)$ and $q_s(t)$ of the PWM rectifier are given as shown:

$$
p_s(t) = \frac{3}{2}\hat{V}'_g i_{sd}(t)
\tag{2}
$$

$$
q_s(t) = \frac{3}{2}\hat{V}'_g i_{sq}(t)
\tag{3}
$$
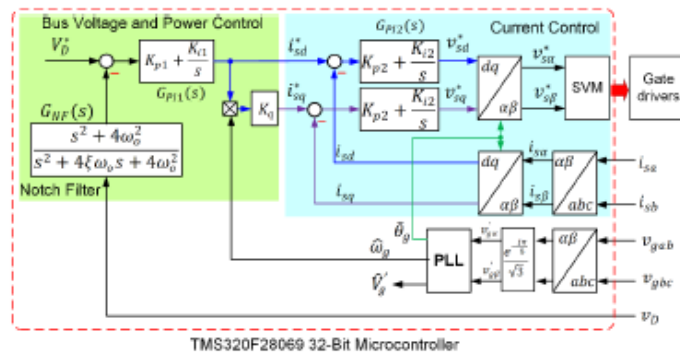
Figure 5. SEIG-side power converter control system.

Assuming there is no loss in the capacitor bank, the SEIG active power $p_g(t)$ and reactive power $q_2(t)$ become the following:

$$p_g(t) = p_s(t) = \frac{3}{2}\hat{V}'_s i_{sd}(t) \tag{4}$$

$$q_2(t) = q_s(t) = \frac{3}{2}\hat{V}'_s i_{sq}(t) \tag{5}$$

The DC bus voltage $v_D(t)$ contains a ripple caused by the oscillating power of the grid-side inverter at the frequency of $2\omega_o$, where $\omega_o = 2\pi f_o$ is the grid frequency. Thus, a second-order notch filter $G_{NF}(s)$ at $2\omega_o$ blocks the bus ripple component before feeding to the bus voltage control loop with a proportional-integral (PI) controller $G_{PI1}(s)$. The bus voltage controller generates the d-axis reference current $i^*_{sd}(t)$ to draw the active power $p_s(t)$ from the SEIG in response to the bus power drawn by the single-phase inverter.

Voltage regulation of a variable-speed SEIG is challenging due to its nonlinear characteristics [23,28,34]. The nominal synchronous speed of this SEIG was 100π rad/s, which can tolerate a speed range of $\pm10\%$. Thus, the mechanical speed range of the engine suited the SEIG well. We proposed a simple open-loop excitation scheme. The q-axis reference current $i^*_{sq}(t)$ was proportional to $i^*_{sd}(t)$ with a constant gain K_q, to produce the reactive power $q_2(t)$ for regulating the SEIG voltage. The sign of the estimated SGIG frequency $\hat{\omega}_g$ defined the reactive power $q_2(t)$'s direction, in the case of the phase sequence opposite to (1). The PI controllers $G_{PI2}(s)$ regulated the dq-axes currents. A space vector modulation (SVM) technique generated the switching signals for the IGBTs.

The $2\omega_o$ ripple component of the bus voltage affects the PWM rectifier and SEIG current waveforms. Figure 6 displays the natural reference frame equivalence of the SEIG-side control system. The PI controllers of the current control loops in Figure 6 are equivalent to the proportional–resonant controllers at the resonant frequency of ω_g. The bus voltage filter $G_{fv}(s)$ attenuates the $2\omega_o$ component $\tilde{v}_{D2\omega_o}$. Let the reference current $i^*_{sd}(t)$ given as below:

$$i^*_d(t) = I^*_g + I_{2\omega_o}\cos(2\omega_o t + \psi) \tag{6}$$

where $\hat{I}_g^*$ is the active power-producing component and $\hat{I}_{2\omega_o} \cos(2\omega_o t + \psi)$ is the resultant of the $2\omega_o$ component. The reference currents i_{sa}^*, i_{sb}^*, and i_{sc}^* in the natural reference frame are obtained from the following:

$$
\begin{bmatrix} i_{sa}^* \\ i_{sb}^* \\ i_{sc}^* \end{bmatrix} = \begin{bmatrix} \cos \omega_g t & -\sin \omega_g t \\ \cos\left(\omega_g t - \frac{2\pi}{3}\right) & -\sin\left(\omega_g t - \frac{2\pi}{3}\right) \\ \cos\left(\omega_g t - \frac{4\pi}{3}\right) & -\sin\left(\omega_g t - \frac{4\pi}{3}\right) \end{bmatrix} \cdot \begin{bmatrix} i_{sd}^* \\ i_{sq}^* \end{bmatrix} \tag{7}
$$
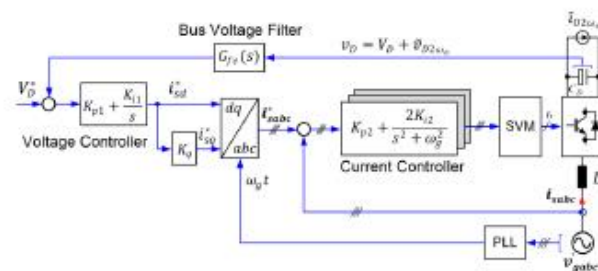
Figure 6. Equivalent SEIG-side power converter control system in the natural reference frame.

Let $i_{sq}^*(t) = k_q i_{sd}^*(t)$, and consider only the $2\omega_o$ component of $i_{sd}^*(t)$, which causes inter-harmonic components $i_{sa,2\omega_o}^*$, $i_{sb,2\omega_o}^*$, and $i_{sc,2\omega_o}^*$ in the natural frame reference currents i_{sa}^*, i_{sb}^*, and i_{sc}^* as follows:

$$
\begin{bmatrix} i_{sa,2\omega_o}^* \\ i_{sb,2\omega_o}^* \\ i_{sc,2\omega_o}^* \end{bmatrix} = \pm \frac{\hat{I}_{2\omega_o}}{2} \begin{bmatrix} \cos\left((2\omega_o \mp \omega_g)t + \psi\right) + k_q \sin\left((2\omega_o \mp \omega_g)t + \psi\right) \\ \cos\left((2\omega_o \mp \omega_g)t - \frac{2\pi}{3} + \psi\right) + k_q \sin\left((2\omega_o \mp \omega_g)t - \frac{2\pi}{3} + \psi\right) \\ \cos\left((2\omega_o \mp \omega_g)t - \frac{4\pi}{3} + \psi\right) + k_q \sin\left((2\omega_o \mp \omega_g)t - \frac{4\pi}{3} + \psi\right) \end{bmatrix} \tag{8}
$$

Thus, the bus voltage filter $G_{fv}(s)$ plays a vital role in mitigating the $(2\omega_o \mp \omega_g)$ components in the PWM rectifier currents. A low-pass filter with a cut-off frequency far below $2\omega_o$ results in a sluggish performance. In this work, we applied a standard second order notch filter $G_{NF}(s)$ to block the $2\omega_o$ component while maintaining fast dynamic performance.

The output stage of the proposed topology in Figure 4 is the single-phase LCL-filtered grid-connected inverter. The damping resistor $\bar{R}_f$ of the LCL filter ensures control stability with a large grid impedance. Grid current $i_o(t)$ feedback control is used in this study. The grid voltage $v_o(t)$ is given here:

$$
v_o(t) = \hat{V}_o \cos \omega_o t \tag{9}
$$

where $\hat{V}_o$ is the voltage amplitude, $\omega_o = 2\pi f_o$ is the grid frequency. The desired grid current $i_o(t)$ is as shown:

$$
i_o(t) = \hat{I}_o \cos(\omega_o t + \varphi_o) \tag{10}
$$

The single-phase inverter is controlled in the virtual synchronous reference frame control by setting $i_{o\alpha}(t) = i_o(t)$ and the orthogonal current $i_{o\beta}(t) = i_o(t) e^{-j\pi/2} = \hat{I}_1 \sin(\omega_o t + \varphi_o)$. The grid current is decoupled into the dq axes using the Park transformation:

$$
\begin{bmatrix} i_{od}(t) \\ i_{oq}(t) \end{bmatrix} = \begin{bmatrix} \cos \omega_o t & \sin \omega_o t \\ \sin \omega_o t & \cos \omega_o t \end{bmatrix} \cdot \begin{bmatrix} i_o(t) \\ i_{o\beta}(t) \end{bmatrix} = \begin{bmatrix} \hat{I}_o \cos \varphi_o \\ \hat{I}_o \sin \varphi_o \end{bmatrix} \tag{11}
$$

The synchronous reference frame control results in the decomposition of the instantaneous power and reactive power as follows [37]:

$$p_o(t) = \frac{\hat{V}_o(t)}{2} \hat{I}_o \cos \varphi_o = \frac{\hat{V}_o}{2} i_{od}(t) \tag{12}$$

$$q_o(t) = -\frac{\hat{V}_o(t)}{2} \hat{I}_o \sin \varphi_o = -\frac{\hat{V}_o}{2} i_{oq}(t) \tag{13}$$

The grid-side control system is implemented in the unbalanced synchronous reference frame, a sub-class of the synchronous reference frame control. Figure 7 depicts the stationary reference frame representation of the synchronous reference frame control. The error signals $e_\alpha(t)$ and $e_\beta(t)$ in the $\alpha\beta-$axes are transformed into the error signals $e_d(t)$ and $e_q(t)$ in the $dq-$axes with the angle $h\omega_o t$. The controllers $H_{DC}(s)$ in the $dq-$axes produce the manipulating signals $y_d(t)$ and $y_q(t)$, which are transformed back to the $\alpha\beta-$axes manipulating signals $y_\alpha(t)$ and $y_\beta(t)$. Applying the convolution and modulation properties of the Laplace transformation [38] yields the stationary reference frame outputs:

$$\begin{bmatrix} y_\alpha(s) \\ y_\beta(s) \end{bmatrix} = \frac{1}{2} \begin{bmatrix} \begin{pmatrix} H_{DC}(s+jh\omega_o) \\ +H_{DC}(s-jh\omega_o) \end{pmatrix} & \begin{pmatrix} -jH_{DC}(s+jh\omega_o) \\ +jH_{DC}(s-jh\omega_o) \end{pmatrix} \\ \begin{pmatrix} jH_{DC}(s+jh\omega_o) \\ -jH_{DC}(s-jh\omega_o) \end{pmatrix} & \begin{pmatrix} H_{DC}(s+jh\omega_o) \\ +H_{DC}(s-jh\omega_o) \end{pmatrix} \end{bmatrix} \begin{bmatrix} e_\alpha(s) \\ e_\beta(s) \end{bmatrix} \tag{14}$$
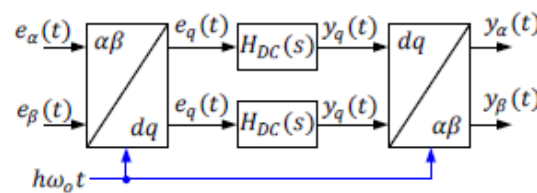
Figure 7. Stationary reference frame representation of the synchronous reference frame control.

If the β-axis input $x_\beta(t) = 0$ and only the output in the α-axis are considered for the single-phase system, the stationary reference frame equivalence of $H_{DC}(s)$ becomes the following:

$$H_{AC}(s) = \frac{y_\alpha(s)}{e(s)} = \frac{1}{2}(H_{DC}(s+jh\omega_o) + H_{DC}(s-jh\omega_o)) \tag{15}$$

If $H_{DC}(s) = K_P + K_I/s$ is the standard PI controller, $H_{AC}(s)$ is as below:

$$H_{AC}(s) = K_P + \frac{K_I}{s^2 + (h\omega_o)^2} \tag{16}$$

The equivalent controller transfer function in the stationary reference frame in (16) is identical to the ideal proportional-resonant controller, which provides an infinite gain at the target frequency $h\omega_o$, ensuring zero steady-state error. This control technique is called the unbalanced synchronous reference frame control, which has been successfully applied for single-phase converters [39,40]. The unbalanced synchronous reference frame control can be implemented in different structures with identical performance [40].

Figure 8a depicts the grid-side control system of the single-phase inverter, which is implemented in the multiple unbalanced synchronous reference frame on the same microcontroller with the SEIG-side control. The proposed control scheme consisted of a fundamental component controller at the grid frequency ω_o, and multiple harmonic

controllers at frequencies $h\omega_o$. The harmonic controllers attenuate low-frequency harmonics in the grid and inverter output voltages due to switching deadtimes [37]. An inverse Park transformation PLL estimates the angle $\theta_o = \omega_o t$ and the grid voltage amplitude $\hat{V}_o$ [41]. A low-pass filter with a time constant of T_{fo} reduces the fast-changing rate of the power reference P_o^* to draw power from the SEIG and engine smoothly. The $d-$axis reference current $i_{od}^*(t)$ is calculated from the filtered reference output power P_{of}^* using (12), whereas the $q-$axis reference current $i_{oq}^* = 0$ is used for a unity power factor. The fundamental current controller uses the grid current as the $\alpha-$axis component current $i_{o\alpha}(t) = i_o(t)$ and the reference current $i_{o\beta}^*$ as the $\beta-$axis component current $i_{o\beta} = i_{o\beta}^*$ for the reference frame transformation [40]. The fundamental grid current components $i_{od}(t)$ and $i_{oq}(t)$ in the $dq-$axes are regulated by the PI controllers $G_{PIO}(s) = K_{Po} + K_{Io1}/s$, whose outputs m_{d1}^* and m_{q1}^* are transformed back to the stationary reference frame. Only the $\alpha-$axis output $m_{\alpha1}^*$ is used. This control structure has inherent power decoupling and frequency adaption capabilities [37]. Figure 8b shows the details of the harmonic current controllers implemented in the modulation/demodulation structure at the frequencies $h\omega_o$. The harmonic controllers have a simpler structure than the fundamental component controller with identical performance. The $\alpha-$axis reference current $i_{o\alpha}^*$ is compared with the grid current $i_o(t)$. The decomposed error signals in the $dq-$axes are regulated by the integral controllers K_{Ioh}/s, from which outputs are transformed back to the $\alpha-$axis signals m_h^*. The output signals of the fundamental current controller $m_{\alpha1}^*$ and the harmonic controller m_h^* form the input signal m^* for the pulse width modulation (PWM) unit embedded in the microcontroller. The transfer function of the grid current controller is equivalent to a proportional–multi-resonant (PMR) controller, as in [37]:

$$G_{io}(s) = \frac{m^*(s)}{i_o^*(s) - i_o(s)} = K_{Po} + \sum_{h=1}^{n} \frac{K_{Ioh}}{s^2 + (h\omega_o)^2} \tag{17}$$
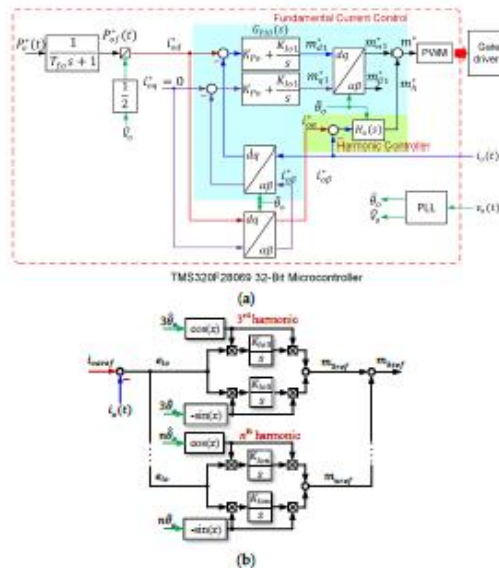

Figure 8. Grid-side control system: (a) Overall control system, (b) Structure of the harmonic control.

2.4. Back-to-Back Converter Design

The proposed power converter in Figure 5 was constructed with parameters listed in Table 1. The excitation capacitors C_{ex} built up the SEIG voltage to the nominal value of $V_{LL} = 220$ V (line to line) at the no-load rotational speed of approximately 100π rad/s. Assuming the efficiency of the converter and SEIG as 70%, the nominal output power was set at 1.5 kW, at which the mechanical input power $P_m = 2.14$ kW, close to the rated power. The SEIG-side and grid-side converters employed the asymmetrical regular sampled PWM technique, with the triangular carrier frequency of $f_c = 10$ kHz and the sampling frequency of $f_s = 20$ kHz. The resonant frequency f_{LCL} is given by the following:

$$f_{LCL} = \frac{1}{2\pi\sqrt{\left(\frac{L_1 L_2}{L_1 + L_2}\right)C_f}} \tag{18}$$

According to Table 1, $f_{LCL} = 5.06$ kHz satisfies the stability criterion [42]:

$$\frac{f_s}{6} < f_{LCL} < \frac{f_s}{2} \tag{19}$$

The grid current control loop with the harmonic controller orders 3rd, 5th, 7th, and 9th was designed at a bandwidth of 1100 Hz [37]. The current control loop of the PWM rectifier was tuned at an approximated bandwidth of 1000 Hz, using the method in [43]. Figure 9 shows the simplified control block diagram of the bus voltage control loop, where the notch filter is approximated as the low-pass filter. The controller parameters K_{p1} and K_{i1} and the notch filter's damping factor ξ were obtained from the extended symmetrical optimum method [44] at a loop bandwidth of 15 Hz.
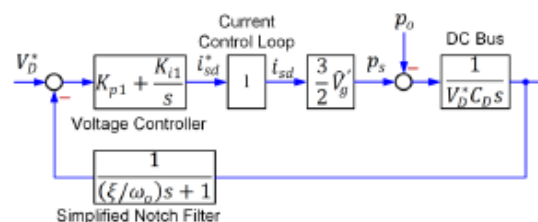
Figure 9. Simplified bus voltage control block diagram.

2.5. Experimental Setup

Figure 10 shows the biogas power generation system prototype, which was installed at Tha Manoa Subdistrict, Chaibadal District, Lopburi, Thailand (15.1998° N, 101.1652° E). Figure 11 depicts the performance evaluation diagram of the prototype system. Gasohol containing 90% 95-octane gasoline and 10% ethanol by volume was used for the laboratory tests. The average thermal input power was determined from the consumption rate using a digital weighing scale monitored in 10 min periods.

The engine was fueled by biogas for the field tests at Tha Manoa Subdistrict. In this community, there are 8 pig farms, each containing 100–700 pigs. The air intake was adjusted experimentally until the engine delivered a stable shaft power for the desired output power. Each farm installed an anaerobic covered lagoon to produce biogas from pig slurry, a primary measure for waste management. The byproduct biogas has been primarily utilized for cooking. Sediment from anaerobic digestion was used for soil fertilization within the community. This biogas production project joined the Thailand Voluntary Emission Reduction (T-Ver) Program, which was verified to reduce the emissions by 1634 tCO_2e/year between 2015–2022 [45]. The produced biogas from each lagoon was purified by passing through $Fe(OH)_3$ absorbent granules, which were made from grey cement mixed with fine

sand soaking in FeCl$_3$ and NaOH [46]. Fan blowers pressurized the upgraded biogas for distribution to 230 households for cooking between 5.00 am–9.00 am and 4.00 pm–9.00 pm daily. The excess biogas had been planned to be used for power generation.

Figure 10. Prototype of the biogas power generation system.
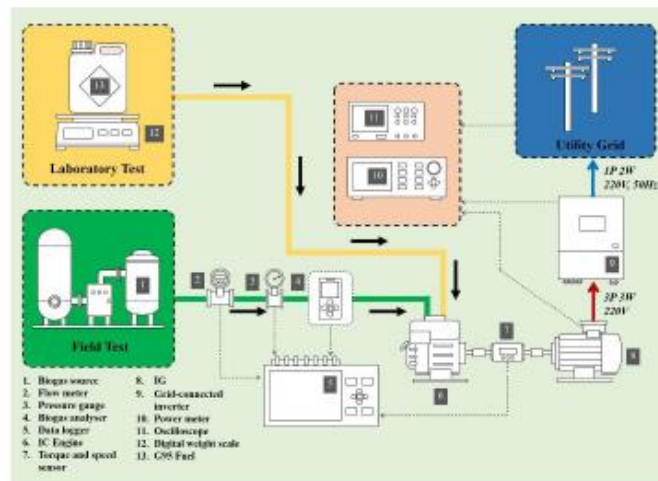
Figure 11. Performance evaluation diagram of the biogas power generation system.

The thermal input power was determined from the volumetric flow rate using an Omega FMA-A2100 thermal mass flowmeter (Stamford, CT, USA) and CH$_4$ content was monitored by an IRCD4 gas analyzer from Beijing Shi'An Technology (Beijing, China). The shaft torque and speed and mechanical power were obtained from a CALT DYN-200 torque–speed sensor (Shanghai, China) mounted between the engine and the SEIG. Electrical parameters at the SEIG and converter outputs were measured by a Yokogawa WT300 4-channel power analyzer (Tokyo, Japan). Current and voltage waveforms were recorded by an ISO-TECH IDS-1074B 4-channel digital oscilloscope (Corby, UK).

3. Results

3.1. Control Performance of the SEIG and Back-to-Back Converter

This section validates the laboratory performance of the SEIG and back-to-back converter system. The SEIG was driven by the GX200T2 QHT engine and fueled by gasohol. The reactive power gain $K_q = 0.5$ was determined experimentally to keep the ratio between the SEIG voltage and frequency constant throughout the operating range.

Figure 12a shows the SEIG voltage build-up period. In the beginning, a small SEIG voltage $v_{gab}(t)$ was induced by the residual flux density in the rotor core. After connecting the SEIG with the back-to-back converter, $v_{gab}(t)$ gradually increased due to the reactive power $q_1(t)$ from the capacitors C_{ex}. While building the terminal voltage, the SEIG also supplied active power to the DC bus capacitor C_D, with the VSC operated as a passive rectifier. Thus, the DC bus voltage was approximately equal to the peak value of the SEIG line-to-line voltage. The VSC current $i_{sa}(t)$ rose during the build-up period and decreased to zero at the steady state. At the steady-state no-load condition, the SEIG current $i_{ga}(t)$ flowed between the SEIG and C_{ex}, as observed from $i_{sa}(t) \approx 0$. The voltage $v_{gab}(t)$ settled at the RMS value of $V_{LL} \approx 220$ V at the steady state. Note that this voltage V_{LL} depends on the C_{ex} value and the engine speed ω_m. Figure 12b shows the startup of the PWM rectifier when $v_D(t)$ increased to the reference $V_D^* = 400$ V. The voltage $v_{gab}(t)$ dropped during the transient condition because the SEIG supplied the active power $p_g(t)$ to the bus capacitance. However, the SEIG was kept excited by the reactive power $q_2(t)$ feeding back from the PWM rectifier to the SEIG.
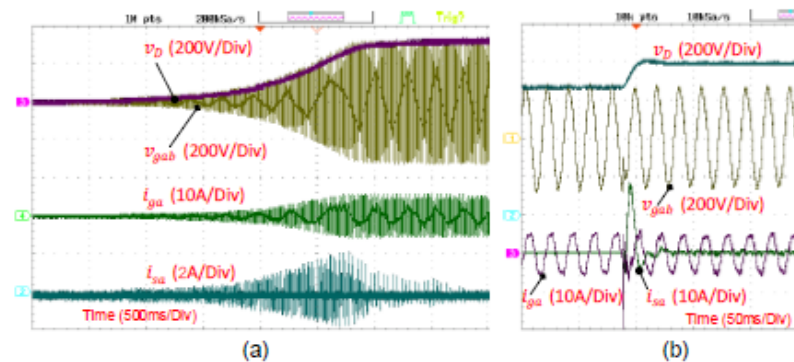
Figure 12. Transient voltage and current waveforms of the SEIG-side converter: (a) Voltage build-up period, (b) DC bus voltage start-up period.

Once the PWM rectifier had been operated, the grid-side inverter was enabled. Figure 13 shows the transient response of the grid current $i_o(t)$ when injecting a power output of 1200 W. The dq-axes current signals $i_{sd}(t)$ and $i_{sq}(t)$ of the PWM rectifier in the microcontroller-based control system were sent to 14-bit digital t0 analog converters (DACs) for monitoring on an oscilloscope. The SEIG-side control system produced the $d-$axis current $i_{sd}(t)$ to draw an active power $p_g(t)$ from the SEIG. The $q-$axis current $i_{sq}(t)$ also increased in proportion to $i_{sd}(t)$. Figure 14 displays the steady-state waveforms of the grid voltage $v_o(t)$ and current $i_o(t)$, and the SEIG voltage $v_{gab}(t)$ and current $i_{ga}(t)$ at the rated output power of 1.5 kW, where the engine speed was approximately 97π rad/s. The SEIG frequency measured 46 Hz. The SEIG current waveform was close to sinusoidal without inter-harmonic components, as analyzed in (8), due to the notch filter blocking the $2\omega_o$ component of the bus voltage. Meanwhile, the grid current waveform was near-sinusoidal because of the added harmonic controller. The effect of the bus voltage ripple on the SEIG current is illustrated in Figure 15, where the notch filter was replaced by a low-pass filter. The bus voltage loop bandwidth was tuned at 15 Hz, similar to the notch filter-based control. The changes in each SEIG current cycle indicate the presence of the inter-harmonic components, as explained in (8).
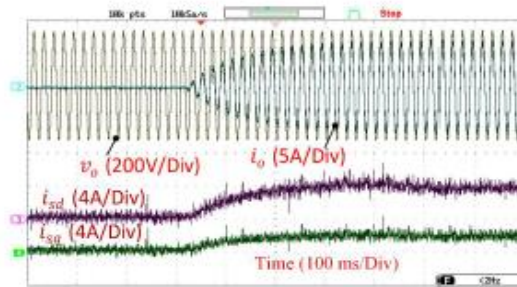
Figure 13. Transient response when injecting a power of 1200 W to the grid.
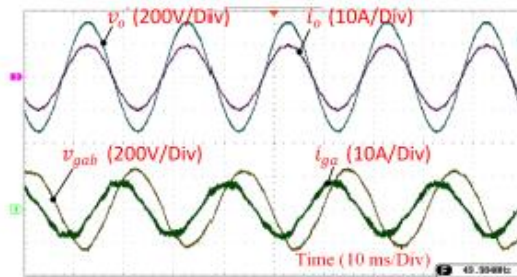
Figure 14. Steady-state waveforms of the grid voltage and current and SEIG voltage and current at the rated output power of 1.5 kW, with the notch filter-based bus voltage control.
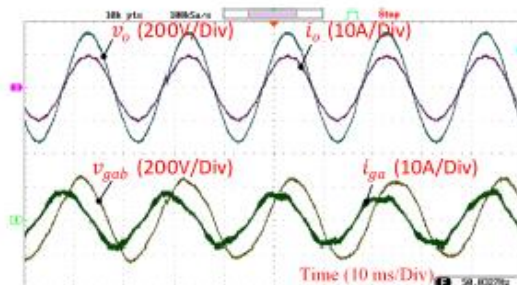
Figure 15. Steady-state waveforms of the grid voltage and current and SEIG voltage and current at the rated output power of 1.5 kW, with the low-pass filter-based bus voltage control.

The SEIG current waveform was also near-sinusoidal, with a total harmonic distortion (THD) of 2.67% at the rated power. Figure 16 depicts the grid current harmonics at the output powers of 500 W (33%), 1000 W (66%), and 1500 W (100%), normalized by the rated current of 6.75 A, which comply with the IEEE 1547 standard [47].
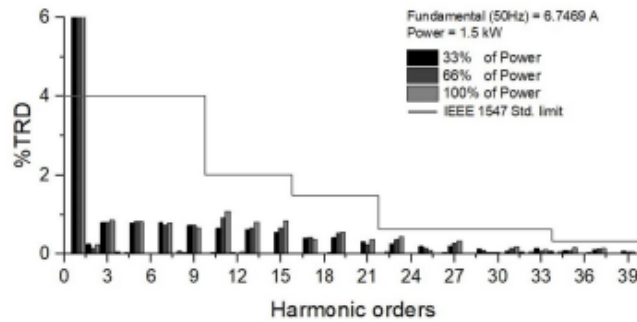
Figure 16. Output current harmonics of the grid-side inverter, normalized by the rated current, according to the IEEE 1574 standard.

Figure 17 shows the reactive power $q_2(t)$ the PWM rectifier injected to the SEIG with the output power range from 10% to 100%. The reactive power from the capacitor bank Q_1 is determined from the following:

$$Q_1 = 3 \times (V_{LL}^2 \omega_g C_{\alpha})$$ (20)
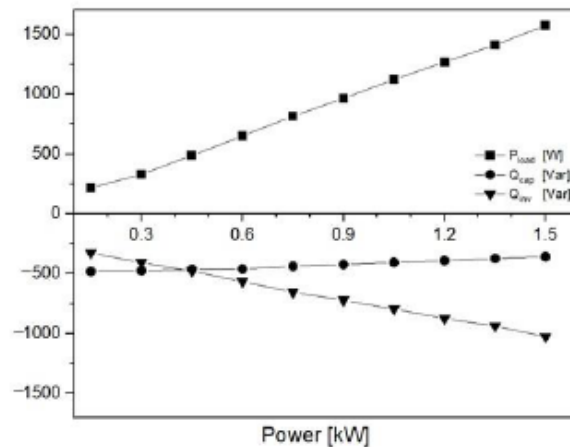
Figure 17. Reactive power and active power of the SEIG with the output power.

The reactive power Q_1 decreased with the output power due to the generator frequency reduction. The reactive power $q_2(t)$ from the PWM rectifier plays an essential role in the regulation of the SEIG voltage. Figure 18 depicts the SEIG voltage/frequency ratio, normalized by the nominal value of V_{LLB}/f_{gB}, which is close to unity over the output power range.
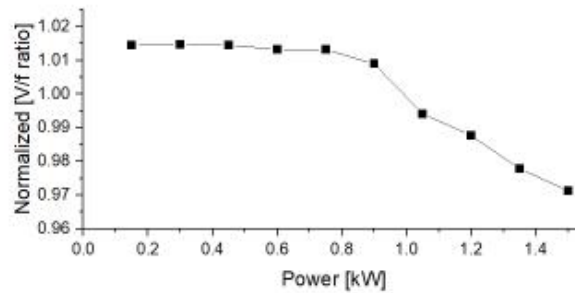
Figure 18. Normalized SEIG voltage/frequency ratio.

This mechanical frequency ω_m of the induction machine is less than the electrical frequency ω_g for operating in the motor mode and higher than ω_g for the generator mode. The slip S due to the speed difference is given as below:

$$S = \frac{\omega_g - \omega_m}{\omega_g} \tag{21}$$

Figure 19 compares ω_m and ω_g normalized by the nominal frequency $\omega_{gB} = 2\pi f_{gB}$, and slip S versus the shaft torque T_m. The mechanical frequency ω_m decreased with the increasing torque T_m, according to the engine characteristics. The SEIG-side converter drew the active power $p_g(t)$ from the SEIG, which caused the SEIG frequency ω_g to be less than the mechanical frequency ω_m. Thus, the slip S decreased with the torque in the negative region while the machine operated in the generator mode.
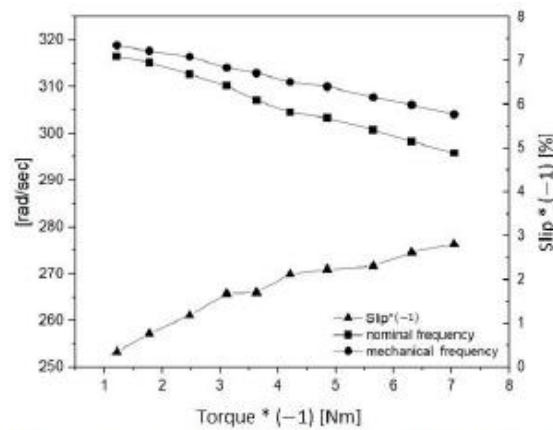
Figure 19. Mechanical, SEIG frequency and slip versus the shaft torque.

3.2. System Performance

The prototype's performance was validated with biogas at the selected area, Ta Manoa Subdistrict, in December 2021. The IRCD4 gas analyzer monitored biogas composition during the experiment, with values listed in Table 2. Note that this IRCG4 gas analyzer could not measure the moisture content of the biogas. However, it has been reported that biogas typically contains less than 1% water by volume. The engine exhaust gas was

97

monitored using an SA500 gas analyzer from Beijing Shi'An Technology (Beijing, China). The probe of the exhaust gas analyzer was cleaned before each measurement. The exhaust gas analyzer was ensured to indicate near-zero before starting the engine. The no-load speed during the field experiments was approximately 108π rad/s because the shaft speed with biogas drops, with the output power greater than with gasohol in the laboratory test. Thus, the excitation capacitors of $C_{ex} = 35$ µF were used in the field experiment in response to the higher no-load speed. For the field tests with biogas, the prototype system delivered the maximum output power of 1200 W, 80% of the rated value, due to low biogas production. Unfortunately, the pigs were young during the test period, so their manure was insufficient to produce enough biogas for the rated output power.

Table 2. Biogas composition in the field experiments.

Composition	Content
CH$_4$	68.5–70.0%
CO$_2$	30%
H$_2$S	0.14–0.24%

Figure 20 compares the engine shaft speed fueled by gasohol and biogas. The engine speed with biogas dropped rapidly, with the output power greater than 70% of the rated power. It was found during the field experiments that the SEIG lost excitation when the output power was greater than 80% of the rated value. Meanwhile, the engine with gasohol delivered the output power smoothly. However, the unstable biogas supply during the experiment and the smaller energy density of biogas itself derated the prototype output power. Figure 21 shows the biogas consumption with the output power at 21 °C and 101.325 kPa, which was obtained from the thermal mass flowmeter. This biogas flowrate and the methene content in Table 2 was used to calculate the engine input power.
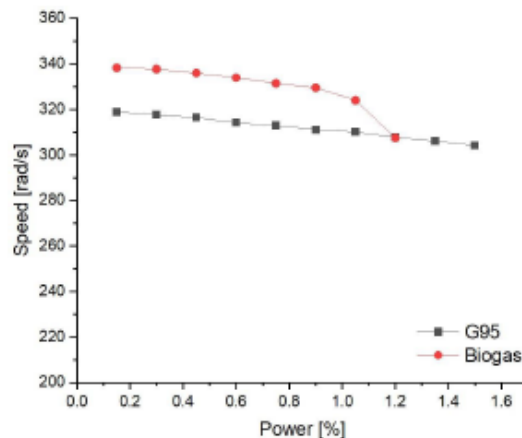
Figure 20. Engine shaft speed with the output power.

Figure 22 compares the engine's efficiency, SEIG, back-to-back converter, and system with biogas and gasohol. The engine plays a vital role in system efficiency. The engine efficiency with biogas was smaller than with gasohol. At the output power of 80%, the engine efficiency was approximately 14%, while that with gasohol was 18%. The engine efficiency can be improved if the biogas supply were to be sufficient for higher power operation. The SEIG and back-to-back converter had an efficiency greater than 70% and

90% for the output power above 50%. The system efficiency with biogas was approximately 10.7% at the output power of 80%. The system efficiency with biogas is expected to be about 13% at the rated power, estimated from the system efficiency with gasohol.
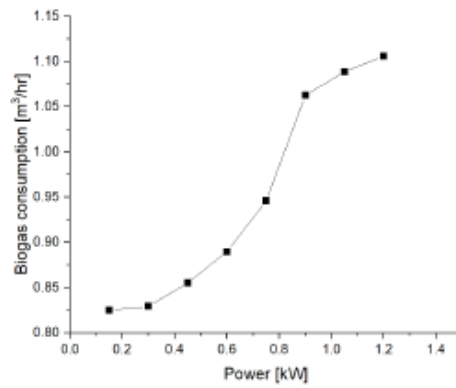
Figure 21. Biogas consumption with the output power.
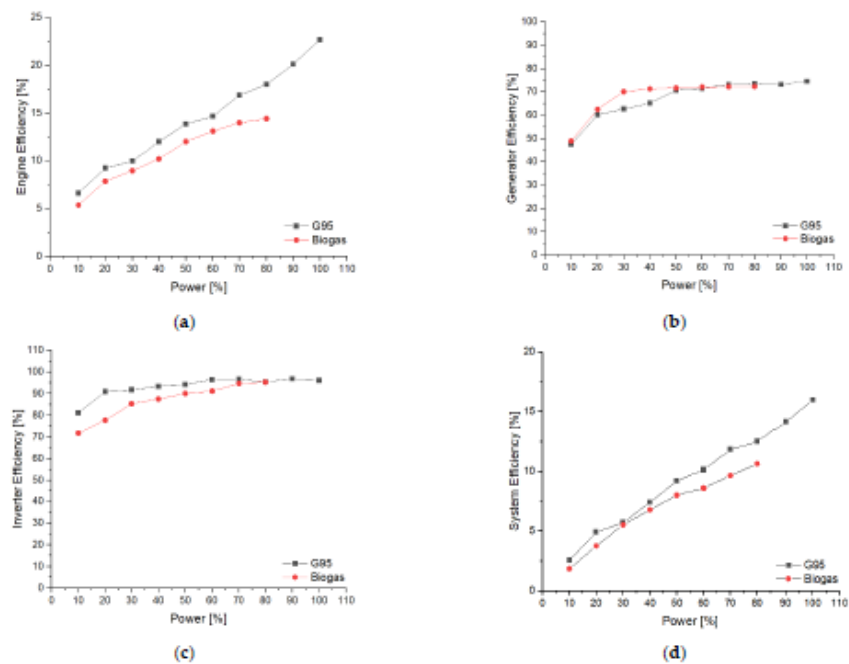
Figure 22. Efficiency of the prototype generation system: (a) engine, (b) SEIG, (c) back-to-back converter, and (d) system.

Figure 23 compares NO_x and CO emissions of the exhaust gas. The NO_x emission with biogas is far less than that with gasohol. The NO_x emission of the biogas-fed system was less than 50 ppm at 80% of the rated output power, thanks to the purification process using the $Fe(OH)_3$ absorbent granules. Meanwhile, the CO emission of the biogas-fed engine decreased with the output power, with the CO emission being lower than 400 ppm at 80% of the rated output power. This is believed to be due to a complete combustion process. On the other hand, the CO emission with gasohol was 2000 ppm for every output power level, which was the maximum measurable value of the exhaust gas analyzer. Thus, the actual CO emission was greater than 2000 ppm.
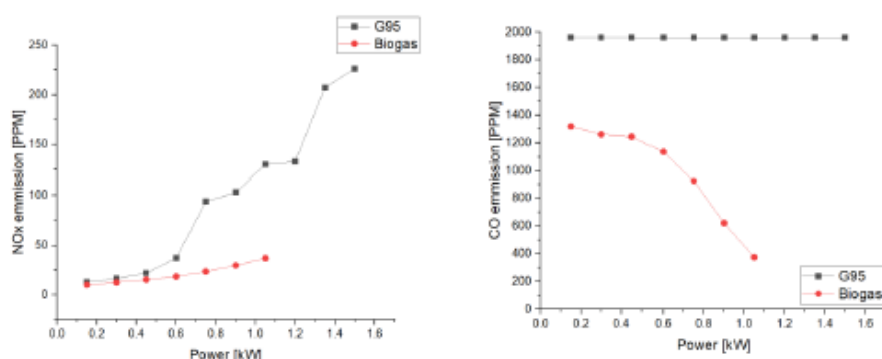
Figure 23. NO_x and CO emissions with the output power.

The higher amount of NO_x and CO emissions for the gasohol fuel resulted from incomplete combustion, which agrees with the report in [16] performed on the same GX200 engine. Meanwhile, the brake thermal efficiency of the engine with biogas (CH_4 of 80%) in [16] was slightly greater than unleaded gasoline, which contrasts with the results in this study. This is believed to be because the biogas in this study contained CH_4 concentration of approximately 70%.

4. Suitability and Economic Analysis

The proposed biogas generation system was technically proven. This section analyzes the possible applications and economic feasibility of the system.

4.1. Suitability of the Proposed Biogas Power Generation System

Let us assume that the prototype system is operated at 1.2 kW for 8 h from 5.30–8.30 am and 5.00–8.00 pm to support the peak load of the local grid. According to the biogas consumption rate of 1.106 m^3/h at 1.2 kW in Figure 22, this power production requires biogas input of 8.85 m^3 daily. It was reported in [48] that a mature pig excretes manure at a rate of 2 kg/day, which produces 0.26 m^3 of biogas. Therefore, a farm should have at least 34 pigs to create a stable biogas supply. In practice, there are 100–700 pigs on the pig farms in Ta Manoa subdistrict. Thus, installing the proposed prototype system on each farm is feasible. It is estimated that the output power can be scaled up to 5 kW with the largest 390 cc engine in this GX series and a 7.5 kW induction machine. The spark–ignition engine selected in this study is widely used in agricultural equipment such as water pumps and sprayers. People in the community are familiar with the engine. Therefore, maintenance of the engine can be carried out locally.

However, this biogas power generation system requires more operation and mainte-nance compared with photovoltaic power generation. This issue can be a barrier to the

wide adaptation of this biogas power generation. Therefore, energy and environmental policies are the key drivers of this biogas power generation scheme for small communities.

4.2. Economic Viability

This analysis covers the biogas power generation system, excluding the anaerobic digester and purification. Biogas is considered a by-product of the waste management system. Table 3 summarizes the capital and annual operating costs and the salvage values of the system components. The operating cost and salvage value were estimated during the installation. Maintenance of the engine is the primary operating cost. In this assumption, the system lifetime is five years. The engine is set to operate for 8 h daily, so the total operating time is 14,600 h. Meanwhile, a biogas-fueled spark–ignition engine can be operated for up to 60,000 h [49]. The life-cycle cost (LCC) for the five years is USD 1046 with an interest rate of 7%. Note that the power converter and SEIG can be overhauled after the project life and reused in the new project.

Table 3. Break-down of costs of the proposed SEIG-based biogas power generation system.

Parts	Capital Cost	Annual Operating Cost	Salvage Value
Engine with biogas modification	USD 260	USD 35	-
Generator (SEIG)	USD 150	-	USD 75
Power converter	USD 450	-	USD 200
Housing and piping	USD 140	USD 7	-
Total	USD 1000	USD 42	USD 270

Let us assume there is a 10% system unavailability due to maintenance and low biogas production. An energy yield per year at 1.2 kW is then given as shown:

$$1.2 \text{ kW} \times 8 \text{ hours} \times 365 \text{ days} \times 0.9 = 3153 \text{ kWh} \tag{22}$$

Each year's revenue is estimated to be USD 378.36 with a retail electricity price of USD 0.12. Thus, the payback period will be 2.8 years. Therefore, the levelized cost of electricity (LCOE) for the whole project lifetime is 0.07 US$/kWh. Note that the LCOE of 0.07 US$/kWh does not include the biogas cost, a byproduct of the waste management system. The system efficiency must be improved to keep the LCOE viable if purchasing biogas.

A 3 kW photovoltaic power (PV) generation system was selected to compare with the biogas power generation system in this study. In Thailand, a specific annual energy yield of 1400 kWh/kWp/year was estimated using the PVsyst software. The installation cost for a 3 kW PV system is approximately USD 3600, with an annual maintenance cost of 0.5%. The salvage value is estimated to be zero. The project's life is 25 years. Table 4 compares the economic viability analysis of the biogas power generation with a 3 kW PV system. Although the LCOE of the biogas system is slightly higher than that of the PV system, the main benefit of the biogas in this study is a stable and dispatchable source.

Table 4. Economic viability of biogas power generation and a 3 kW photovoltaic system.

Indicators	Biogas in This Study	3 kW PV
Energy yield	3153 kWh/year	4200 kWh/year
Project period	5 years	25 years
LCC	USD 1046	USD 4738
Payback period	2.8 years	9.4 years
LCOE	USD 0.07/kWh	USD 0.05/kWh

5. Conclusions

A 196 cc 4-stroke single-cylinder ignition engine was fueled by biogas from pig manure using a gas conversion kit. The engine drove a 2-pole 2.2 kW squirrel-cage inductor motor,

operated as a self-excited induction generator. We developed a back-to-back converter for generator control and integration with a 220 V 50 Hz single-phase network. The generator-side converter employed a three-phase PWM rectifier to transfer active power to the grid-side converter and supply reactive power back to the generator for voltage regulation. The grid-side converter adopted an LCL-filtered voltage source inverter with multi-frequency unbalanced synchronous reference frame control, resulting in an injected output current which complied with the IEEE 1547 standard. Meanwhile, the notch filter-based bus voltage control on the generator side effectively mitigated the inter-harmonic components in the generator current caused by the oscillating power from the grid-side converter.

The prototype power generation system was validated with biogas from a swine farm in Ta Manoa subdistrict, Lopburi, Thailand. The system delivered a maximum power of 1.2 kW with a thermal efficiency of 10.7%. If the system is operated at the output power of 1.2 kW for 8 h per day, the prototype is suitable for a farm with at least 34 pigs. The proposed system has a life-cycle cost of USD 1046 for 5 years. The levelized cost of electricity was estimated to be USD 0.07/kWh, with a payback period of 2.76 years. The advantages of the proposed biogas power generation system can be summarized as follows:

(1) Low investment cost;
(2) Spark–ignition engines and induction machines are manufactured in Thailand and are widely available;
(3) The system is easy to operate, and maintenance of the engines can be carried out in the community;
(4) The system is a dispatchable renewable source that can be used for grid support;
(5) Near-sinusoidal generator and output currents impose a low loss on the generator.

Author Contributions: Conceptualization, S.S.; methodology, P.T.; software, P.T.; validation, P.T., T.K. (Tanakorn Kaewchum), T.P. and W.W.; formal analysis, P.T., S.S. and T.S.; investigation, P.T., S.S. and T.S.; resources, S.S. and P.M.; data curation, T.S.; writing—original draft preparation, P.T.; writing—review and editing, S.S.; visualization, S.B.; supervision, S.S.; project administration, P.M. and B.P.; funding acquisition, T.K. (Tanongkiat Kiatsiriroat). All authors have read and agreed to the published version of the manuscript.

Institutional Review Board Statement: Not applicable.

Informed Consent Statement: Not applicable.

Data Availability Statement: Not applicable.

Conflicts of Interest: The authors declare no conflict of interest.

References

1. Obaideen, K.; Abdelkareem, M.A.; Wilberforce, T.; Elsaid, K.; Sayed, E.T.; Maghrabie, H.M.; Olabi, A. Biogas role in achievement of the sustainable development goals: Evaluation, Challenges, and Guidelines. *J. Taiwan Inst. Chem. Eng.* **2022**, *131*, 104207. [CrossRef]
2. Czubaszek, R.; Wysocka-Czubaszek, A.; Wichtmann, W.; Banaszuk, P. Specific Methane Yield of Wetland Biomass in Dry and Wet Fermentation Technologies. *Energies* **2021**, *14*, 8373. [CrossRef]
3. Tauber, J.; Ramsbacher, A.; Svardal, K.; Krampe, J. Energetic Potential for Biological Methanation in Anaerobic Sewage Sludge Digesters in Austria. *Energies* **2021**, *14*, 6618. [CrossRef]
4. Seruga, P.; Krzywonos, M.; Boer, E.D.; Niedźwiecki, A.; Urbanowska, A.; Pawlak-Kruczek, H. Anaerobic Digestion as a Component of Circular Bioeconomy—Case Study Approach. *Energies* **2023**, *16*, 140.

5. Ingale, G.U.; Kwon, H.-M.; Jeong, S.; Park, D.; Kim, W.; Bang, B.; Lim, Y.-I.; Kim, S.W.; Kang, Y.-B.; Mun, J.; et al. Assessment of Greenhouse Gas Emissions from Hydrogen Production Processes: Turquoise Hydrogen vs. Steam Methane Reforming. *Energies* **2022**, *15*, 8679. [CrossRef]
6. Athanasiou, C.; Drosakis, C.; Booto, G.K.; Elmasides, C. Economic Feasibility of Power/Heat Cogeneration by Biogas–Solid Oxide Fuel Cell (SOFC) Integrated Systems. *Energies* **2023**, *16*, 404.
7. Chang, C.C.; Do, M.V.; Hsu, W.L.; Liu, B.L.; Chang, C.Y.; Chen, Y.H.; Yuan, M.-H.; Lin, C.-F.; Yu, C.-P.; Chen, Y.H.; et al. A case study on the electricity generation using a micro gas turbine fuelled by biogas from a sewage treatment plant. *Energies* **2019**, *12*, 2424. [CrossRef]
8. Xiao, G.; Yang, T.; Liu, H.; Ni, D.; Ferrari, M.L.; Li, M.; Luo, Z.; Cen, K.; Ni, M. Recuperators for micro gas turbines: A review. *Appl. Energy* **2017**, *197*, 83–99. [CrossRef]
9. Yanmar Holdings. Cogeneration Systems—CP Series (Bio Gas). 2023. Available online: https://www.yanmar.com/en_th/energy/cogeneration_systems/biogas/ (accessed on 16 June 2023).
10. Caterpillar. Gas Generator Sets G3520C. 2023. Available online: https://www.cat.com/en_US/products/new/power-systems/electric-power/gas-generator-sets/18483554.html# (accessed on 16 June 2023).
11. Verma, S.; Das, L.M.; Kaushik, S.C. Effects of varying composition of biogas on performance and emission characteristics of compression ignition engine using exergy analysis. *Energy Convers. Manag.* **2017**, *138*, 346–359. [CrossRef]
12. Homdoung, N.; Tippayawong, N.; Dussadee, N. Performance and emissions of a modified small engine operated on producer gas. *Energy Convers. Manag.* **2015**, *94*, 286–292. [CrossRef]
13. Yingjian, L.; Qi, Q.; Xiangzhu, H.; Jiezhi, L. Energy balance and efficiency analysis for power generation in internal combustion engine sets using biogas. *Sustain. Energy Technol. Assess.* **2014**, *6*, 25–33. [CrossRef]
14. Capaldi, P.; Daliento, A.; Rizzo, R. An innovative 10 kW microcogenerator suitable for off grid application and fed with syngas or biogas. In Proceedings of the Universities Power Engineering Conference, Cluj-Napoca, Romania, 2–5 September 2014.
15. Da Costa, R.B.R.; Valle, R.M.; Hernández, J.J.; Malaquias, A.C.T.; Coronado, C.J.; Pujatti, F.J.P. Experimental investigation on the potential of biogas/ethanol dual-fuel spark-ignition engine for power generation: Combustion, performance and pollutant emission analysis. *Appl. Energy* **2020**, *261*, 114438. [CrossRef]
16. Karakitie, E.D.; Aralu, C.E.; Fadare, A.D. Performance charateristics of a conventional spark ignition petrol engine powered by biogas. *Fuel Commun.* **2022**, *10*, 100032. [CrossRef]
17. Bash, M.; Pekaret, S.; Sudhoff, S.; Whitmore, J.; Fratzen, M. A comparison of permanent magnet and wound rotor synchronous machines for portable power generation. In Proceedings of the 2010 Power and Energy Conference at Illinois (PECI), Urbana, IL, USA, 12–13 February 2010.
18. Wang, L.; Lin, P. Analysis of a Commercial Biogas Generation System Using a Gas Engine–Induction Generator Set. *IEEE Trans. Energy Convers.* **2009**, *24*, 230–239. [CrossRef]
19. Bellini, A.; Franceschini, G.; Lorenzani, E.; Tassoni, C.; Tomaiuolo, M. Field Oriented Control of Self-Excited Induction Generator for Distributed Cogeneration Plants. In Proceedings of the 41st IEEE Industry Applications Conference, Tampa, FL, USA, 8–12 October 2006.
20. Klima, J. Stand Alone Bio-Gas Power Plants with Induction Generator and PWM Voltage Source Inverter. *IFAC Proc. Vol.* **1997**, *30*, 137–142. [CrossRef]
21. Singh, G.K. Self-excited induction generator research—A survey. *Electr. Power Syst. Res.* **2004**, *69*, 107–114. [CrossRef]
22. Krishna, V.M.; Sandeep, V.; Murthy, S.; Yadlapati, K. Experimental investigation on performance comparison of self excited induction generator and permanent magnet synchronous generator for small scale renewable energy applications. *Renew. Energy* **2022**, *195*, 431–441. [CrossRef]
23. Calgan, H.; Demirtas, M. A robust LQR-FOPIλDμ controller design for output voltage regulation of stand-alone self-excited induction generator. *Electr. Power Syst. Res.* **2021**, *196*, 107175. [CrossRef]
24. Sowmmiya, U.; Uma, G. Control and maximum power tracking operation of hybrid excited variable speed induction generator. *Electr. Power Syst. Res.* **2017**, *143*, 771–781.
25. Capelo, B.; Pérez-Sánchez, M.; Fernandes, J.F.; Ramos, H.M.; López-Jiménez, P.A.; Branco, P.C. Electrical behaviour of the pump working as turbine in off grid operation. *Appl. Energy* **2017**, *208*, 302–311. [CrossRef]
26. Chilipi, R.R.; Singh, B.; Murthy, S.S. Performance of a Self-Excited Induction Generator With DSTATCOM-DTC Drive-Based Voltage and Frequency Controller. *Energy Conversion. IEEE Trans.* **2014**, *29*, 545–557.
27. Marra, E.G.; Pomilio, J.A. Induction-generator-based system providing regulated voltage with constant frequency. *IEEE Trans. Ind. Electron.* **2000**, *47*, 908–914. [CrossRef]
28. Scherer, L.G.; Tischer, C.B.; de Camargo, R.F. Power rating reduction of distribution static synchronous compensator for voltage and frequency regulation of stand-alone self-excited induction generator. *Electr. Power Syst. Res.* **2017**, *149*, 198–209. [CrossRef]
29. Chauhan, P.J.; Chatterjee, J.K.; Bhere, H.; Perumal, B.V.; Sarkar, D. Synchronized Operation of DSP-Based Generalized Impedance Controller With Variable-Speed Isolated SEIG for Novel Voltage and Frequency Control. *IEEE Trans. Ind. Appl.* **2015**, *51*, 1845–1854. [CrossRef]
30. Ayodele, T.R.; Ogunjuyigbe, A.S.O.; Adetokun, B.B. Optimal capacitance selection for a wind-driven self-excited reluctance generator under varying wind speed and load conditions. *Appl. Energy* **2017**, *190*, 339–353. [CrossRef]

31. Thomsen, B.; Guerrero, J.M.; Thøgersen, P.B. Faroe islands wind-powered space heating microgrid using self-excited 220-kW induction generator. *IEEE Trans. Sustain. Energy* **2014**, *5*, 1361–1366. [CrossRef]
32. Ion, C.P.; Marinescu, C. Three-phase induction generators for single-phase power generation: An overview. *Renew. Sustain. Energy Rev.* **2013**, *22*, 73–80. [CrossRef]
33. Honda. GX120/160/200. 2023. Available online: https://engines.honda.com/models/model-detail/mid-gx#Features (accessed on 16 June 2023).
34. Senthil Kumar, S.; Kumaresan, N.; Subbiah, M. Analysis and control of capacitor-excited induction generators connected to a micro-grid through power electronic converters. *Generation, Transmission & Distribution. IET* **2015**, *9*, 911–920.
35. Singh, B.; Niwas, R. Performance of synchronous reluctance generator for DG set based standalone supply system. *Electr. Power Syst. Res.* **2016**, *133*, 93–103. [CrossRef]
36. Braga, A.; Rezek, A.; Silva, V.; Viana, A.; Bortoni, E.; Sanchez, W.; Ribeiro, P. Isolated induction generator in a rural Brazilian area: Field performance tests. *Renew. Energy* **2015**, *83*, 1352–1361. [CrossRef]
37. Somkun, S. High performance current control of single-phase grid-connected converter with harmonic mitigation, power extraction and frequency adaptation capabilities. *IET Power Electron.* **2021**, *14*, 352–372. [CrossRef]
38. Monfared, M.; Golestan, S.; Guerrero, J.M. Analysis, design, and experimental verification of a synchronous reference frame voltage control for single-phase inverters. *IEEE Trans. Ind. Electron.* **2014**, *61*, 258–269. [CrossRef]
39. Somkun, S. Unbalanced synchronous reference frame control of singe-phase stand-alone inverter. *Int. J. Electr. Power Energy Syst.* **2019**, *107*, 332–343. [CrossRef]
40. Somkun, S.; Chunkag, V. Unified unbalanced synchronous reference frame current control for single-phase grid-connected voltage-source converters. *IEEE Trans. Ind. Electron.* **2016**, *63*, 5425–5436. [CrossRef]
41. Golestan, S.; Monfared, M.; Freijedo, F.D.; Guerrero, J.M. Dynamics assessment of advanced single-phase PLL structures. *IEEE Trans. Ind. Electron.* **2013**, *60*, 2167–2177. [CrossRef]
42. Wang, J.; Yan, J.D.; Jiang, L.; Zou, J. Delay-dependent stability of single-loop controlled grid-connected inverters with LCL filters. *IEEE Trans. Power Electron.* **2016**, *31*, 743–757. [CrossRef]
43. Holmes, D.G.; Lipo, T.A.; McGrath, B.P.; Kong, W.Y. Optimized design of stationary frame three phase AC current regulators. *IEEE Trans. Power Electron.* **2009**, *24*, 2417–2426. [CrossRef]
44. Sangwongwanich, A.; Abdelhakim, A.; Yang, Y.; Zhou, K. Chapter 6—Control of Single-Phase and Three-Phase DC/AC Converters. In *Control of Power Electronic Converters and Systems*; Blaabjerg, F., Ed.; Academic Press: Cambridge, MA, USA, 2018; pp. 153–173.
45. Sedpho, S. *Community Biogas from Swine Farms Phase 3 at Thamanao Sub-District, Chaibadan District, Lopburi Province, Thailand*; Thailand Voluntary Emission Reduction Program; Tha Manao Subdistrict Administrative Organization: Lopburi, Thailand, 2020.
46. Pinate, W.; Dangphonthong, D.; Sirirach, S.; Sukkhon, S. Removal of hydrogen sulfide (H_2S) from biogas for the community in the province of Maha Sarakham. *J. Phys. Conf. Ser.* **2017**, *901*, 012049. [CrossRef]
47. 1547-2018; IEEE Standard for Interconnection and Interoperability of Distributed Energy Resources with Associated Electric Power Systems Interfaces. Revision of IEEE Std 1547–2003; IEEE Standards Coordinating Committee: New York, NY, USA, 2018; pp. 1–138.
48. Khotmanee, S.; Pinsopon, U. A Study on Biogas Production Potential in Thailand 2019. In Proceedings of the 7th International Conference on Engineering, Applied Sciences and Technology (ICEAST), Bangkok, Thailand, 1–3 April 2021.
49. Kaparaju, P.; Rintala, J. 17–Generation of heat and power from biogas for stationary applications: Boilers, gas engines and turbines, combined heat and power (CHP) plants and fuel cells. In *The Biogas Handbook*; Wellinger, A., Murphy, J., Baxter, D., Eds.; Woodhead Publishing: Sawston, UK, 2013; pp. 404–427.

Research Article

EASR

Engineering and Applied Science Research

https://www.tci-thaijo.org/index.php/easr/index

Published by the Faculty of Engineering, Khon Kaen University, Thailand

Biogas-powered small power generation system designed for the agricultural sector to support the BCG model in Thailand

Panupon Trairat*[1], Sakda Somkun[1], Tanakorn Kaewchum[1], Tawat Suriwong[1], Pisit Maneechot[1] and Tanongkiat Kiatsiriroat[2]

[1]School of Renewable Energy and Smart Grid Technology (SGtech), Naresuan University, Phitsanulok, Thailand
[2]Department of Mechanical Engineering, Faculty of Engineering, Chiang Mai University, Chiang Mai, Thailand

Abstract

This study presents the design of a small grid-connected power generation unit for farming systems to support the Bio-Circular-Green Economic Model (BCG) in Thailand. We focus on using the remaining agriculture waste resources to be reused according to the circular economy in the BCG model. Biogas was used as the primary fuel for an internal combustion engine, with gasoline and LPG as the immediate emergency reserves. We have integrated an engine to transmit power to a self-excited induction generator and designed a grid-connected inverter control strategy based on PQ control for the power conversion of the system by using digital signal processing. Using interface-based Internet of Things, devices can be wirelessly connected for control and logging data via a dashboard application.

Keywords: Biogas, Self-Excited Induction Generator, Internal combustion engine, BCG model, Circular economy

1. Introduction

Thailand has the majority of its people engaged in agriculture: annual crops such as rice, sugar cane, corn, cassava, etc., and small livestock farming such as pigs, chickens, fish, cows, etc., and so is considered an agricultural society. But the farm production process is still at a low level. Due to the small number of innovations related to agriculture, the Thai government supports innovation to improve the quality and quantity of agricultural production and has presented a Bio-Circular-Green Economic Model (BCG) model as a strategy to create sustainability and equality for the economy, society, and environment [1-3]. This model focuses on applying science, technology, and innovation to transform a comparative advantage in biodiversity and culture into a competitive one. Its benefits are concentrated in four strategic sectors: 1) Agriculture and Food, 2) Health and Medicine, 3) Energy, Materials, and Biochemistry, and 4) Tourism and Creative Economy. The BCG model consists of three leading economies: the Bio-Economy (B) system focuses on the cost-effective use of biological resources, linking with the Circular Economy (C) that implements the reuse of various materials as much as possible, and both these economies are within the Green Economy (G) system which aims to solve pollution problems to sustainably reduce the impact on the planet [4-6], as shown in Figure 1. Furthermore, the BCG model will drive smart practices for Agriculture 4.0 to make agriculture in Thailand more sustainable [3-6].

According to the chapters in the 2021-2027 BCG Action Plan [1], two main issues for development in the agriculture and energy sectors are pushing for renewable energy. Biogas is an engaging alternative energy for recycling waste from agricultural and industry in accordance with the circular economy based on the BCG model [1, 7]. When we surveyed Thailand's agricultural and livestock sectors, there was a potential for biogas fuel production from agricultural waste or animal manure [8-10], which have been used in terms of burning fuel for cooking. Biogas is an attractive fuel for power generation but is not widespread. Supposing it can generate electricity for agriculture, it will increase self-sufficiency by managing agricultural and household electricity use. Biogas-fueled power generation can respond to three key points of the BCG model. This can be classified, for the sake of clarity, as follows: 1) Bio-economy: take biotechnology and biodiversity as a driver. 2) Circular economy: using waste materials to generate alternative energy. 3) Green economy: environmentally friendly and sustainable development.

This research aims to design a small-size grid-connected power generation integrated with a Self-Excited Induction Generator (SIEG) and an internal combustion engine (IC engine) using biogas as fuel. The system was developed focusing on using locally produced equipment that is generally available, resulting in simple maintenance. We selected an IC engine to be the prime mover for the generator. Since farmers use it daily for farm use, such as water pumping and filling, it can be applied in another application without complicated modifications to be used with a biogas fuel. We designed a back-to-back converter with a capacitor bank to control power conversion from an internal combustion (IC) engine to an SEIG. We connected it to the grid with a DC-link size of 400 V, with the maximum output power from the converter being 1.5 kW. The system to measure, process, and communicate was added through an IoT system displayed on a mobile application dashboard to manage the electricity used. The experimental design was split into two tests: 1) Laboratory testing of the effectiveness of the SEIG, the inverter, and the control system. The test system was connected to the

grid at a power rating of 1.5 kW, and the system was run on gasoline 95 fuel. 2) The engine's performance when using three different types of fuel (95-octane gasoline, LPG, and biogas) was tested, including greenhouse gas emissions.

2. Closed-loop circular economy systems for the agricultural sector

The circular economy for agriculture refers to an approach that aims to create a closed-loop system within the agricultural sector, minimizing waste, maximizing resource efficiency, and promoting sustainable practices. [4-7]

This concept draws its inspiration from natural ecosystems, where waste from one process becomes a valuable input for another, creating a closed-loop system that maximizes resource utilization and reduces environmental impact. Here is how it can be applied to agriculture:

1) Waste Reduction and Valorization:

- Implement composting and anaerobic digestion to convert organic waste (crop residues, food scraps) into nutrient-rich compost and biogas.

- Recycle agricultural byproducts and residues as feedstock for bioenergy production or other value-added products.

2) Closed-loop Systems:

- Integrate livestock farming and crop production, where animal waste becomes a nutrient source for crops and crop residues become feed for animals.

- Creating integrated farming systems where livestock waste is used as a resource rather than a pollutant. For example, using manure as fertilizer or converting it into biogas for the sake of producing energy.

Figure 1 shows the closed-loop circular economy systems for the agricultural sector. The red arrow closed-loop demonstrates the purpose of this study. It can be briefly explained as follows: Agricultural and livestock waste is fermented in tanks by an anaerobic digestion process. The resulting product is the required methane (CH4) gas and other gas components. The remainder from the completion of this process will be organic fertilizer, which will be used as plant food. The resulting methane gas is converted into heat and electrical energy.

Thailand has always used a closed-loop system to reduce waste by producing biogas from agricultural and livestock waste and occasionally using it as fuel for burning. However, electricity power generation from biogas was still not widely used. Producing electricity from biogas will contribute to this system's completion and can lead to a more resilient, efficient, and sustainable energy system that balances economic prosperity with environmental and social well-being in Thailand.
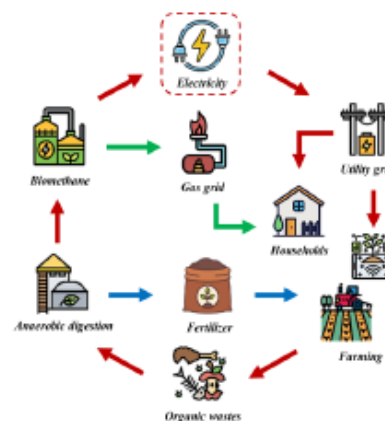

Figure 1 Closed-loop circular economy system for the agricultural sector [4-7]

3. Biogas production and potential in Thailand

Biogas production is a sustainable and renewable energy generation process that involves the conversion of organic materials into biogas through the process of anaerobic digestion. Biogas primarily consists of methane (CH4) and carbon dioxide (CO2), along with trace amounts of other gases like hydrogen sulfide (H2S) and water vapor. It can be used as a source of energy for various applications, including generating electricity, heating, and even as a vehicle fuel [8-10].

Here are the key steps involved in biogas production:

1) **Feedstock Selection**: Organic materials, known as feedstock, are used as the raw materials for biogas production. Common feedstock sources include animal manure, agricultural residues, food waste, sewage sludge, and energy crops (such as maize or grass).

2) **Preparation**: The feedstock is collected and prepared for the anaerobic digestion process. This may involve shredding, chopping, or other mechanical processes to reduce particle size and increase the surface area for microbial activity.

3) **Anaerobic Digestion**: Anaerobic digestion is the core process, in which microorganisms break down the organic matter in the absence of oxygen. This occurs in a sealed, oxygen-free digester tank. It has four main stages:

- **Hydrolysis**: Complex organic materials are broken down into simpler compounds.
- **Acidogenesis**: Acid-forming bacteria convert the simpler compounds into volatile fatty acids.

- **Acetogenesis**: Acetic acid is formed from the volatile fatty acids.
- **Methanogenesis**: Methanogenic bacteria convert the acetic acid and other intermediates into methane and carbon dioxide.
4) **Gas Collection**: The biogas produced during the anaerobic digestion process is collected at the top of the digester tank.
5) **Gas Storage and Upgrading**: Biogas may require further treatment to remove impurities such as hydrogen sulfide (H2S) and moisture. Additionally, it can be stored in tanks or used directly for various applications. In some cases, it can also be upgraded to biomethane, which is a purified form of biogas with a higher methane content suitable for injection into natural gas pipelines or use as a transportation fuel.
6) **Biogas Utilization**: Biogas can be used for a wide range of applications, including:
- **Electricity Generation**: Biogas can be used in gas engines or turbines to generate electricity.
- **Heat Production**: It can be used for heating purposes in homes, industries, or for district heating.
- **Vehicle Fuel**: When upgraded to biomethane, it can be used as a clean-burning fuel for vehicles.
- **Cooking and Lighting**: In some regions, biogas is used for cooking and lighting in households.

Biogas production offers several environmental and economic benefits. It helps to manage organic waste, reduce greenhouse gas emissions, and provides a renewable source of energy. Additionally, it can be integrated into sustainable agricultural and waste management practices, contributing to a circular economy. However, the success of biogas production depends on factors like feedstock quality, digester design, and operational management.

Khotmanee and Pinsopon [8] studied the potential for biogas production in Thailand. By surveying data for three sectors, industrial plants, agricultural plants, and livestock in 2019, it was found that Thailand has the potential to produce a total of 22826.79 million cubic meters per year, divided into industrial plants at 7521.48 million m³ per year, agricultural plants at 14479.01 million m³ per year, and livestock at 826.30 million m³ per year. More details are shown in Table 1.

Table 1 Potential biogas production in Thailand 2019 [8]

Biogas Source	Production potential (million m³/years)	Productivity (million m³/years)	Remaining (million m³/years)
Industrial plants	7,521.48	747.45	6774.03
Livestock	826.30	68.61	757.66
Agricultural	1,4479.01	-	14,479.01
Total	22,826.79	816.06	22,010.70

For this research, only the agriculture and livestock sectors were studied. We therefore show the rates of waste-to-biogas production in these two sectors according to the type of agricultural plants and livestock farms found in Thailand, as shown in Tables 2 and 3 [8], [10].

Table 2 Livestock biogas production rate [8]

Types	Manure rate per day (kg/animal)	Manure collected (%)	Evaporation Rate of Solids (%)	Biogas Production Rate (m3/kg(solids))
1. Beef cattle	5.00	50	13.37	0.307
2. Dairy Cattle	15.00	80	13.37	0.307
3. Breeder Pigs	2.00	80	24.84	0.217
4. Piglets	0.50	80	24.84	0.217
5. Fattening Pigs	1.20	80	24.84	0.217
6. Chickens	0.03	80	23.34	0.242

Table 3 Agricultural waste biogas production rate [8]

Type	Waste	Ratio of Waste to product mass (%)	Waste Unused Percentage (%)	Biogas production rate (L/kg(dry))	Dry Material to Raw Material (%)
1. Rice	Straw	29.37	39.40	162 (Fresh)	-
2. Corn	Trunk	43.52	73.71	250	70
	Leaves	30.97	100	225	90
	Stubble	21.26	73.64	344	90
3. Sugarcane	Leaves and Shoots	39.51	93.24	262	70
4. Cassava	Stems and Leaves	28.93	14.87	274	65
	Rhizome	17.12	90.25	141	65

4. Materials and methods

In this study, an SIEG) and an IC engine using biogas as fuel are integrated to create a small grid-connected power generation system. The system's development was centered on utilizing widely accessible, locally produced equipment, which makes maintenance easy. We chose the generator's IC engine as the prime mover. Since it is often used by farmers for farming purposes, such as water pumping and filling, it can be utilized in another application with simple adjustments to be used with biogas fuel. To manage power conversion from an IC engine to a SEIG, we devised a back-to-back converter with a capacitor bank. A grid-connected inverter with a controller embedded inside was developed to power conversion and synchronize power to the grid, and it can be monitored and controlled via a smartphone application, as shown in Figure 2.
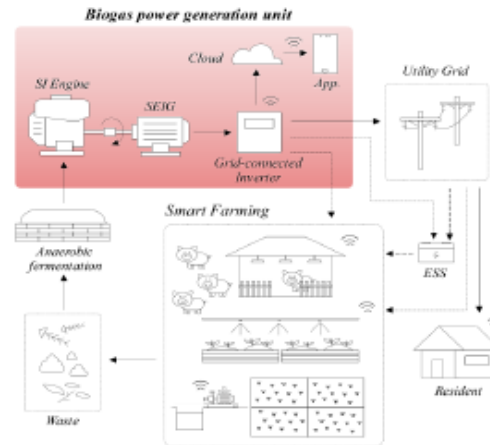
Figure 2 Proposed biogas power generation unit system

4.1 Internal combustion engine selection and modification

Gasoline-powered IC engines are suitable for the direct use of biogas [11-13]. The gas hose is installed in the carburetor area in a position above the accelerator by connecting the biogas pipe. A valve is installed outside to control the amount of biogas sent to the combustion chamber, as shown in Figure 3. This modification of the engine from the original carburetor (which mixes gasoline with air) incorporates air with biogas instead. The machine can run on 100% biogas throughout its operation [14].
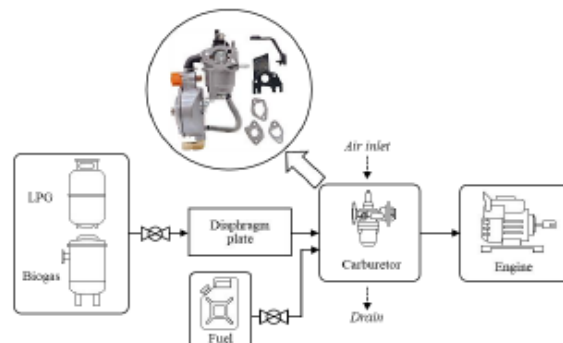

Figure 3 Biogas and LPG supply system for IC engine.

This work chooses a Honda GX200T2 QHT [15], a small four-stroke IC gasoline engine with a horizontal shaft. Air-cooled, it delivers a maximum power of 4.1 kW at 3,600 rpm and a maximum torque of 12.4 Nm at 2,500 rpm according to SAE J1349 standards. The dual fuel carburetor also allows the engine to accept biogas [15] LPG/ biogas when the engine is started. Negative pressure is supplied to the pressure regulating valve through the mixer. The seal arm swings to open the valve, and combustible gas enters the engine after decompression. The pressure regulating valve closes at the same time, and the combustible gas will stop when the engine shuts down.

4.2 Self-excited induction generator selection with DC-to-DC power conversion

A squirrel cage induction motor is suitable for direct coupling with the IC engine [16-18], where the operation speed is around 3000 RPM. This study selected a HITACHI TFO-K series [19], 220 V/ 380 V 2.2 kW two-pole three-phase induction motor as an SEIG. The designed system connects to an output voltage of 220 V and a frequency of 50 Hz, a low-voltage grid system. The inverter requires a minimum DC voltage of 311 V, so the output voltage and frequency of the generator must be properly regulated.

The generator requires reactive power to excite the strength of the magnetic field at the rotor core to generate a voltage at the terminals. The capacitor bank generates reactive power during the build-up, and when the load is connected, it continually uses the VSC-based PWM rectifier controlled by the PWM stage to impersonate this function [16, 18].
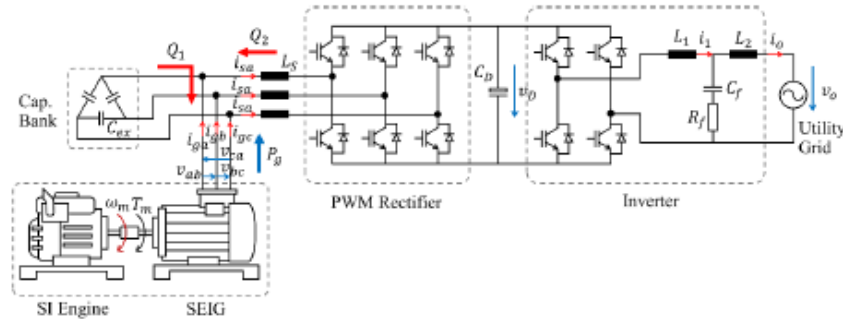
Figure 4 Proposed back-to-back converter with a capacitor bank

Figure 4 shows the topology of the proposed back-to-back converter. The SEIG with delta-connected windings generates a line-to-line AC voltage of 220 V, taking Q_1 from the capacitor bank. The VSC-based PWM rectifier boost-type converts the line-to-line voltage to v_D 400 VDC bus voltage. Then the v_D is converted to the required output voltage with an LCL active filter circuit to make it a pure sine before being fed to the grid [20, 21].

4.3 Power converter control structure

Figure 5 depicts the power converter control system. The SEIG-side and grid-side control schemes are implemented on a TMS320F28069 32-bit microcontroller from Texas Instruments [22]. The voltage and current signals of the SEIG and grid are sampled via the embedded analog-to-digital converters (ADCs), from which the control schemes generate the switching signals from the PWM units for the IGBTs via the gate driver circuits. The SEIG and capacitor bank are three-phase AC voltage sources with a star connection. The shaft rotational speed is not required. The shaft speed can be estimated from the generator frequency ω_g for a supervisory control system, along with other mechanical parameters such as temperatures, biogas pressure, and flow rate [20, 21].
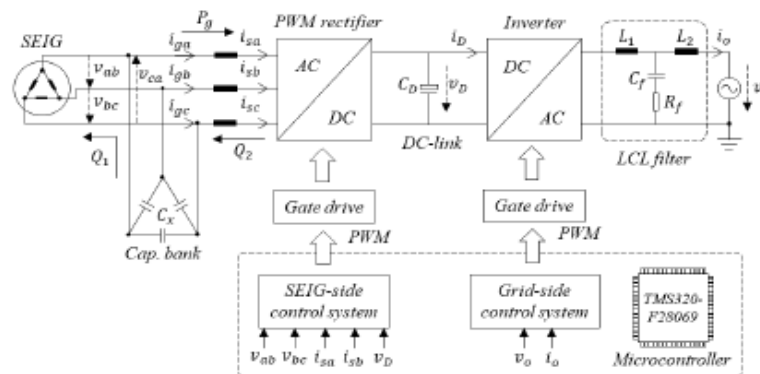

Figure 5 Power conversion topologies for the biogas power generation system design

The SEIG control scheme is implemented in the synchronous reference frame [20-23], so the active and reactive powers can be controlled separately. The control system of the PWM rectifier in the synchronous reference frame. A phase-locked loop (PLL) is used in this study [20, 21], which is implemented in the synchronous reference frame to estimate the angle and the frequency from the measured line-to-line voltages.

The output stage of the proposed topology in Figure 5 is the single-phase LCL-filtered grid-connected inverter. The damping resistor R_f of the LCL filter ensures control stability with the presence of a large grid impedance grid current (t) feedback control used in this study. The grid-side control system of the single-phase inverter is implemented in the multiple unbalanced synchronous reference frame on the same microcontroller with the SEIG-side control. The proposed control scheme consists of the fundamental component controller at the grid frequency and multiple harmonic controllers at frequencies. The harmonic controllers are used for the rejection of low-frequency voltage harmonics in the grid voltage and inverter output voltage due to switching dead times.

The proposed power converter in Figure 5 was constructed with the parameters listed in Table 4. The excitation capacitors C_x build up the SEIG voltage to the nominal value of $V_{LL} = 220$ V (line to line) at the no-load rotational speed approximately of 3,000 rpm. Assuming that the efficiency of the converter and SEIG is 70%, the nominal output power was set at 1.5 kW at which the mechanical input power $P_m = 2.14$ kW is close to the rated power.

Table 4 Parameters of the inverter

Symbol	Quantity	Value
P_o	Nominal output power	1.5 kW
V_{LLB}	Nominal SEIG line-to-line voltage	220 V
f_{gB}	Nominal SEIG frequency	50 Hz
C_{ex}	Excitation capacitors	40 µF (Δ connection)
V_D	Nominal DC voltage	400 V
V_o	Nominal grid voltage	220 V
f_o	Grid frequency	50 Hz
f_c	Triangular carrier frequency	10 kHz
f_s	Sampling frequency	20 kHz
L_s	SEIG-side inductor	2 mH
C_D	DC bus capacitor	1000 µF
L_1	LCL filter inductor	1 mH
L_2	Grid-side inductor	0.5 mH
C_f	LCL filter capacitor	3 µF
R_f	LCL filter damping resistor	1 Ω

4.4 Designing the power monitoring system with IoT devices

The design of an electrical power display system based on a smartphone application is schematically shown in Figure 6(a). This research uses the *EasyLogic* PM2230 [24] power meter manufactured by Schneider Electric, which is used for industrial applications. Modbus protocol connection is supported by specifying the register location of the required parameters from the manufacturer's instruction manual. The data from the power meter is sent to the *NodeMCU* ESP32 via RS485 Modbus Protocol and converted to TTL (Transistor-Transistor Logic). It is forwarded via Wi-Fi to Google Firebase [25] as a real-time database for displaying windows on applications, by an application designed with MIT app inventor software developed on the MIT platform using Component Oriented Software (Component-based Software Development) principles without writing commands (Source code) [26, 27]. The real-time data collection system that is designed can be seen in Figure 6(b). We chose to collect the data on Google Sheets in real time every ten minutes. We created JavaScript code to retrieve the values sent from the *NodeMCU* ESP32 and store them in Google Sheets with the Google Apps Script function.
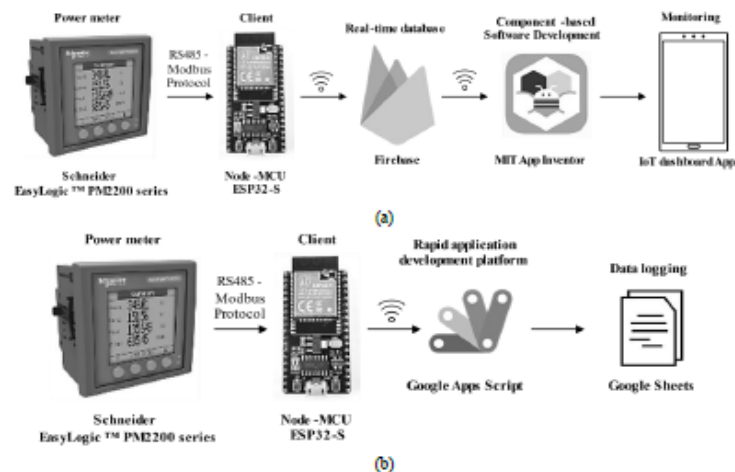

(a)

(b)

Figure 6 Power Monitoring System based on the IoT: a) Power monitoring system on an application, and b) Realtime data logging.

5. Experimental setup

5.1 Experimental procedures

The experimental design was divided into two parts with different implications, namely, 1) laboratory testing, for testing the efficiencies of the SEIG, the inverter, and the control system. The system was operated on gasohol 95 fuel, with the test system connected to the grid at a power rating of 1.5 kW. 2) Field Test: to test and compare the engine performance using three types of fuel: gasohol 95, LPG, and Biogas, shown in Figure 7.

Figure 7 Experimental Setup of biogas generation unit

The performance of the prototype biogas power generation system was validated with biogas in the selected area, Ta Manoa Subdistrict, in December 2021. The composition of the biogas was monitored by an IRCD4 gas analyzer from Beijing Shi'An Technology Instrument during the experiment, as listed in Table 2. The engine's exhaust gas was also monitored using an SA500 gas analyzer from Beijing Shi'An Technology Instrument.

Figure 8 depicts the performance evaluation diagram of the prototype system. The tests used gasohol containing 90% of 95-octane gasoline and 10% ethanol by volume. The average thermal input power was determined from the consumption rate using a digital weighing scale monitored in ten-minute periods. LPG and biogas fueled the engine. Then the thermal input power was determined from the volumetric flow rate using a thermal mass flowmeter and the CH_4 content monitored by a gas analyzer. A torque-speed sensor was mounted on the shaft between the engine and the SEIG to measure the torque, speed, and mechanical power. A four-channel power analyzer measured the electrical parameters at the SEIG and converter outputs. A four-channel digital oscilloscope recorded the waveforms of the current and voltage.
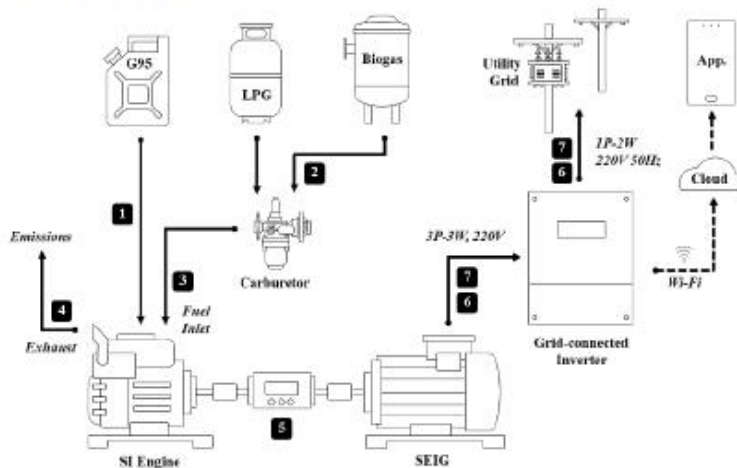

Figure 8 Schematic of experimental setup and measurement diagram of the proposed model: 1) Digital weighing scale, 2) Gas analyzer, 3) Flow meter, 4) Gas exhaust detection, 5) Torque/ speed sensor, 6) Digital power meter, 7) Four-channel digital oscilloscope

5.2 Calculation of overall system efficiency

The efficiency for the engines, generators, inverters, and systems can be calculated as follows [28, 29];

1) Engine performance (Efficiency of engine, η_{eng})

$$\eta_{eng} = \frac{Mechanical\,power\,output}{Rate\,of\,fuel\,energy\,input} \tag{1}$$

2) Generator performance (Efficiency of generator, η_{gen})

$$\eta_{gen} = \frac{Electrical\,power\,output}{Mechanical\,power\,input} \tag{2}$$

3) Inverter performance (Efficiency of inverter, η_{inv})

$$\eta_{inv} = \frac{Electrical\,power\,output}{Electrical\,power\,input} \tag{3}$$

4) System performance (Efficiency of system, η_{sys})

$$\eta_{sys} = \frac{Net\,Electrical\,power\,output}{Rate\,of\,fuel\,energy\,input} \tag{4}$$

6. Results and discussion

6.1 Engine performance

The test conditions with biogas were identical to the laboratory tests with gasohol. The no-load speed during the field experiments was set at approximately 3,250 rpm. The shaft speed with biogas drops at an output power greater than that with gasohol in the laboratory test. Thus, the excitation capacitors $C_{ex} = 40\ \mu F$ were used in the field experiment in response to the higher no-load speed. For the field tests with biogas, the prototype system delivered a maximum output power of 1,200 W, 80% of the rated value due to low biogas production. The composition of the biogas in the field test is shown in Table 5.

Table 5 Biogas composition in the field experiments

Composition	Content
CH_4	68.5%-70.0%
CO_2	30%
H_2S	0.14%-0.24%

Figure 9 compares the efficiency of the engine with biogas, LPG, and gasohol 95 (G95). The engine efficiency with biogas is approximately 14.43% at an output power of 80%. The engine efficiency with biogas is expected to be about 15% at the rated power, estimated from the engine efficiency with gasohol and LPG curves.
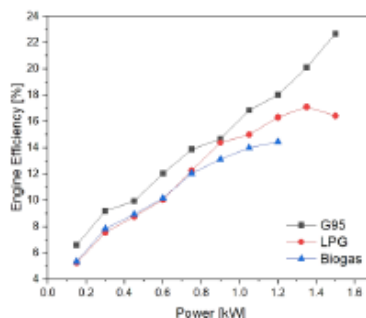

Figure 9 The engine efficiency with biogas gasohol and LPG curves

6.2 Generator performance

Figure 10 compares the generator of the engine with biogas, LPG, and gasohol 95 (G95). The generator efficiency with biogas is approximately 72.27% at an output power of 80%. The generator efficiency with biogas is expected to be about 73% at the rated power, estimated from the generator efficiency with gasohol and LPG curves.
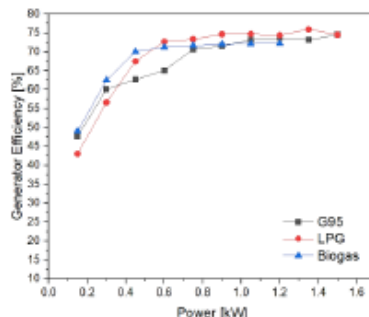
Figure 10 The generator efficiency with biogas gasohol and LPG curves

6.3 Inverter performance

Figure 11 compares the inverter of the engine with biogas, LPG, and gasohol 95 (G95). The inverter efficiency with biogas is approximately 95.33% at an output power of 80%. The inverter efficiency with biogas is expected to be about 96% at the rated power, estimated from the inverter efficiency with gasohol and LPG curves.
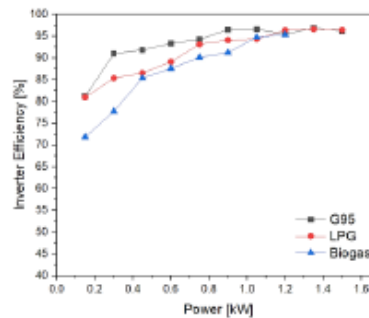

Figure 11 The inverter efficiency with biogas, gasohol, and LPG curves

6.4 System performance

Figure 12 compares the system of the engine with biogas, LPG, and gasohol 95 (G95). The system efficiency with biogas is approximately 10.65% at an output power of 80%. The system efficiency with biogas is expected to be about 13% at the rated power, estimated from the system efficiency with gasohol and LPG curves.
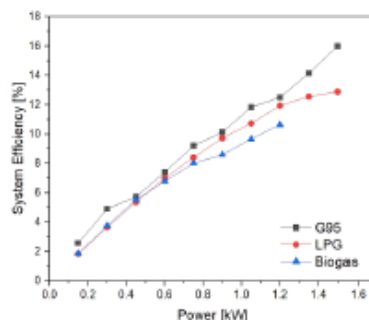

Figure 12 The system efficiency with biogas gasohol and LPG curves

557

6.5 CO and NOx emissions

Figure 13 shows NOₓ and CO emissions of the exhaust gas. The NOₓ emission with biogas is far less than that with gasohol. The NOₓ emission of the biogas-fed system is less than 50 ppm at 80% output power thanks to the purification process using the Fe(OH)₃ absorbent granules. Meanwhile, the CO emission of the biogas-fed engine decreases with the output power, where the CO emission is smaller than 400 ppm at 80% output power. This is believed to be due to there being a complete combustion process. On the other hand, the CO emission with gasohol is 2,000 ppm for every output power level. This indicates that the indicated values were limited by the measurable range of the exhaust gas analyzer, and the actual CO emission was above 2,000 ppm.
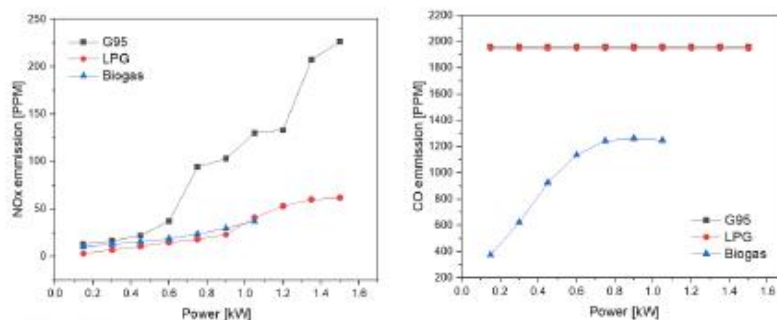

Figure 13 NOₓ and CO emissions of the exhaust gas

6.6 Electrical power

The SEIG-side control system, Figure 14 displays the steady-state waveforms of the grid voltage $v_o(t)$ and current $i_o(t)$ and the SEIG voltage $v_{gab}(t)$ and $i_{go}(t)$ at the rated output power of 1.5 kW. The grid current's waveform is nearly sinusoidal due to the added harmonic controller. The SEIG current's waveform is also nearly sinusoidal, which does not impose an additional loss due to current harmonics. The grid current harmonics comply with the IEEE 1547 Standard [20].
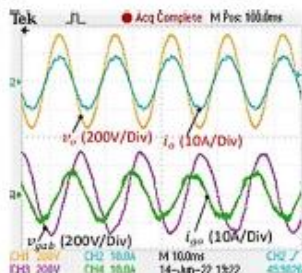

Figure 14 Steady state waveforms of the grid voltage and current and SEIG voltage and current.
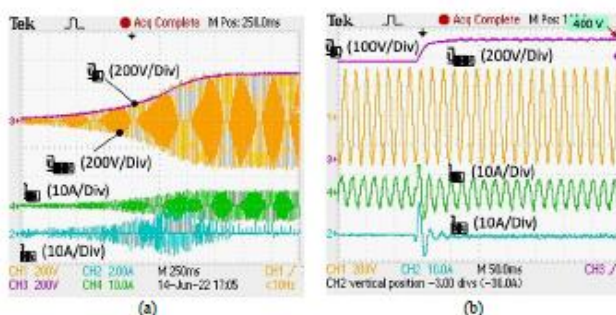

Figure 15 Transient voltage and current waveforms of the SEIG-side converter: (a) Voltage build-up period, (b) DC bus voltage startup period.

Figure 15(a) shows the SEIG voltage build-up period. In the beginning, there is a small SEIG voltage $v_{gab}(t)$ induced by the residual flux density in the rotor core, which is gradually increased due to the reactive power $q_1(t)$ from the capacitors C_{ex}. While building the terminal voltage, the SEIG also supplies active power to the DC bus capacitor C_b with the VSC operating as a passive rectifier. Figure 15(b) shows the startup of the PWM rectifier when $v_D(t)$ is increased to the reference $V_{Dref} = 400$ V. The voltage $v_{gab}(t)$ drops during the transient condition because the SEIG supplies the active power $p_g(t)$ to the bus capacitance. However, the SEIG is kept excited due to the reactive power $q_2(t)$ feeding back from the PWM rectifier to the SEIG.

6.7 Power monitoring system

This test used two power meters, a three-phase, three-wire delta ungrounded on the generator side and the second a one-phase, two-wire delta on the grid side as shown in Figure 16. The efficiency as determined from the data recorded in this experimental setup can be compared with that derived from the data recorded with the standard measuring equipment. Here, a power meter, model Chroma digital power meter 66204, is installed on the grid side to measure and record data every five minutes for comparison by setting the parameters Vs, Is, and Fs. The comparison uses the square root of the mean squared error (RMSE) to evaluate of the error from the proposed data collection system. The comparison is shown in Figure 17.
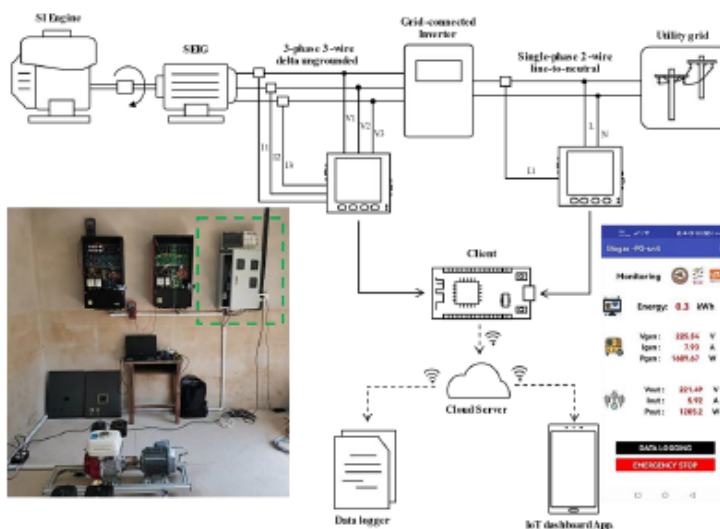

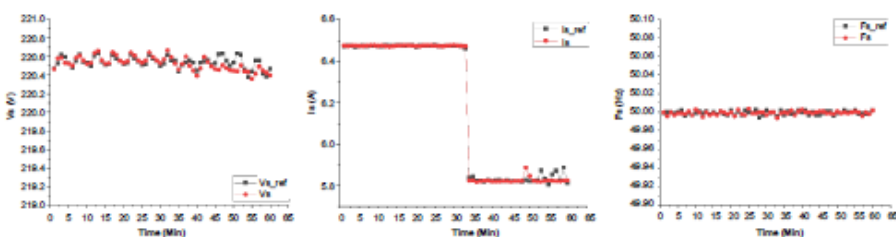**Figure 16** Power Monitoring System based on IoT

Figure 17 The errors from the proposed data acquisition system using RMSE

Figure 17, shows that the parameter data measured by the measuring instrument compared to the display system and the data collected in real-time were similar. When estimating the error values from the proposed data acquisition system using RMSE, it was found that the recorded grid voltage V_s, grid current I_s and grid frequency F_s tested had tolerances of 0.05888, 0.12547, and 0.00244 respectively, which are in the acceptable range and very close to those obtained by the standard measuring tools.

6.8 Analyzing biogas-fueled consumption in the proposed micro-power generation

In the previous test, we used one of the pig farm waste biogas sources mentioned in the section above. It was found to have a maximum power capacity of 1.2 kW. We analyzed the amount of pig manure required per hour for this farm. Based on the data from

Table 2, the results are as follows: The system requires 0.217 m3 of biogas per hour, equivalent to a minimum of 8.47 kg of raw materials per hour. Assume we want to produce electricity 8 hours per day at 1.2 kW. That means this pig farm needs to have at least 34 pigs.

In addition, we also analyzed and classified the required quantities of raw material for power generation at 1.2 kW per hour for other types of waste, from the agricultural and livestock sectors, as shown in Tables 6 and 7.

Table 6 Raw material for power generation at 1.2 kW per hour (Agricultural sector).

Type	Waste	Biogas Production rate (m^3/kg(dry))	Required material (kg)	Dry material (kg)	Raw material (kg)	Product mass (kg)
1. Rice	Straw	0.162	6.83	6.83	6.83	58.99
2. Corn	Trunk	0.250	4.423	6.32	9.03	28.14
	Leaves	0.225	4.92	5.46	6.07	19.59
	Stubble	0.344	3.21.	3.57	3.97	25.35
3. Sugarcane	Leaves and Shoots	0.262	4.22.	6.03	8.617	23.38
	Stems and Leaves	0.274	4.04	6.21	9.557	222.06
4. Cassava	Rhizome	0.141	7.84	12.07	18.567	120.15

Table 7 Raw material for power generation at 1.2 kW per hour (Livestock sector).

Type	Biogas Production rate (m^3/kg(solids))	Required material (kg)	Solid material (kg)	Raw material (kg)
1. Beef cattle	0.307	3.60	4.16	8.32
2. Dairy Cattle	0.307	3.60	4.16	5.20
3. Breeder Pigs	0.217	5.09	6.78	8.48
4. Piglets	0.217	5.09	6.78	8.48
5. Fattening Pigs	0.217	5.09	6.78	8.48
6. Chickens	0.242	4.57	5.96	7.45

6.9 Economic

The engine is programmed to run for eight hours each day, thus overall, there will be 14,600 hours of operation. A spark-ignition engine powered by biogas can run for up to 60,000 hours [30]. With a 7% interest rate, the five-year life-cycle cost (LCC) is USD 1046. Assume that poor biogas output and system maintenance result in a 10% system downtime. The following is then provided, with a 1.2 kW annual energy yield, and with a retail electricity price of USD 0.12, the estimated annual revenue is USD 378.36. The payback period will therefore be 2.8 years compared with purchasing electricity.

7. Conclusions

This work presented a small grid-connected power generation unit for farming systems to support the Bio-Circular-Green Economic (BCG) model in Thailand. The main conclusions are the following:
- A maximum power transmission system of 1.2 kW with a thermal efficiency of 10.7% if the system operates at 1.2 kW.
- Assume that we aim to generate 1.2 kW of electricity for 8 hours each day. Accordingly, this pig farm must have at least 34 pigs.
- The payback period will therefore be 2.8 years.
- The CO emissions of biogas-fed engines decrease with the power output, where CO emissions of less than 1300 ppm at 80% power output are believed to be due to complete combustion. On the other hand, CO emissions with gasohol 95, and LPG are 2000 ppm for all power levels.
- The advantages of the proposed biogas power generation system can be summarized as follows:
  1) The system supports a circular economy for agriculture and livestock sector, moving to sustainability.
  2) The proposed power generation system is a dispatchable renewable source, which can be used for grid support, and which will be part of the smart grid in the near future.
  3) The system is easy to operate, and maintenance of the engines can be done in the community.

8. Acknowledgements

9. References

[1] Palapleevalya P, Poboon C, Mungcharoen T. Development of sustainable consumption and production indicators for industrial sector according to circular economy principles in Thailand. Interdiscip Res Rev. 2021;16(6):13-8.

[2] Edyvean RG, Apiwatanapiwat W, Vaithanomsat P, Boondaeng A, Janchai P, Sophonthammaphat S. The bio-circular green economy model in thailand – a comparative review. Agr Nat Resour. 2023;57(1):51-64.

[3] Energy Policy and Planning office. Thailand power development plan 2018 Rev. 3 [Internet]. 2018 [cited 2019 Nov 15]. Available from: https://www.eppo.go.th/images/Infromation_service/NEWS/2018/PDP_Public_Hearing2018_3.pdf.

[4] Liu Y, Ma X, Shu L, Hancke GP, Abu-Mahfouz AM. From industry 4.0 to agriculture 4.0: current status, enabling technologies. IEEE Trans Industr Inform. 2021;17(6):4322-34.
[5] Scot MK, Furstenau LB, Kipper LM, Giraldo FD, López-Robles JR, Cobo MJ, et al. Precision techniques and agriculture 4.0 technologies to promote sustainability in the coffee sector: state of the art, challenges and future trends. IEEE Access. 2020;8:149854-67.
[6] Cheng WM, Liu HJ, Chen R, Chang WC, Yuan JJ, Chen J, et al. A real and novel smart agriculture implementation with IoT technology. The 9th International Conference on Orange Technology (ICOT); 2021 Dec 16-17; Tainan, Taiwan. USA: IEEE; 2021. p. 1-4.
[7] Aceleanu MI, Şerban AC, Suciu MC, Bițoiu TI. The management of municipal waste through circular economy in the context of smart cities development. IEEE Access. 2019;7:133602-14.
[8] Khotmanee S, Pinsopon U. A study on biogas production potential in Thailand 2019. The 7th International Conference on Engineering–Applied Sciences and Technology (ICEAST); 2021 Apr 1-3; Pattaya, Thailand. USA: IEEE; 2021. p. 269-72.
[9] Chanathaworn J, Dussadee N. Application of supporting media for improvement of anaerobic digestion performance and biogas production. Int J Renew Energy. 2017;12(2):65-74.
[10] Schlegel M, Kanswohl N, Rossel D, Sakalauskas A. Essential technical parameters for effective biogas production. Agron Res. 2008;6(SI):341-8.
[11] Fathabadi H. Internal combustion engine vehicles: converting the waste heat of the engine into electric energy to be stored in the battery. IEEE Trans Veh Technol. 2018;67(10):9241-8.
[12] Barz M. Biomass technology for electricity generation in community. Int J Renew Energy. 2008;3(1):1-10.
[13] Paenpong C, Pratoomchai N. Performance evaluation of a small spark-ignited engine with an electromagnetic intake valve. J Res Appl Mech Eng. 2021;9(1):1-14.
[14] Rao R, Raju R, Rao M. Experimental investigations on the Mahua fuelled C.I engine with different oxygenates. Int J Renew Energy. 2008;3(1):63-70.
[15] Honda. General purpose engines GX series ed Honda Power Products [Internet]. 2019 [cited 2019 Nov 15]. Available from: https://engines.honda.com/models/series/gx.
[16] Blaabjerg F, Lungeanu F, Skaug K, Tonnes M. Two-phase induction motor drives. IEEE Ind Appl Mag. 2004;10(4):24-32.
[17] Mosaad MI. Optimization of self excited induction generator using constrained particle swarm optimization. Thammasat Int J Sc Tech. 2011;16(3):37-45.
[18] Ojo O, Jimoh AA. Steady-state and dynamic analyses of isolated self-excited induction generators. Trans South Afr Inst Electr Eng. 1999;90(1):14-9.
[19] Hitachi. Hitachi electric motors for industial application [Internet]. 2010 [cited 2019 Nov 15]. Available from: https://hiem.hitachi.com.my/brochures/pdf/Brochure_ElectricMotor.pdf.
[20] Somkun S. High performance current control of single-phase grid-connected converter with harmonic mitigation, power extraction and frequency adaptation capabilities. IET Power Electron. 2021;14(2):352-72.
[21] Somkun S. Unbalanced synchronous reference frame control of singe-phase stand-alone inverter. Int J Electr Power Energy Syst. 2019;107:332-43.
[22] Somkun S, Chunkag V. Unified unbalanced synchronous reference frame current control for single-phase grid-connected voltage-source converters. IEEE Trans Ind Electron. 2016;63(9):5425-36.
[23] Texas Instruments. TMS320x2806x Microcontrollers Technical Reference Manual [Internet]. 2011 [cited 2019 Nov 15]. Available from: https://www.ti.com/product.
[24] Schneider Electric. EasyLogic PM2200 Series User Manual [Internet]. 2020 [cited 2020 Dec 5]. Available from: https://www.se.com/th/th/download/document/NHA2778902-01.
[25] Spath P. Firebase. In: Spath P, editor. Pro Android with Kotlin. Berkeley: Apress; 2022. p. 363-6.
[26] Mir SB, Llueca GF. Introduction to programming using mobile phones and MIT App inventor. IEEE Revista Iberoamericana de Tecnologías del Aprendizaje. 2020;15(3):192-201.
[27] Mikolajczyk T, Fuwen H, Moldovan L, Bustillo A, Matuszewski M, Nowicki K. Selection of machining parameters with Android application made using MIT App Inventor bookmarks. Procedia Manuf. 2018;22:172-9.
[28] Sutheersak E, Pirompugd W, Sanitjai S. Performance and emissions characteristics of a direct injection diesel engine from compressing producer gas in a dual fuel mode. Eng Appl Sci Res. 2018;45(1):47-55.
[29] Poonnakhun W, Suntivarakorn P, Theragulpisut S, Sookkumnerd C. The effect of biodiesel on diesel engine performance. KKU Eng J. 2006;33(3):193-208. (In Thai)
[30] Kaparaju P, Rintala J. Chap 17 - Generation of heat and power from biogas for stationary applications: boilers, gas engines and turbines, combined heat and power (CHP) plants and fuel cells. In: Wellinger A, Murphy J, Baxter D, editors. The biogas handbook. Cambridge: Woodhead Publishing; 2013. p. 404-27.